Porosity Engineering of Boron Nitride Materials for Hydrogen Storage

Weng Qunhong

Doctoral Program in Materials Science and Engineering

Submitted to the Graduate School of

Pure and Applied Sciences

in Partial Fulfillment of the Requirements

for the Degree of Doctor of Philosophy in

Engineering

at the

University of Tsukuba

Abstract

Our society is running on fossil fuels for over two centuries. With the tremendous consumption of these carbon-rich fossil fuels, the fixed carbon underground is releasing to our atmosphere; the concentration of CO_2 in our atmosphere is continually rising. This produces long-term effects and threatens our environment, makes it unpredictable, and possibly disastrous. Thus, searching for "green" fuels that can substitute fossil fuels is on the urgent agenda. Among the candidates for future clean fuels and energy, H_2 attracts particular attentions due to its zero-pollutant emission during the consumption. However, realization of the practical applications of hydrogen still presumes a lot of challenges facing by the scientific community. Hydrogen should be first produced, effectively stored and then delivered to an end user. In this chain, the bottle-neck problem is how to store H_2 efficiently and safely. Traditional storage methods relied on compressed gas cylinders, which themselves require an energy-consuming treatment and have notable safety risks. To date, most of H_2 storage is based on physisorption, chemisorption and chemical reactions. Physisorption is featured by the fast adsorbing/releasing kinetics, superb reversibility, and cycling features. Many researchers focused on the novel designs and found new H_2 adsorbents relying on the physisorption mechanism and employing its advantages. And my project related to a design of advanced porous boron nitride (BN) nanomaterials for H_2 storage, from this viewpoint, is meaningful and important.

Compared to traditional porous carbons and metal-organic frameworks (MOFs), porous BNs exhibit excellent thermal stability and resistance against chemicals, which can improve their cycling and regeneration abilities during H_2 storage. However, the state of development of reliable methods to prepare porous BN materials is not that optimistic at present; there were no reports on porous BNs with a specific surface area (SSA) >1000 $m^2 g^{-1}$ before 2012 (the starting time of my PhD project). This situation also makes BNs far less known within the scientific community with respect to their H_2 storage potentials. In my dissertation, I focus on the development of easily operable, one-step, and template-free reactions to fabricate porous BN nanomaterials, and using these porous BNs for H_2 detailed storage studies. The fundamental material textural factors responsible for their H_2 sorption behaivors are also carefully explored and discussed.

I will firstly introduce hierarchically porous BN microbelts with the SSA ranging from 1144 to 1488 $m^2 g^{-1}$, which were the first BN materials in the world with the SSA exceeding 1000 $m^2 g^{-1}$. They were synthesized by a one-step reaction of boric acid-melamine (2B·M) adducts in ammonia at temperatures varied from 900 to 1100 ^oC. Comprehensive characterizations including high-resolution transmission electron microscopy, X-ray diffraction, and Raman confirmed the obtained BN phase is partially disordered, reveals an enlarged average (0002) spacing of 0.38 nm, larger than the standard 0.33 nm for bulk *h*-BN. Through varying the synthetic conditions, the textures of the prepared porous BNs were found to be

adjustable. It was shown that these high-surface-area BN porous belts possess high and reversible hydrogen uptakes ranging from 1.6 to 2.3 wt %.

Next, the synthesis of a series of microporous BN microsponges *via* this simple one-step template-free reaction will be introduced. The products showed increased inter-layer (0002) distances compared to the standard *h*-BN and revealed specific dislocation structures. The SSAs and pore volumes of these BN microsponges might be effectively tuned in a wide range (920−1900 m^2 g^{-1} and 0.516−1.070 cm^3 g^{-1}, respectively) via changing the synthetic conditions. Amazingly, there were almost no macro- and mesopores in these obtained BN microsponge products. Decent and totally reversible H_2 uptakes, from 1.65 to 2.57 wt % at 1 MPa and 77 K, were documented for these BN materials. Finally, I carried out the systematical studies of the correlations between the textural parameters of these novel materials and their H_2 sorption capacities.

Besides, I also made a modification of the synthetic conditions for BN microbelts to prepare composition-changed microbelts, namely porous BCNO microbelts. Three BCNO microbelt sample series were featured by similar morphologies, chemical compositions and partially disordered phases. Furthermore, they also showed high and close SSAs, pore volumes, but characteristic ultra-narrow pore widths that varied from 0.4 to 1.1 nm. Enhanced H_2 uptakes of 1.90–2.14 wt % at 1 MPa and 1.41–1.60 wt % at a lower pressure of 0.1 MPa were recorded for those materials. And importantly, I revealed the relationship between pore width and H_2 storage abilities for the fabricated BCNO porous materials.

Over all, I have developed a simple strategy for the fabrication of highly porous BNs, and prepared a series of new porous BN materials with different porosity (hierarchically porous and microporous) and chemical (BN and BCNO) features. They exhibited very high SSAs and pore volumes, and H_2 uptake capacities up to 2.6 wt % at 1 MPa and 77 K, which corresponded to a gravimetric energy capacity of ~0.87 kWh kg^{-1}. I hope my work will inspire many researchers in this field to design and search for better porous BN H_2 accumulators.

Acknowledgement

Great and exciting time always passes very quickly. Now, it is maybe the time to say goodbye to my PhD adventure. I remember Louis Pasteur who has a saying: "Chance favors only the prepared mind". And a PhD training will make a scientific researcher prepared to welcome his/her future chances and opportunities, as I believed. Here, firstly, I would like to express my most sincere gratitudes and respects to my supervisors, Profs. Dmitri Golberg and Yoshio Bando, for providing such a valuable chance to let me study in the National Institute for Materials Science (NIMS). In the past three years, I have benefitted a lot from their excellent academic guidance, helps and continuous supports. I deeply appreciate their all-round advices and suggestions on my work, and the time spent on this dissertation. I am very fascinated by their long-lasting enthusiasms and energetics peculiar to their work and daily life.

I also would like to acknowledge the University of Tsukuba and NIMS for their financial and living supports while I was staying in Tsukuba, especially for the fellowship provided by NIMS for its junior researchers (NIMS Graduate Research Assistantship). Certainly, WPI-MANA (World Premier International Center for Materials Nanoarchitectonics) has provided a large amount of machine time for various facilities, which is also indispensable to complete my project smoothly and in time.

During this period, I received many supports and helps from my co-workers and colleagues. The following co-workers involved in my project are particularly appreciated and acknowledged; they are namely, Prof. Chunyi Zhi, Dr. Xuebin Wang, Dr. Xi Wang, Dr. Xia Li, Prof. Yusuke Ide, Dr. Binju Wang, Dr. Dequan Liu, Mr. Chao Zhang, Dr. Xiangfen Jiang and Prof. Nobutaka Hanagata. I also wish to deeply thank my colleagues for their nice assistance and suggestions; they include but are not limited to Prof. Tianyou Zhai, Dr. Daiming Tang, Dr. Xianlong Wei, Dr. Fei Liu, Dr. Zhi Xu, Dr. Wei Tian, Dr. Maho Yamaguchi, Dr. Amir Pakdel, Dr. Jun Zhang, Dr. Naoyuki Kawamoto, Dr. Masanori Mitome, Dr. Akihiko Nukui, Dr. Yueming Xue, Dr. Pengcheng Dai, Dr. Shimou Chen, Ms. Xiaodan Wang, Dr. Kotone Hasegawa, Mr. Shigenobu Okamiya. Besides, many thanks should be given to my friends for many funny and happy moments they brought to my life in Tsukuba: Mr. Qinghui Shou, Dr. Pengfei Yan, Mr. Lei Dong, Dr. Chengxiang Wang, Dr. Jinghua Wu, Dr. Qi Wang, Dr. Fengxia Geng, Dr. Ming Hu, Dr. Cuiling Li, Ms. Yunqi Li, Mr. Bo Jiang, Mr. Yuexian Lin, Dr. Hongli Mao, Mr. Xingke Cai, Ms. Rong Cai, and many more from their circles and not included here. The secretary of our group, Ms. Yumiko Hirai, has provided many helps to solve the difficulties arisen from my experimental and personal affairs. Thanks a lot!

I never forget the other NIMS staff and members who kindly provided the trainings of facilities or analytical supports besides our group members. They are Drs. Makito Nakatsu (BET and XRD), Kiyotaka Iiyama (Raman, PL and IR), Isamu Yamada (TEM), Toshiaki Takei (TEM), Akihiro Tanaka (XPS),

Yoshiyuki Yajima (elemental analysis), and Satoshi Takenouchi (elemental analysis). Big thanks for their dedications.

Lastly, I need to thank all my family members and my old friends for their understanding and throughout supports while I was being abroad. I wish I can share my pleasures with them, wherever they are.

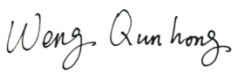

at Tsukuba

Table of Contents

Chapter 1

Introduction

Chapter 1. Introduction

1.1 Hexagonal boron nitride materials

1.1.1 Structure of hexagonal boron nitride

Boron nitrides are constructed by equal number of Boron (B) and Nitrogen (N) atoms, these structures are isoelectronic to the carbon lattices with similar morphologies. Among the existing numerous crystalline forms, the graphite-like hexagonal boron nitride (*h*-BN) is the most stable BN phase in the standard conditions. The cubic BN form (*c*-BN), corresponding to the diamond form, is well known for its superb hardness. While in wurtzite BN (*w*-BN) form, all B and N atoms are also sp^3-hybridized like in the case of c-BN, but its BN3 or NB3 tetrahedrons are stacked differently.

h-BN has a layered structure analogous to graphite (Figure 1.1). Within the layer, B and N atoms are bound by strong covalent bonds, whereas the layers are tighten together by weak van der Waals forces. However, the interlayer stacking mode of *h*-BN is different from graphite; B atoms in one *h*-BN layer lay over and above N atoms in the neighboring layers. This reflects the polarity nature of the B-N bonds. The electron pair is obviously confined closer to the N atom due to its larger electronegativity, and the lone pair electrons in the N p_z-orbital are only partially delocalized with B p_z orbital, compared to the equally contributed and electron-wise distributed C-C bonds in graphite layers.

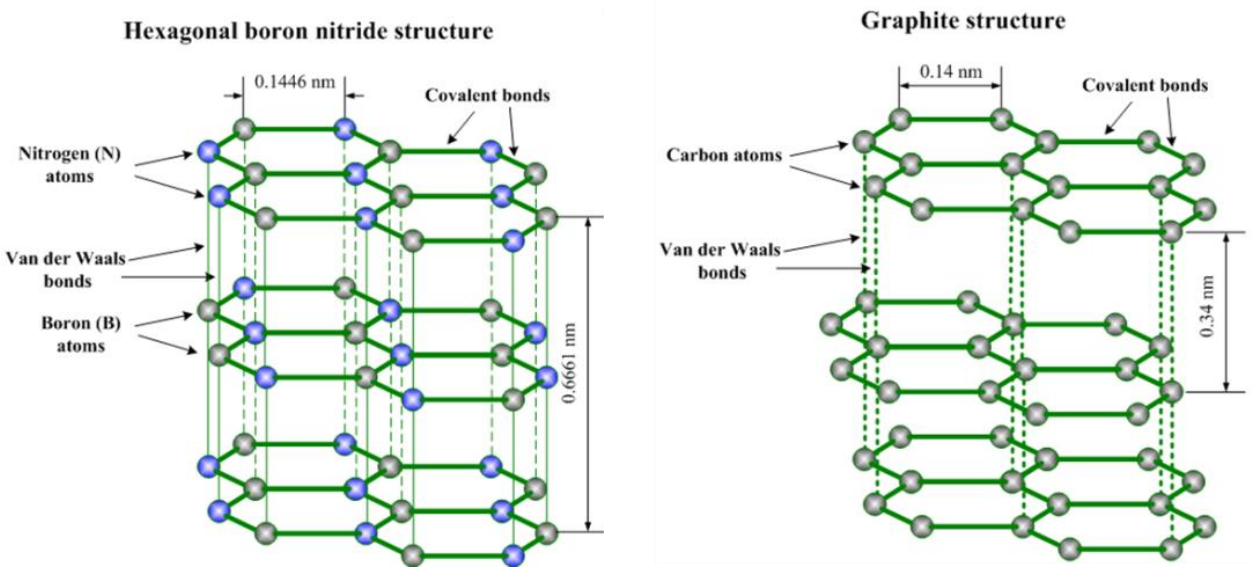

Figure 1.1 Structures of *h*-BN (left) and graphite (right). Reproduced from www.substech.com.

1.1.2 Physical and chemical properties of *h*-BN

The structural features of *h*-BN discussed above endow this material many important physical and chemical properties, such like high thermoconductivity, mechanical strength, electrical insulation, thermal and chemical stability, *etc*. Very different bonding features along and perpendicular to the basal planes cause high anisotropy of most of the *h*-BN properties. The partial ionic structure of BN layers in *h*-BN reduces electrical conductivity. The reduced electron-delocalization in *h*-BN leads to a large band gap and the colorless appearance. In industry, *h*-BN is widely used for high-temperature crucibles, anti-oxidation lubricants, protecting coatings, deep ultraviolet illuminants, cosmetics, thermal conductive fillers, microwave-transparent shields, *etc*. The basic physical and chemical properties of *h*-BN and graphite are summarized and compared in Table 1.1.

Table 1.1 Comparison of physical and chemical properties of *h*-BN and graphite. Data are reproduced from Refs. 1, 2.

Properties	***h*-BN**	**graphite**
Bond length (Å)	1.44	1.42
Bond energy (eV)	4.0	3.7
Interlayer distance, by diffraction (Å)	3.33	3.35
Bulk modulus (GPa)	36.5	34
In-plane thermal conductivity (W/mK)	600	200-2000 [3]
Charge transferred in covalence bond (e)	~ 0.4	~ 0
Band gap (eV)	5.5-6.0	~ 0
Breakdown voltage (MV/cm)	~ 7	conductor [4]
Dielectric constant (static, 25 ^{o}C)	5.06 ($\varepsilon_{\parallel}$) 6.85 ($\varepsilon_{\perp}$)	~ 0
Oxidation resistance (^{o}C)	900-950	~ 600
Appearance color	white	black

$\varepsilon_{\parallel}$ is parallel to *c* axis, $\varepsilon_{\perp}$ is vertical to *c* axis.

1.1.3 Development of nanostructured BN materials

Like other materials, BN materials were also a subject of many explorations in the last two decades in regards of their nanostructured forms and their corresponding properties. One may find that the development of BN nanomaterials goes well along with their carbon counterparts, from 0D fullerenes/nanocages [5,6] and 1D nanotubes in 1990s, [7] to 2D graphene/nanosheets in 2000s, [8] as well as with other morphologies like nanomeshes, [9] nanospheres, [10] nanowires, [11,12,13,14] nanoribbons, [15] and nanoporous BN. [16]

Fullerene-like BN nanocages were firstly observed under electron irradiation in 1998 (Figure 1.2). [5,6,17] Unlike C_{60} or other classical fullerene families, $(BN)_n$ nanocages (n = 12, 20, 24 or larger numbers) tend to form 4-, 6-, and 8-membered rings. [18] Due to such ring structures, the objects avoid the formation of unstable B-B and N-N bonds which are unavoidable in odd-numbered rings. Theoretically, BN nanocages are good lubricants, [19] and have a high adsorption capacity of H_2 (4 wt % at 298 K and 10 MPa) and organic pollutants. [20,21] However, they are rarely studied in the experiments due to difficulties in their macroscopic syntheses comparing with C_{60}.

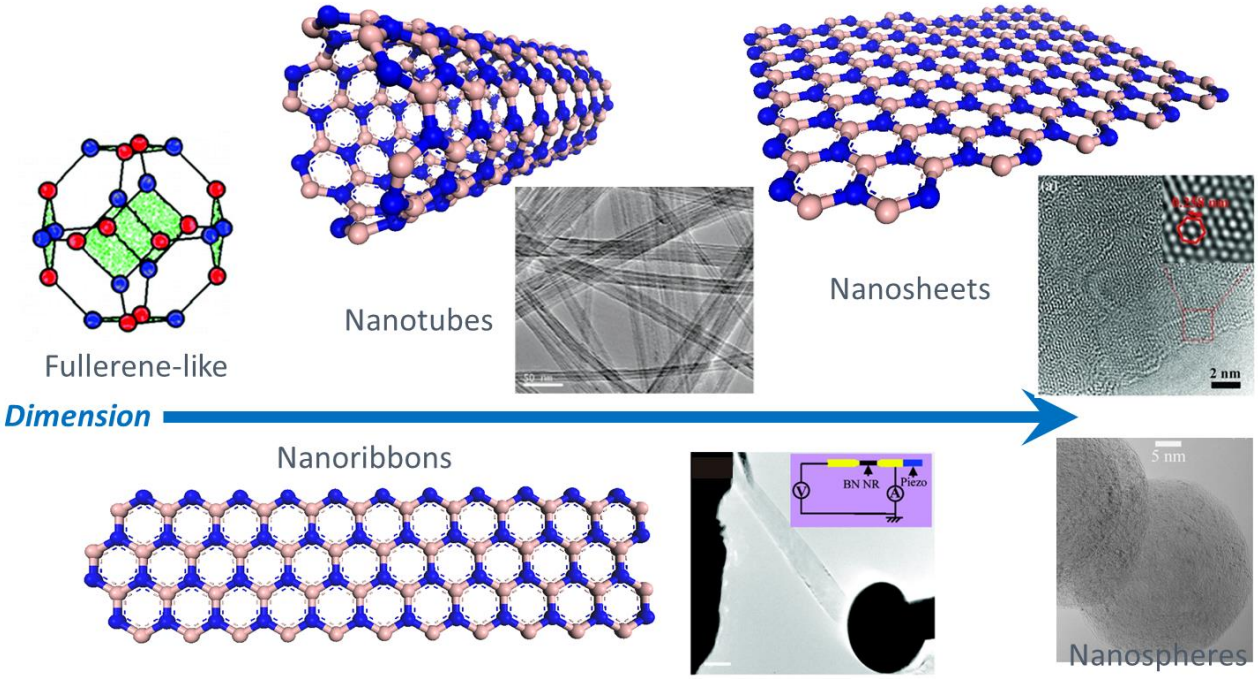

Figure 1.2 Nanostructured BN materials. The images are reprinted from Refs. 22,10,23,51.

Nanotubes are a typical 1D structure for nano-BN materials, which were firstly prepared in 1995. [7,24] After that, a variety of other 1D nanomaterials, such as nanoribbons and nanowires, were also investigated. BN nanotubes attract many attentions due to their unique properties. They may be utilized for mechanical reinforcements for many bulk materials, like polymers, [25] ceramics, [26] and metals. [27] Unlike carbon nanotubes and carbon fibers, using BNNTs as the fillers not only can improve the composite mechanical strength and

thermal conductivity, but also can maintain the high dielectric constant of a material.[28] This is very important for the packing materials in electronics. Besides, they were also applied for a hydrogen uptake (will be discussed in detail in the following section),[29] insulating coatings,[30] field emission,[31] ultraviolet luminescence,[32] and drug delivery.[33]

BN nanosheets, as the graphene analogue belonging to a representative advanced 2D material catalogue, have been "blooming" in the last ten years. Both top-down exfoliation and bottom-up growth strategies can be used to obtain BN nanosheets. The top-down method uses mechanical forces, such as sonication, shearing, ball milling, and surface tension, to overcome van der Walls interactions between/among *h*-BN layers and to exfoliate BN nanosheets.[34] The bottom-up growths, on the other hand, deposit different B- and N-containing precursors to grow the BN nanosheets with or without using substrates. CVD growth usually needs metal substrates, such like Cu, Ni, Pd, Ru, or Pt.[35,36,37,38] BN nanosheets with vertical alignment on Si and Si/SiO_2 surfaces were prepared by the microwave-plasma CVD[39] and catalyst-assistant CVD[40]. There are many unique applications of the BN nanosheets. Scientists found that graphene-based electronic devices would have an enhanced carrier mobility if using *h*-BN as the electronic substrate instead of standard SiO_2 substrates,[41] and, in addition, the zero-band gap of graphenes on *h*-BN nanosheets may be opened.[42,43] They can serve as the prominent spacers and protectors for tunneling transistors and devices,[44,45,46,47] and, also, as good anti-breakdown dielectric gate layers.[48] Besides, the sheet-like BNs are also useful as the nonwetting superhydrophobic,[49] and oxidation-resistant coatings.[50] Furthermore, they were applied in polymeric composites,[51,52,53,54] deep ultraviolet luminescence,[54,55,56] and solid-state lubrication.[57]

1.2 Porous materials

Based on IUPAC definitions, porosity or void fraction for a material is defined as a measure of the void (*i.e.* "empty") spaces in the material body, and is a fraction of the volume of voids over the total volume. Due to the variety of pore shapes and structures, pore width is defined as the diameter in case of a cylindrical pore and as the distance between opposite walls in case of a slit pore. Based on the pore width, the pores can be classified as macropore ($w>50$ nm), mesopore ($50\ nm > w > 2\ nm$) and micropore ($w < 2$ nm). Sometimes, a micropore will be further divided into a supermicropore ($0.7\ nm < w < 2\ nm$) and an ultramicropore ($w < 0.7$ nm). From this point, the porous material could also be viewed as a kind of special nanostructured material.

To date, there have been numerous techniques developed to evaluate the porosity of materials, such as scanning electron microscopy (SEM), atomic force microscopy (AFM), scanning tunneling microscopy (STM) and transmission electron microscopy (TEM), and gas, and liquid molecule adsorption-desorption methods. Among them, the method based on N_2 adsorption-desorption method is widely accepted as the standard method to evaluate material porosity, specific surface area, pore width and other textural properties. Different pore width and structure result in different N_2 physisorption isotherms and hysteresis loops of the

desorption branches. Currently, there are 6 types of adsorption isotherms and 4 types of hysteresis loops that have been observed.

1.3 Porous materials in hydrogen storage

Porous materials are very useful for our daily life and industrial applications. A thousand years ago, people had already known the magical functions of activated carbon in water purification, odor removal, *etc*. Modern chemical production processes can't be realized without porous materials. *E.g.*, most of the catalysts are dispersed on porous supports, like porous carbons and silica, zeolites, randanites, *etc*. Any filtering processes for heterogeneous mixtures need a porous separation medium. Removal of a low concentration of water, O_2, and other components to obtain the purified chemicals or other products can't be achieved without molecule sieves, which is a kind of porous material with well-tailored pore widths. These porous materials are also candidates as the accumulators for H_2, a green fuel for automobiles without any harmful emissions. Many porous materials, including carbon nanotubes, porous carbon materials, metal-organic frameworks (MOFs), BN nanotubes, were investigated in regards of H_2 storages. The cutting-edge porous material can achieve an H_2 uptake capacity of >10 wt % at 77 K. However, none of the materials have been confirmed to satisfy the threshold condition toward economical application of H_2; U.S. Department of Energy estimated that an economically feasible hydrogen storage material requires a 6.5 wt % uptake of H_2 at 2 MPa and room temperature. Thus, better H_2 storage materials are needed to finally solve this bottle-neck problem hampering the large-scale application of clean H_2 fuels.

1.3.1 MOF

MOFs are the promising hydrogen accumulation materials. They were extensively studied in the past decade. MOFs are crystalline materials which structurally consist of metal ions linked by organic ligands. Generally, MOFs have defined pore structures. Since MOF crystals are synthesized from metal ions and organic building blocks, the framework structure, pore width, and surface area, and other textural parameters can be well tuned by a proper selection of material building blocks. Multiple MOFs with relatively small to very large surface areas and pore widths have been reported.[58] In 2003, the initial H_2 storage data reported for MOF-5 prepared from benzene-1,4-dicarboxylate (BDC) and Zn(II) salt was 4.5 wt % at 77 K and 1 atm (101 kPa) [59] Since then, there have been many reports on porous MOFs for H_2 storages, many of them have different frameworks and pore structures, and they showed relatively high H_2 storage capacities. Many researchers have employed various metal ions like Zn(II), Cu(II), Cr(III), Mn(II), and lanthanides(III), and diverse types of ligands, such as carboxylates, imidazolates, triazolates, tetrazolates for the construction of the MOFs. To date, the highest excess H_2 storage capacity reported for MOFs (NU-100) is 9.95 wt % at 56 bar (1 bar = 100 kPa) and 77 K with a total capacity of 16.4 wt % 77 K and 70 bar.[60] MOF-210 is documented to have the highest total H_2 storage capacity of 17.6 wt % (excess 8.6 wt %) at 77 K and 80

bar.[61] These values are crucial to demonstrate the tremendous progress in research on MOFs as H_2 storage materials.

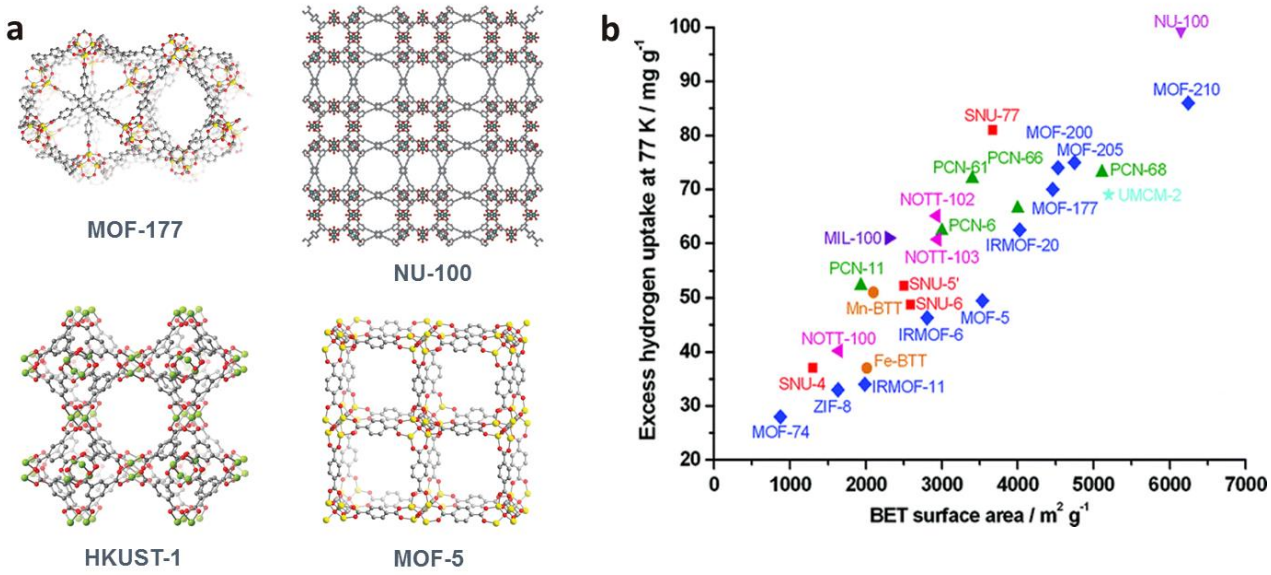

Figure 1.3 (a) Selected typical MOF structures (from Ref. 62) and (b) Excess high-pressure H_2 uptake capacity plot at 77 K versus BET surface areas for MOFs. Figure b is reprinted from Ref. 58.

1.3.2 Porous carbon materials

Besides the MOF materials, carbon-based materials, especially porous carbons, have also received a considerable attention with respect to H_2 physisorption studies. The advantageous properties of porous carbons include light nature of carbon, its abundance, thermal and chemical and stability, easy processing and low framework density. A lot of carbon structures with high SSA are well known, *e.g.* activated carbon, expanded/exfoliated graphite, fullerenes, carbon nanotubes (CNTs), nanofibers, *etc*. The state-of-the-art activation methods can obtain the porous carbons with SSAs up to 2700 m^2 g^{-1} by H_3PO_4 chemical activation,[63] 3400 m^2 g^{-1} *via* CO_2-activation of carbide-derived carbons,[64,65,66] and ~4000 m^2 g^{-1} by KOH activation.[67] The porous carbons with SSAs up to ~5000 m^2 g^{-1} have also been produced by the carbonization from MOFs.[68]

An activated carbon aerogel with the SSA of 3200 m^2 g^{-1} can store up to 5.3 wt % hydrogen at 77 K and 30 bar.[69] The porous carbons aimed for H_2 storage and obtained by direct activation of polymers and carbide-derived carbons exhibit very high SSAs (1850-3500 m^2 g^{-1}) and pore volumes (1.5-2.6 cm^3 g^{-1}); they show hydrogen storage capacity from 4.3 to 7.03 wt % at 77 K and 20 bar.[67] Wang *et al.* used a two-step procedure of physical activation (with CO_2) followed by chemical (KOH) activation to generate an activated carbon with the surface area of 3190 m^2 g^{-1}, which possesses a hydrogen uptake of up to 7.08 wt % at 77 K and 20 bar.[70] This figure is one of the best hydrogen uptakes evidenced for activated carbons.

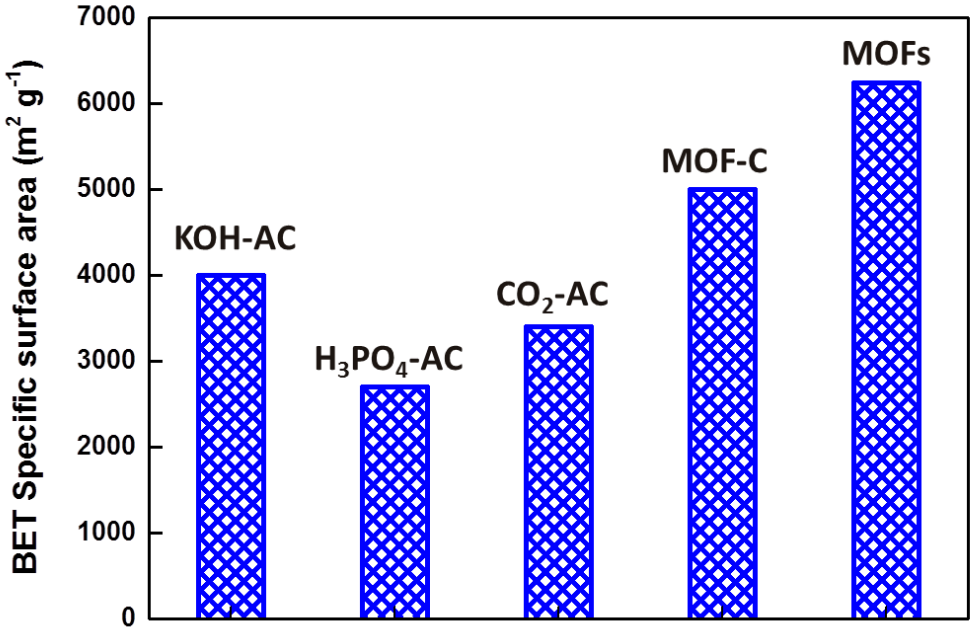

Figure 1.4 Summary of the highest values of BET surface area reported for different types of porous materials: KOH activated carbons (KOH-AC),[71] H_3PO_4 activated carbons (H_3PO_4-AC),[72] CO_2 activated carbons (CO_2-AC),[73 74] MOF-derived carbons (MOF-C) [68]and MOFs.[60]

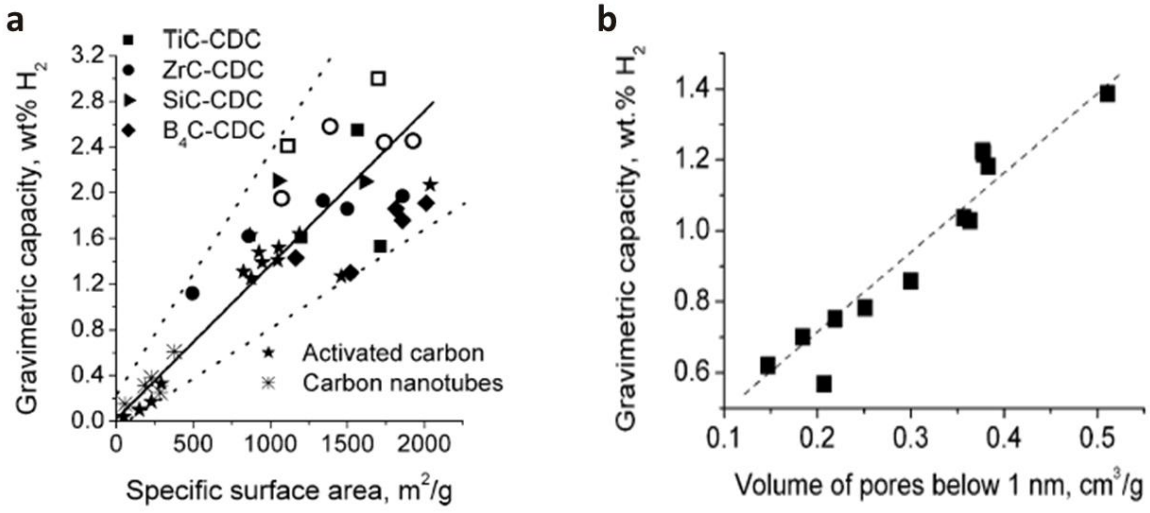

Figure 1.5 (a) Plot of H_2 uptake capacity value versus specific surface area of various carbon materials. (b) Plot of H_2 uptake value versus the volume of pores below 1 nm for the carbide-derived carbons. Reprint from Ref. 75.

Due to the availability of highly porous carbon materials with tailored SSAs, pore width, pore volumes, *etc.*, the correlations between these textual parameters with H_2 uptakes were also systematically investigated. Total SSA and pore volume of porous carbon materials can't establish a linear correlation with H_2 uptake

values. This is because only a portion of these SSA or volume that has enough affinity to adsorb H_2 molecules is effective for H_2 storage in carbon materials. Usually, narrower pore width will result in higher H_2 affinity (higher H_2 adsorption heat) given the same material surfaces. The corresponding results showed that pores with a width below 1 nm are effective for H_2 storage at ambient pressure and liquid-nitrogen temperature.[75]

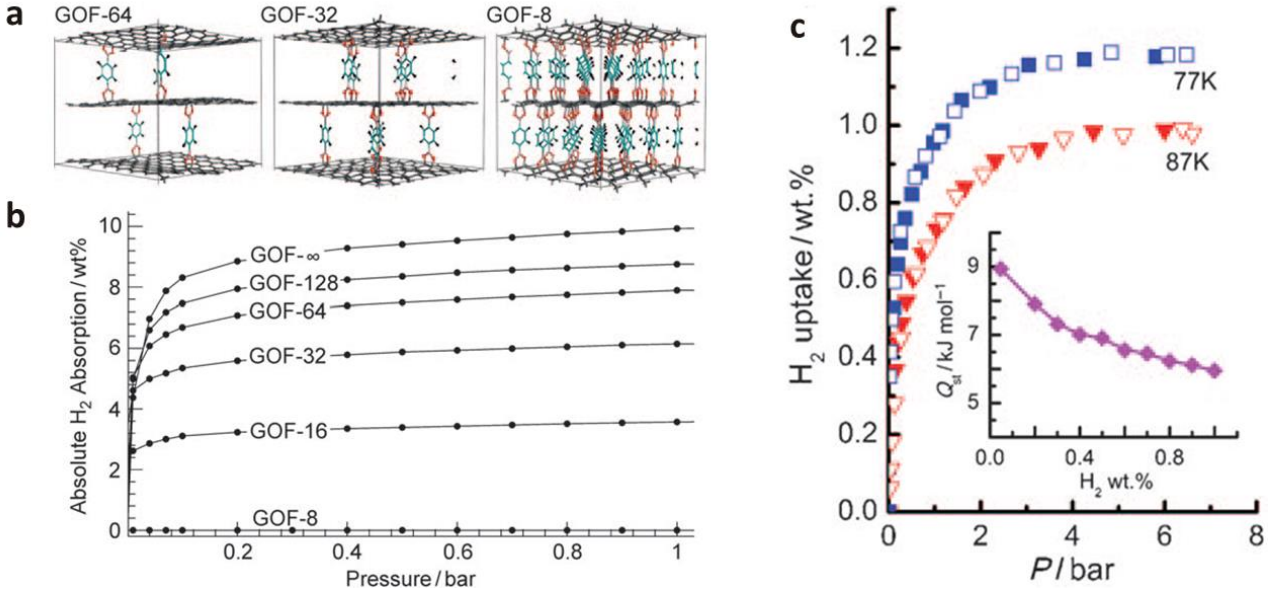

Figure 1.6 (a) Grand canonical Monte Carlo simulated GOF-n models with n graphene carbons per linker. (b) The simulated H_2 adsorption isotherms at 77 K for the GOFs. (c) H_2 adsorption isotherms of the COF prepared from 1:1 (GO:linker). (Reproduced from Ref. 76.)

Since many important properties were discovered in graphene, great enthusiasms were aroused regarding the graphene oxide studies, which were viewed as important issues for the primary architectonics. After rational designing and engineering the GO interlayer distance by chemical functionalization or physical spacing, it was possible to obtain the GO-based H_2 accumulators. Yildirim *et al.* designed a series of phenyldiboronic acid linked-GO model systems (GOFs) (Fig. 1.6). They found that changing the ratio of GO:linker produced different textural properties of the products including interlayer distances, pore sizes, specific surface areas. The GOF structure with one linker per 32 graphene carbons was theoretically predicted to hold ~6.1 wt % of H_2 at 77 K and 1 bar. And the experimental result of the COF prepared with 1:1 (GO:linker) showed a SSA of 470 m^2 g^{-1} and H_2 uptake of 1.2 wt % at 77 K and 6 bar.[76] Following the similar methodology, while using other chemical linkers, like sylsesquioxane [77] or physical spacers, like MWCNTs,[78] Pd nanoparticles,[79,80,81,82] clay [83,84] and MOF particles [85,86] could also achieve the same aim of adjusting the GO interlayer distances, thus affecting the material textural properties. These functionalized GO materials usually showed improved H_2 storage performances compared with GO.

1.3.3 Others

Besides MOFs and porous carbons materials, there are other porous material systems also reported for the application in H_2 physisorption, such as porous polymers, zeolites,[87] porous silica,[88] *etc*. Porous polymers derived for H_2 storages usually contain intrinsic micropores, so called Polymers of Intrinsic Microporosity (PIMs).[89] This is achieved by a design of the monomer structure forming the final PIM product which is assembled into highly porous morphology. The recently reported microporous polycarbazole obtained by straightforward carbazole-based oxidative coupling polymerization exhibited a specific surface area up to 2220 m^2 g^{-1}. H_2 adsorption isotherms showed a 2.80 wt % uptake at 1.0 bar and 77 K.[90] Corti *et al.* reported the growth of silica nanosprings made of multiple nanowires inter-twined by a modified vapor–liquid–solid method. It was demonstrated that they are able to reversibly store 0.85 wt% hydrogen at 20 bar and room temperature. A Pd nanoparticle coating of the silica nanosprings leads to storage of nearly 3.5 wt % at 66 bar at room temperature.[88] above

1.3.4 Advantages of porous boron nitride for hydrogen storage

As was discussed in section 1.1, B-N bond shows a partially ionic nature due to the relatively higher electronegativity of the N atom. Such property of *h*-BN materials was theoretically pointed out to be advantageous for H_2 adsorption. Jhi *et al.* studied H_2 molecule adsorption on BN nanotubes using the pseudopotential density functional method.[91] They computed that the binding energy of hydrogen on BN sheet surface is 90 meV (8.7 kJ mol^{-1}), which is much higher than that in graphite (60 meV) due to the heteropolar bonding in boron nitride; *i.e.*, a ~50 % rise. As to the BNNTs, its binding energy increased by 40% compared to that on carbon nanotubes. Substitution doping and structural defects were predicted to be favorable for hydrogen adsorption.

Usually, placing a molecule in pores will result in a higher adsorption heat than in case of plane surfaces. This is due to a fact that the interactions between the adsorbates and the solid surface are stronger; the adsorbates can be attracted by many more surface atoms of the pore walls. Thus, developing porous BN materials with a suitable pore size and structure, as well as with high SSAs, is a very meaningful and practical approach for a design of better H_2 accumulators. Recent progress in theoretical calculations showed a modeled stable porous BN structure could reach a SSA of 4800 m^2 g^{-1},[92,93] indicating the remained large potentials toward the further improvement of the BN material textural properties.

1.4 Porous boron nitride materials

1.4.1 Preparation strategies

Many methods had been developed for fabrication of porous BN materials, which could be divided into two categories, based on whether the templates were involved during the synthesis, namely, template directing method and non-template method. The former is a prime strategy for the preparation of porous materials. And many templates have been developed and applied for the preparation of porous BNs. While the latter strategy grabbed the full attention in recent years based on the direct reactions of interacted B- and N-precursors; this strategy is featured by its simple, one-step process and free of harmful post-treatments required.

1.4.1.1 Template directing method

Like the preparation methods for other porous materials, porous BN could be obtained using soft-/hard-template directing synthesis. Numerous templates, such as silica, activated carbons, graphene aerogel, zeolite, cationic surfactant, and block copolymer were used as templates for the preparation of porous BNs. The SSAs of these porous BNs reportedly ranged from 100 to 950 $m^2 g^{-1}$.

In 2004, Han *et al.* reported (using an activated carbon as the template, B_2O_3 and N_2 as the B- and N-sources) on the preparation of porous BN under high temperature. The SSA of the received porous BN product was 167.8 $m^2 g^{-1}$, obviously smaller than that of the used activated carbon template (779 $m^2 g^{-1}$).[94] Such phenomena (inefficient filling of the pores in the used template by precursors and the resultant reduced SSAs) were confirmed to be very common for the methods which use hard-templates for the preparation of porous BNs. Later, numerous ordered mesoporous carbon materials were adopted as the hard templates. Meile *et al.* nanocasted an organic BN precursor of tri(methylamino)borazine (MAB) to mesoporous silica (SBA-15) and carbon (CMK-3) templates. After thermal treatment and the removal of the hard templates using an ammonia thermal treatment (for the carbon template) or an HF treatment (for the silica template), the porous BNs were obtained. Ordered mesoporous BN with a pore width of 3.4 nm and the SSA of 540 $m^2 g^{-1}$ was prepared using CMK-3 as the template. As a comparison, using silica template was confirmed to be inefficient to obtain the BN replica due to the hydrophilic nature of the silica.[95] They also utilized different porous carbons as the templates for the same purpose; the obtained products displayed hierarchical porosity with a SSA of ~300 $m^2 g^{-1}$.[96] Similarly, Vinu *et al.* also produced the ordered mesoporous BN that was templated from the mesoporous carbons using B_2O_3 and N_2 as the B- and N-sources. Both TEM and N_2 adsorption isotherms confirmed the ordered porous features of the product, which exhibited a SSA of 565 $m^2 g^{-1}$ and a pore width of 2.7 nm. [97] More recently, Parmentier *et al.* fabricated the porous carbon templated from zeolite Y (FAU structure type) that could also be suitable as a template for the further synthesis of porous BNs. These obtained porous BN architectures exhibited a high portion of micropores (~0.20 $cm^3 g^{-1}$) and a high specific area (570 $m^2 g^{-1}$), and a pore volume (0.78 $cm^3 g^{-1}$).[98] See Figure 1.7.

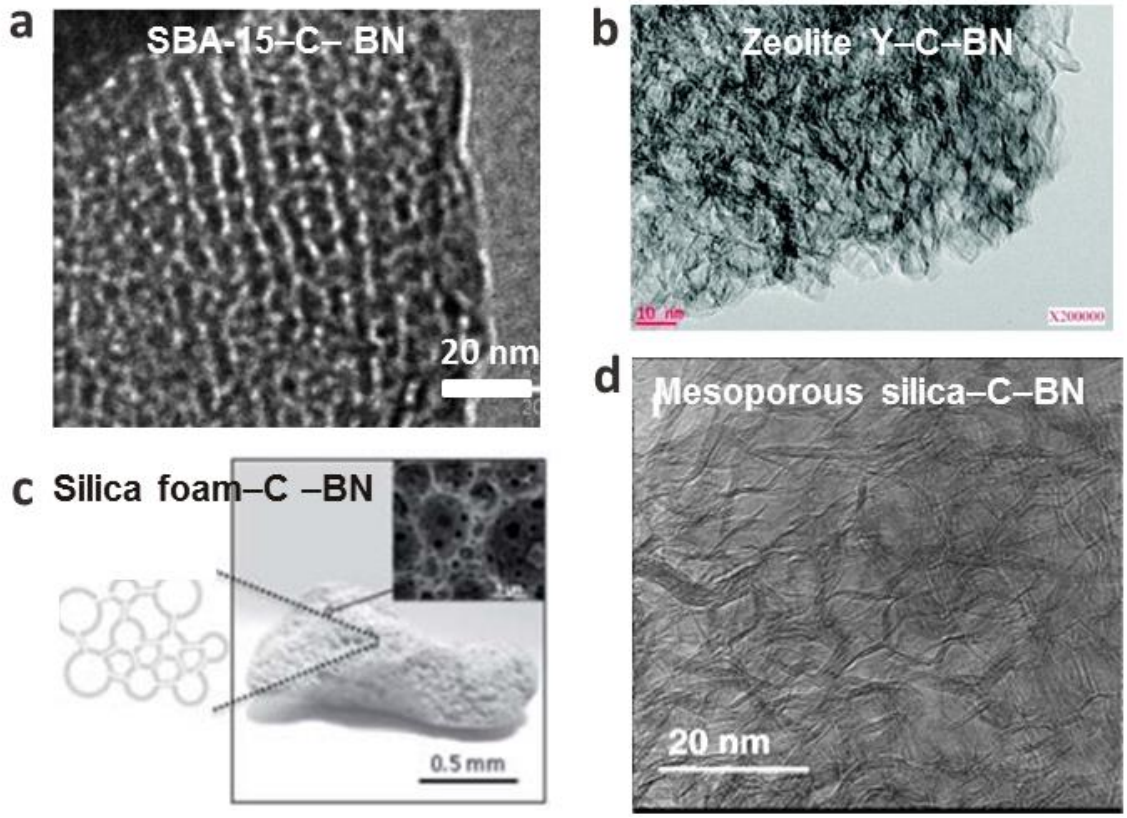

Figure 1.7 Porous BN materials templated from different hard templates via carbonaceous intermediates: SBA-15 (a, Ref. 95), Zeolite Y (b, Ref. 98), silica foam (c, Ref. 96), and mesoporous silica (d, Ref. 97).

Since the used mesoporous carbon hard templates are always prepared from mesoporous silica, using mesoporous silica directly is advantageous from the point of reducing the number of steps in the preparation. To improve the filling efficiency, Mokaya *et al.* selected ammonia borane (BH_3NH_3) as the BN precursor to infiltrate a SBA-15 template. After the removal of the template, the resultant textural properties of the received porous BNs were relatively high (surface area of 327 $m^2\ g^{-1}$ and pore volume of 0.50 $cm^3\ g^{-1}$), indicating the better filling performances of these small ammonia borane molecules.[99]

Besides the hard-templates discussed above, using soft-templates for directing porous BNs was also explored. Taken the advantage of polycondensation property of MAB, Meile *et al.* heated a MAB precursor in CTAB solution (a kind of surfactant) at 120 ℃ for 7 days to form a transparent gel. After eliminating the solvent and ceramization under ammonia at 1000 ℃, highly porous BN product with the SSA of 800 $m^2\ g^{-1}$, pore width of 6 nm, and mesoporous volume of 0.5 $cm^3\ g^{-1}$ was synthesized.[100] By designing a hybrid organic–inorganic block copolymer of polynorbornene–decaborane, and utilizing its self-assembly property in tetrahydrofuran (THF), Malenfant *et al.* synthesized ordered porous BN nanostructures with a pore size dominated at ~20 nm and a record-high SSA of 950 $m^2\ g^{-1}$ at that time,[101] see Figure 1.8.

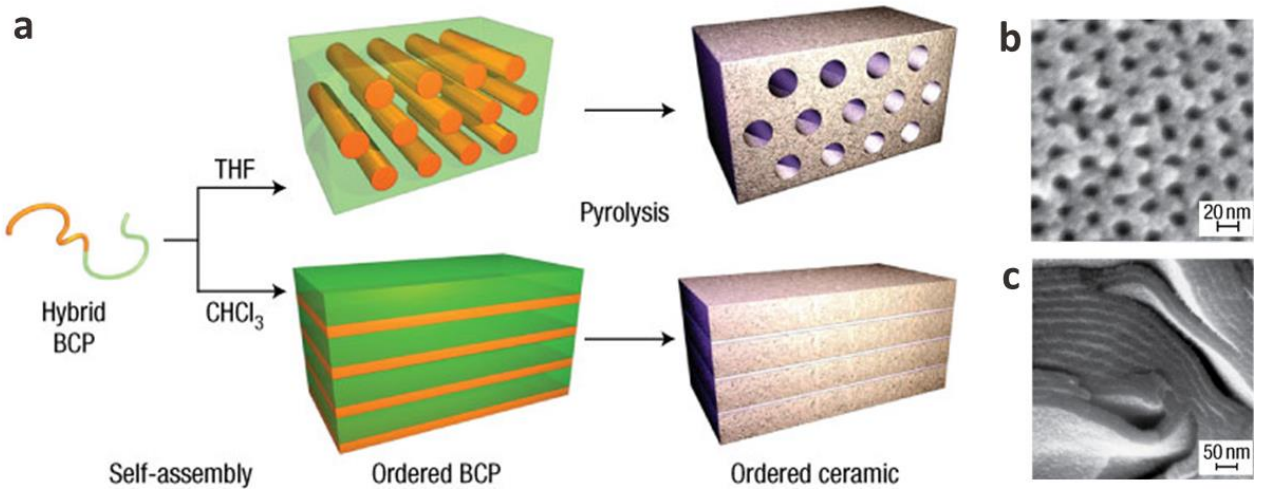

Figure 1.8 Illustration of the self-assembly and pyrolysis of a block copolymer (PNB-b-PDB30) that consists of a polynorbornene (PNB) segment and a decaborane-based one (PDB). SEM images of the obtained ordered porous BNs originating from the self-assembled PNB-b-PDB30 cast from THF (b) and chloroform (c) after pyrolysis to 1000 ℃ in ammonia. (Ref. 101)

1.4.1.2 Non-template synthesis

In the last two years, the strategies based on non-template one-step reactions witnessed a remarkable progress. As will be introduced as the main topic (later in this Thesis), my achievements include obtaining the first pure BN material with the SSA over 1000 m^2 g^{-1} by the one-step reaction of a boric acid-melamine (2B-M) precursor. Under the optimized conditions, the SSA of this microbelt-like porous BN sample reached a value as high as 1488 m^2 g^{-1}.[16] Such high SSA and porosity for this 2B-M derived porous BNs were later independently confirmed by other research groups.[102,103] Using other precursor systems, such as H_3BO_3-dicyandiamide, led to the unprecedented super-high SSAs, up to 1900 m^2 g^{-1}, for the obtained porous BN materials.[104] Besides, recently, the porous BN sheets prepared from a B_2O_3-guanidine hydrochloride precursor were also reported to have a very high SSA of 1425 m^2 g^{-1}. An additional information on the development of this field during the last two years will be finally given in Summary and Outlook Chapter. In this portion, I primarily focused on the research background and the field status before my PhD work had been started.

In 2004, Osterwalder *et al.* discovered a peculiar mesh pattern of hexagonal BN with a 3 nm periodicity and a 2 nm pore size on a Rh(111) single crystalline surface after a high-temperature exposure to borazine $(HBNH)_3$.[105,106] The BN nanomesh composes of two offset layers to have a minimum metal surface area and is considered to be formed by the lattice mismatch between the film and Rh substrate (Figure 1.9). Using other Rh surface like (0001) led to the formation of a single layer BN nanomesh.[107,108] Such nanostructures are very thermally stable. Their pores were found to uptake C_{60}, organic molecules with the matching size,[109] and Au nanoparticles.[110,111]

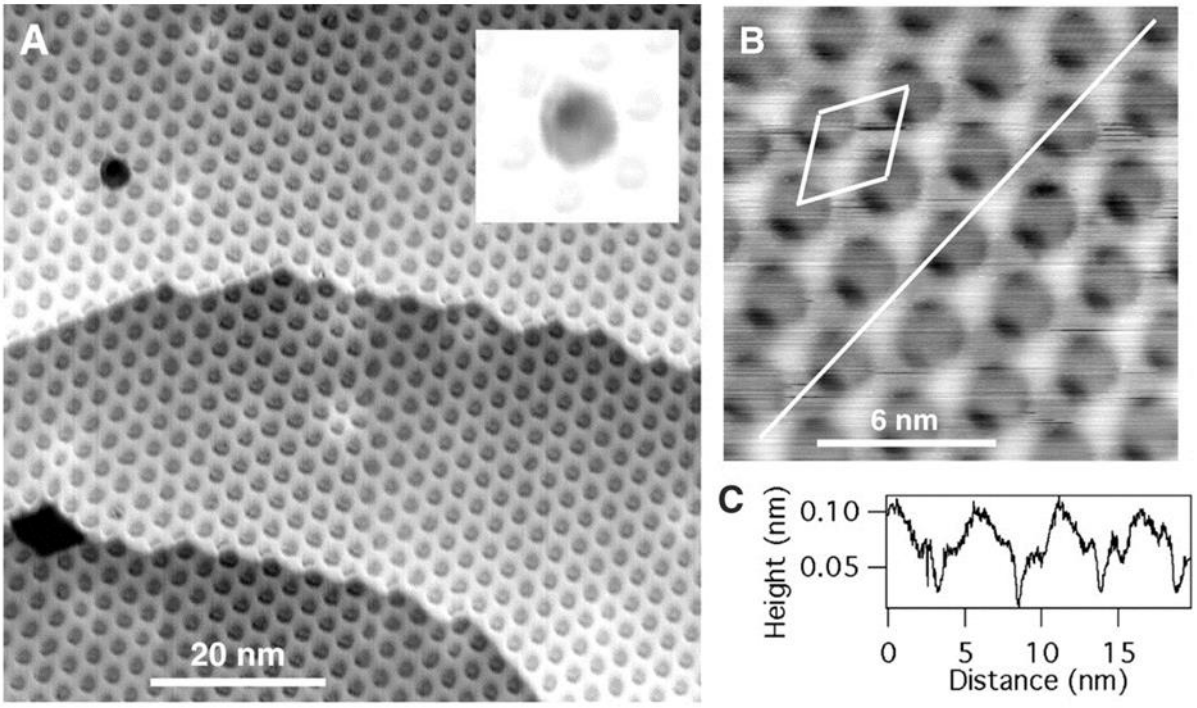

Figure 1.9 (a) STM images of a BN nanomesh prepared via high-temperature decomposition of borazine on a Rh(111) surface. The inset is the enlarged defect area. (b) High-resolution STM image of the BN nanomesh, showing the presence of two offset layers on Rh(111) surface. (c) Cross-sectional profile along the diagonal white line in (b). Reproduced from Ref. 105.

Qian *et al.* developed a sealed reaction of solid B- and N-precursors in an autoclave at a moderate temperature to prepare the porous BN materials.[112,113,114] They chose various H_3BO_3, $Na_2B_4O_7$, $NH_4HB_4O_7$ and $Mg(BO_2)_2$ reagents as the B-precursor, NaN_3 as the N-precursor and Mg as the reducing agent for this reaction. The yielded products contained micro-sized pores. When using the other recipe consisting of KBH_4, NH_4F and Zn, BN hollow submicro-boxes were received with the SSA of 87 m^2 g^{-1}. Lately, they found that the presence of sulfur in the reaction between NH_4BF_4 and Fe was helpful to the formation of dense macropores in the products. And the SSA of the product was also improved to 230 m^2 g^{-1}. Yin and Bai *et al.* investigated the reactions between $NaBH_4$ and $CO(NH_2)_2$/$CS(NH_2)_2$ at a moderate temperature of 550 ^oC using the same synthesis technique. After the post-purification treatments, porous BNs with SSAs of ~220 m^2 g^{-1} were obtained.[115,116]

An ideal single-layered *h*-BN sheet theoretically has a SSA of ~2600 m^2 g^{-1}. Also, due to the loose stacking of BN layers, it is possible to form slit-shaped pores between or among the BN layers in the experimentally obtained BN nanosheets. In 2010, Rao *et al.* invented synthesis of sheet-like BNs from the direct reaction between boric acid and urea at different mass ratios. They found that the SSAs of the products had increased along with the increase of the precursor ratio of urea to boric acid. At the optimized condition, the received sheet-like BN product exhibited a high SSA of up to 927 m^2 g^{-1}, which was the highest SSA

value among all non-template-derived BNs,[117] see Figure 1.10. More recently, our group has also made a decent progress in the macroscopic preparation of BN nanosheets by thermal polymerization of BH_3NH_3 (Figure 1.10). The obtained product showed a hierarchical pore structure with SSA of 140 m^2 g^{-1}.[52]

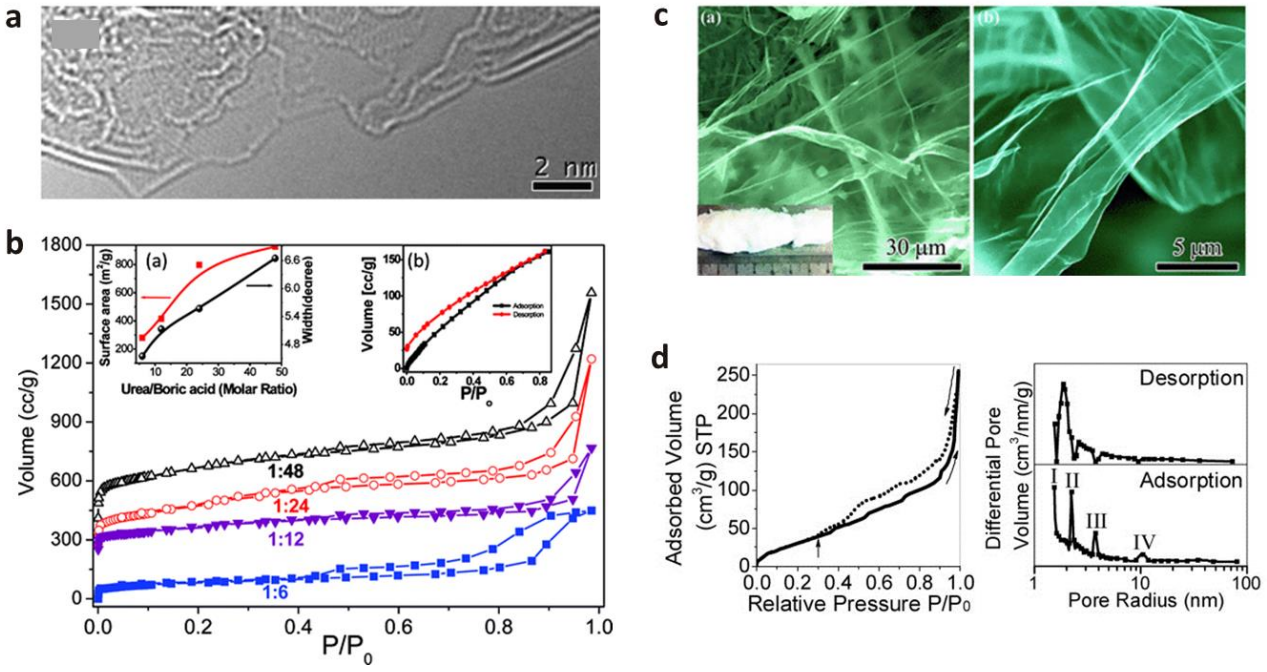

Figure 1.10 Structures and N_2 adsorption-desorption isotherms of BN nanosheets. (a,b) TEM image and textural measurement of BN nanosheets (Ref. 117). (c,d) SEM images and textural measurement of BN nanosheets prepared from ammonia borane (Ref. 52)

1.4.2 Research status of porous boron nitrides for hydrogen storage

Researches on nanostructured BN materials for H_2 storage could be tracked back to 2002 after the technique of macroscopic preparation of BNNTs was realized in our lab.[118] Ma *et al.* investigated H_2 uptake performances of the BN nanotubes with different morphologies. One is the normal BN multiwalled nanotubes and the other is the bamboo-like nanotubes. They found that the bamboo-like and multiwalled BNNTs could uptake 2.6 and 1.8 wt % H_2 under 10 MPa at room temperature (Figure 1.11). One problem using BNNTs for H_2 storage, as the authors pointed out, is that ~70 wt % of the adsorbed hydrogen was retained in the material after the system was recovered to ambient pressure. The retained amount of hydrogen was only released when the structures were heated to 573 K, suggesting that the majority of hydrogen was likely chemisorbed at such high pressure.[119]

Later, Tang *et al.* found that such irreversible H_2 uptake capacity could be increased up to 4.2 wt % at the same testing conditions after the BNNT surfaces were activated *via* Pt catalysis to form a collapsed hair-like surface morphology (Figure 1.11). It is understandable that the BNNT SSA could be improved from 254.2 to 789.1 m^2 g^{-1} after this activation process, and this would be helpful to enhance the H_2 sorption performance

of the samples. And similarly, most of the H_2 molecules were found to be chemisorbed and needed a high temperature to be released.[120] Such respectively high uptake capacity was later found to be partially due to the co-contribution of BNNTs and residual Pt particles introduced during the activation process. Because similarly collapsed BNNTs activated through another route (using SO_2 at a high temperature) showed very limited H_2 uptake: ~0.6 wt % at 2 MPa and 77 K.[121]

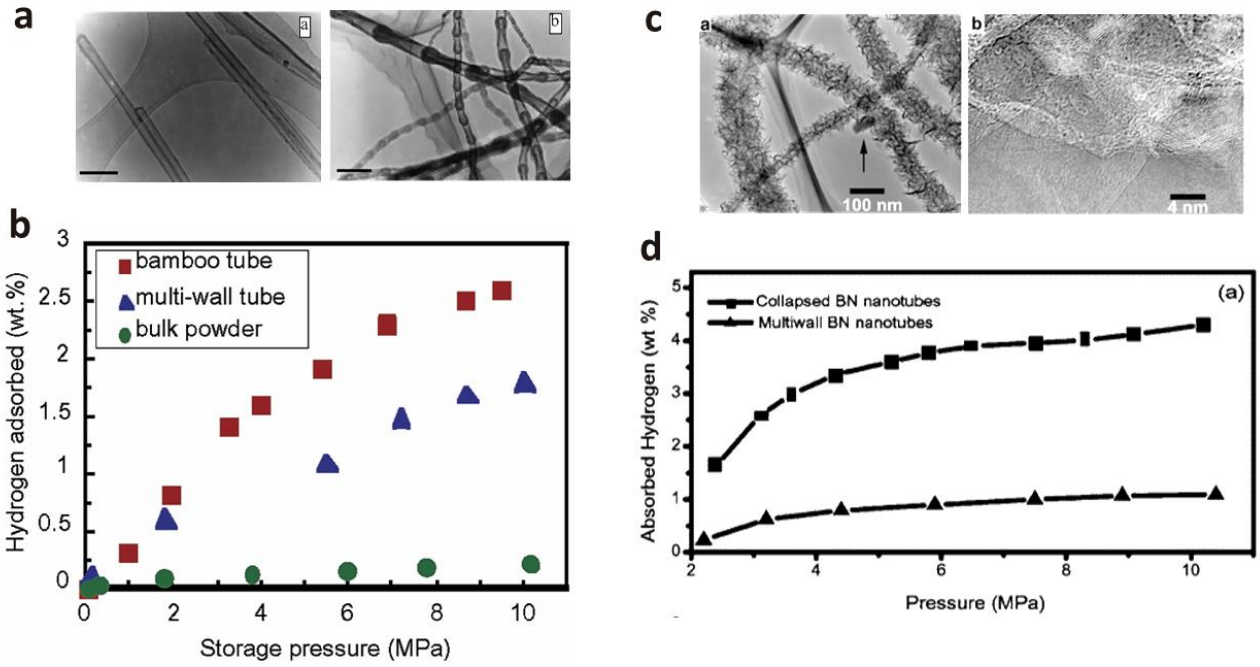

Figure 1.11 Hydrogen uptake performances of different BN nanotubes. (a) TEM images of multiwalled BNNTs and bamboo-like BNNTs. (b) H_2 adsorption isotherms of the tube samples at room temperature. (c) TEM images of the collapsed BNNTs. (d) Comparison of the H_2 adsorptions of the collapsed BNNTs and multiwalled BNNTs at room temperature. (a,b) are reproduced from Ref. 119. (c,d) are reproduced from Ref. 120.

Lin *et al.* used a ball-milling of boron-nickel catalyst in nitrogen/hydrogen gas mixture at 1025 ^{o}C for the synthesis of BNNTs. The BNNTs were found to uptake a reproducible H_2 capacity of 1.8–2.2 wt % under 6 MPa and room temperature. They conducted a temperature-programmed desorption analysis and found that 50% of the adsorbed hydrogen on the BNNTs had been chemisorbed, which could be released at a temperature of 250 ^{o}C.[122]

More recently, the advances on H_2 storage studies of BN materials have been focused on the design of hollow and porous BN materials. Portehault *et al.* developed a pyrolysis method starting from a complex-filled borane (as the B source) and a mesoporous graphitic carbon nitride (as the N source) to prepare the porous BCN materials. The as-prepared products possessed very high surface areas, up to 1560 m^2 g^{-1}. This reactive hard-template approach assures tunable composition and texture for the products. It was documented that these compounds had exhibited H_2 uptakes from 0.55 to 1.07 wt % at 77 K and 100 kPa (Figure 1.12).[123]

Lian *et al.* reported the synthesis of BN hollow spheres with thin shells (1–3 nm) using a template-free sealed reaction between NH_4BF_4, NaN_3 and 0.64 g sulphur (S) in an autoclave. The prepared BN hollow spheres possessed high specific surface area up to 215 m^2 g^{-1} and large pore volume, and exhibited a relatively high hydrogen uptake capacity, up to 4.07 wt % at 298 K and 10 MPa (Figure 1.11).[21]

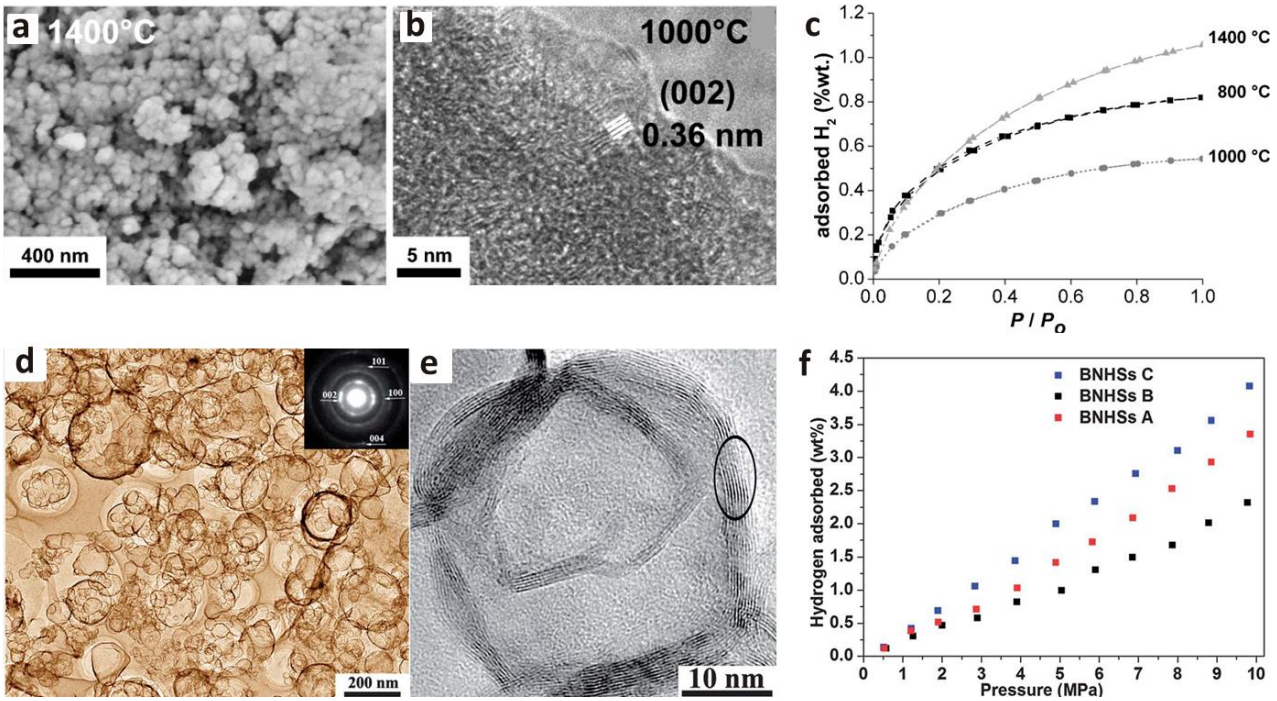

Figure 1.12 (a) SEM images of BCN materials obtained after pyrolysis of borane complex-filled mesoporous graphitic carbon nitride at 1400 °C. (b) TEM image of the sample obtained after 1000 °C treatment. (c) H_2 sorption isotherms of the porous BCN materials with different temperature treatments. (d,e) TEM and HRTEM images of BN hollow spheres prepared from a sealed solid reaction. (f) H_2 uptake capacities of BNHSs with different shell thickness at 298 K. From A to C, the shell thickness decreased from 8~10 to 1~3 nm. (a-c) are reproduced from Ref. 123, (d-f) are reproduced from Ref. 21.

1.4.3 Challenges in this field and the motivation of my dissertation

Although the initial efforts to prepare porous BN materials were initiated quite early, notable breakthroughs along the preparation routes toward highly porous BN materials with high SSAs were rather scare compared with those natural for other porous material systems in the last 10 years. One may find that until 2012, the highest SSA for BN materials was only 950 m^2 g^{-1}, which is far below the cutting-edge values reported for porous carbons and MOF materials. Certainly, these textural properties are not sufficient for the purpose of H_2 storage applications. We attribute the main reasons behind this situation to the chemical inertness of BN materials, limited choices for suitable precursors, and a more difficult control of the chemical reactions involved.

The inert chemical nature of *h*-BN material limits the preparation possibilities of the porous structures *via* a top-down etching reaction way. Such route is very common and effective for the preparation of porous carbon materials. In addition, due to the rich source of carbon and MOF precursors, there are almost infinite possibilities and combinations of these different precursors chosen for the bottom-up growths. Very differently, for the BN system, suitable precursors which can provide B and N source are rather limited, especially for B precursors. Since BN materials are composed of equal molar contents of B and N components, it is not easy to calculate the precise ratios of the B- and N- precursors to get the right B/N balance in the final products. And the synthesis processes are also influenced by many additional factors, such as reaction atmosphere, heating rate, *etc*, making them even more difficult to be well controlled.

To address the challenges faced in this field, I have developed original and simple one-step template-free methods to prepare highly porous BN materials. In this Thesis, several B- and N- precursor adducts with molecular-level interactions have been discovered, including the adducts of boric acid-melamine and boric acid-dicyandiamide. Further reactions of these novel adducts have led to the formations of hierarchically porous BN microbelts with the SSA up to 1488 $m^2 g^{-1}$ (Chapter 2), microporous BN microsponges with the SSA up to 1900 $m^2 g^{-1}$ (Chapter 3), and pore width- and composition-tunable BCNO microbelts (Chapter 4). Numerous factors that can affect the resultant textural properties of the products have been explored and discussed, and finally optimized for the fabrication of porous BNs; these factors include temperature, precursor ratio, and reaction atmosphere. H_2 adsorption measurements on these porous BN materials have revealed high and reversible uptake capacity up to 2.60 wt % at 1 MPa and 77 K, which corresponds to a gravimetric energy capacity of ~0.87 kWh kg^{-1}. The correlations of SSA, pore width, and chemical composition of the materials with H_2 uptake capacity have finally been carefully studied.

I believe that the developed simple and effective synthesis methods designed in this Thesis for fabrication of highly porous BN materials open the door toward designing practical H_2 accumulators based on novel porous BN systems. More porous BN materials with higher SSAs and pore volumes are envisaged to be found in the near future. With much easier accessibility to highly porous BN materials, establishment of the quantitative correlations between the material textural parameters and its H_2 uptake capacities can be foreseen, which will in turn guide the more efficient designs and which produce better BN H_2 accumulators.

1.5 References

1 "BN – Boron Nitride". Ioffe Database. Sankt-Peterburg: FTI im. A. F. Ioffe, RAN.

2 Paine, R.; Narula, C. *Chem. Rev.*, **1990**, *90*, 73–91.

3 Chen, S.; Wu, Q.; Mishra, C.; Kang, J.; Zhang, H.; Cho, K.; Cai, W.; Balandin, A. A.; Ruoff, R. S. *Nature Mater*., **2012**, *11*, 203.

4 Both intra-planar and inter-planar electron transports of graphitic layers behave like linear Ohmic characteristic at small voltages.

5 Stephan, O.; Bando, Y.; Loiseau, A.; Willaime, F.; Shramchenko, N.; Tamiya, T.; Sato, T. *Appl. Phys. A-Mater*., **1998**, *67*, 107.

6 Golberg, D.; Bando, Y.; Stephan, O.; Kurashima, K. *Appl. Phys. Lett*., **1998**, *73*, 2441.

7 Chopra, N. G.; Luyken, R.J.; Cherrey, K.; Crespi, V. H.; Cohen, M. L.; Louie, S. G.; Zettl, A. *Science*, **1995**, *269*, 966.

8 Novoselov, K. S.; Jiang, D.; Schedin, F.; Booth, T. J.; Khotkevich, V. V.; Morozov, S.V.; Geim, A. K. *P. Natl. Acad. Sci. USA*, **2005**, *102*, 10451.

9 Corso, M.; Auwarter, W.; Muntwiler, M.; Tamai, A.; Greber, T.; Osterwalder, J. *Science*, **2004**, *303*, 217.

10 Tang, C. C.; Bando, Y.; Huang, Y.; Zhi, C. Y.; Golberg, D. *Adv. Funct. Mater*., **2008**, *18*, 3653.

11 Huo, K. F.; Hu, Z.; Chen, F.; Fu, J. J.; Chen, Y.; Liu, B. H.; Ding, J.; Dong, Z. L.; White, T. *Appl. Phys. Lett*., **2002**, *80*, 3611.

12 Chen, Y. J.; Zhang, H. Z.; Chen. Y. *Nanotechnology*, **2006**, *17*, 786.

13 Zhang, H. Z.; Yu, J.; Chen, Y.; Gerald, J. F. *J. Am. Ceram. Sos*., **2006**, *89*, 675.

14 Qiu, Y. J.; Yu, J.; Yin, J.; Tan, C. L.; Zhou, X. S.; Bai, X. D.; Wang, E. G. *Nanotechnology*, **2009**, *20*, 345603.

15 Chen, Z. G.; Zou, J.; Liu, G.; Li, F.; Wang, Y.; Wang, L. Z.; Yuan, X. L. Sekiguchi, T.; Cheng, H. M.; Lu, G. Q. *ACS Nano*, **2008**, *2*, 2183.

16 Weng, Q. H.; Wang, X. B.; Zhi, C. Y.; Bando, Y.; Golberg, D. *ACS Nano*, **2013**, *7*, 1558.

17 Han, W. Q.; Bando, Y.; Kurashima, K.; Sato, T. *Jpn. J. Appl. Phys*., **1999**, *38*, L755.

18 Wu, H. S.; Cui, X. Y.; Qin, X. F.; Strout, D. L. Jiao, H. *J. Mol. Model*., **2006**, *12*, 537.

19 Pan, Y.; Huo, K.; Hu, Y.; Fu, J.; Lu, Y.; Dai, Z.; Hu, Z.; Chen, Y. *Small*, **2005**, *1*, 1199.

20 Pupysheva, O.V.; Farajian, A. A.; Yakobson, B. I. *Nano Lett*., **2008**, *8*, 767.

21 Lian, G.; Zhang, X.; Zhang, S. J.; Liu, D.; Cui, D. L.; Wang, Q. L. *Energy Environ. Sci*., **2012**, *5*, 7072.

22 Huang, Y.; Lin, J.; Tang, C.; Bando, Y.; Zhi, C.; Zhai, T.; Dierre, B.; Sekiguchi, T.; Golberg, D. *Nanotechnology*, **2011**, *22*, 145602.

23 Zeng, H.; Zhi, C.; Zhang, Z.; Wei, X.; Wang, X.; Guo, W.; Bando, Y.; Golberg, D. *Nano Lett*., **2010**, *10*,

5049.

24 Loiseau, A.; Willaime, F.; Demoncy, N.; Hug, G. Pascard, H. *Phys. Rev. Lett*., **1996**, *76*, 4737.

25 Zhi, C.; Bando, Y.; Terao, T.; Tang, C.; Kuwahara, H.; Golberg, D. *Adv. Funct. Mater*., **2009**, *19*, 1857.

26 Huang, Q.; Bando, Y.; Xu, X.; Nishimura, T.; Zhi, C.Y.; Xu, F. F.; Golberg, D. *Proc. 16th Int. Conf. on Composite Materials*, Kyoto, Japan, July 8-13 **2007**, 810.

27 Yamaguchi, M.; Tang, D. M.; Zhi, C.; Bando, Y.; Shtansky, D.; Golberg, D. *Acta Mater*., **2012**, *60*, 6213.

28 Huang, X.; Zhi, C.; Jiang, P.; Golberg, D.; Bando, Y.; Tanaka, T. *Adv. Funct. Mater*., **2013**, *23*, 1824.

29 Tang, C. C.; Bando, Y.; Ding, X. X.; Qi, S. R.; Golberg, D. *J. Am. Chem. Soc.*, **2002**, *124*, 14550.

30 Golberg, D.; Dorozhkin, P.; Bando, Y.; Hasegawa, M.; Dong, Z. C. *Chem. Phys. Lett.*, **2002**, *359*, 220.

31 Golberg, D.; Dorozhkin, P. S.; Bando, Y.; Dong, Z. C.; Tang, C. C.; Uemura, Y.; Grobert, N.; Reyes-Reyes, M.; Terrones, H.; Terrones, M. *Appl. Phys. A*, **2003**, *76*, 499.

32 Huang, Y.; Bando, Y.; Tang, C.; Zhi, C.; Terao, T.; Dierre, B.; Sekiguchi, T.; Golberg, D. *Nanotechnology*, **2009**, *20*, 085705.

33 Li, X.; Hanagata, N.; Wang, X.B.; Yamaguchi, M.; Yi, W.; Bando. Y.; Golberg, D. *Chem. Commun*., **2014**, *50*, 4371.

34 Pacile, D.; Meyer, J. C.; Girit, C. O.; Zettl, A. *App. Phys. Lett*., **2008**, *92*, 133107.

35 Nagashima, A.; Tejima, N.; Gamou, Y.; Kawai, T.; Oshima, C. *Phys. Rev. Lett*., **1995**, *75*, 3918.

36 Song, L.; Ci, L. J.; Lu, H.; Sorokin, P. B.; Jin, C. H.; Ni, J.; Kvashnin, A. G.; Kvashnin, D. G.; Lou, J.; Yakobson, B. I.; Ajayan, P. M. *Nano Lett*., **2010**, *10*, 3209.

37 Kim, K. K.; Hsu, A.; Jia, X. T.; Kim, S. M.; Shi, Y. S.; Hofmann, M.; Nezich, D.; Rodriguez-Nieva, J.F.; Dresselhaus, M.; Palacios, T.; Kong, J. *Nano Lett*., **2012**, *12*, 161.

38 Shi, Y. M.; Hamsen, C.; Jia, X. T.; Kim, K. K.; Reina, A.; Hofmann, M.; Hsu, A.L.; Zhang, K.; Li, H. N.; Juang, Z. Y.; Dresselhaus, M. S.; Li, L. J.; Kong, J. *Nano Lett*., **2010**, *10*, 4134.

39 Yu, J.; Qin, L.; Hao, Y. F.; Kuang, S.; Bai, X. D.; Chong, Y. M.; Zhang, W. J.; Wang, E. *ACS Nano*, **2010**, *4*, 414.

40 Pakdel, A.; Wang, X. B.; Zhi, C. Y.; Bando, Y.; Watanabe, K.; Sekiguchi, T.; Nakayama, T.; Golberg, D. *J. Mater. Chem*., **2012**, *22*, 4818.

41 Dean, C. R.; Young, A. F.; Meric, I.; Lee, C.; Wang, L.; Sorgenfrei, S.; Watanabe, K.; Taniguchi, T.; Kim, P.; Shepard, K. L. Hone, J. *Nature Nanotech*., **2010**, *5*, 722.

42 Giovannetti, G.; Khomyakov, P. A.; Brocks, G.; Kelly, P. J.; D.Brink, J. V. *Phys. Rev. B*, **2007**, *76*, 073103.

43 Slawinska, J.; Zasado, I.; Klusek, Z. *Phys. Rev. B*, **2010**, *81*, 155433.

44 Ponomarenko, L. A.; Geim, A. K.; Zhukov, A. A.; Jalil, R.; Morozov, S. V.; Novoselov, K. S.; Grigorieva, I. V.; Hill, E. H.; Cheianov, V. V.; Fal'ko, V. I.; Watanabe, K.; Taniguchi, T.; Gorbachev, R. V. *Nature Phys*., **2011**, *7*, 958.

45 Gorbachev, R. V.; Geim, A. K.; Katsnelson, M. I.; Novoselov, K. S.; Tudorovskiy, T.; Grigorieva, I. V.; MacDonald, A. H.; Morozov, S. V.; Watanabe, K.; Taniguchi, T.; Ponomarenko, L. A. *Nature Phys*., **2012**, *8*, 896.

46 Britnell, L.; Gorbachev, R. V.; Jalil, R.; Belle, B. D.; Schedin, F.; Katsnelson, M. I.; Eaves, L.; Morozov, S. V.; Mayorov, A. S.; Peres, N. M. R.; Neto, A. H. C.; Leist, J.; Geim, A. K.; Ponomarenko, L. A.; Novoselov, K. S. *Nano Lett*., **2012**, *12*, 1707.

47 Pan, W.; Xiao, J.L.; Zhu, J. W.; Yu, C. X.; Zhang, G.; Ni, Z. H.; Watanabe, K.; Taniguchi, T.; Shi, Y.; Wang, X. R. *Sci. Rep*., **2012**, *2*, 893.

48 Shi, G.; Hanlumyuang, Y.; Liu, Z.; Gong, Y.; Gao, W.; Li, B.; Kono, J.; Lou, J.; Vajtai, R.; Sharma, P.; Ajayan, P. M., *Nano Lett*., **2014**, *14*, 1739.

49 Pakdel, A.; Wang, X.B.; Bando, Y.; Golberg, D. *Acta Mater*., **2013**, *61*, 1266.

50 Liu, Z.; Gong, Y.; Zhou, W.; Ma, L.; Yu, J.; Idrobo, J. C.; Jung, J.; MacDonald, A. H.; Vajtai, R.; Lou, J.; Ajayan, P. M. *Nat. Commun*., **2013**, *4*, 2541.

51 Wang, X. B.; Zhi, C. Y.; Li, L.; Zeng, H. B.; Li, C.; Mitome, M.; Golberg, D.; Bando, Y. *Adv. Mater*., **2011**, *23*, 4072.

52 Wang, X.B.; Pakdel, A.; Zhang, J.; Weng, Q. H.; Zhai, T. Y.; Zhi, C. Y.; Golberg, D.; Bando, Y. *Nanoscale Res. Lett*., **2012**, *7*, 662.

53 Wang, X. B.; Zhi, C. Y.; Weng, Q. H.; Bando, Y.; Golberg, D. *J. Phys.: Conf. Ser*., **2013**, *471*, 012003.

54 Wang, X.B.; Pakdel, A.; Zhi, C.Y.; Watanabe, K.; Sekiguchi, T.; Golberg, D.; Bando, Y. *J. Phys.: Condens. Matter*, **2012**, *24*, 314205.

55 Watanabe, K.; Taniguchi, T.; Niiyama, T.; Miya, K.; Taniguchi, M. *Nature Photon*., **2009**, *3*, 591.

56 Watanabe, K.; Taniguchi, T.; Kanda, H. *Nature Mater*., **2004**, *3*, 404.

57 Lee, C.; Li, Q.; Kalb, W.; Liu, X. Z.; Berger, H.; Carpick, R.W.; Hone, J. *Science*, **2010**, *328*, 76.

58 Suh, M.; Park, H; Prasad, T.; Lim, D. *Chem. Rev.*, **2012**, *112*, 782.

59 Rosi, N. L.; Eckert, J.; Eddaoudi, M.; Vodak, D. T.; Kim, J.; O'Keeffe, M.; Yaghi, O. M. *Science* **2003**, *300*, 1127.

60 Farha, O. K.; Yazaydin, A. O.; Eryazici, I.; Malliakas, C. D.; Hauser, B. G.; Kanatzidis, M. G.; Nguyen, S. T.; Snurr, R. Q.; Hupp, J. T. *Nat. Chem.*, **2010**, *2*, 944.

61 Furukawa, H.; Ko, N.; Go, Y. B.; Aratani, N.; Choi, S. B.; Choi, E.; Yazaydin, A. O.; Snurr, R. Q.; O'Keeffe, M.; Kim, J.; Yaghi, O. M. *Science,* **2010**, *329*, 424.

62 Murray, L.; Dincă, M.; Long, J. *Chem. Soc. Rev.*, **2009**, *38*, 1294.

63 Wang, L.; Guo, Y.; Zou, B.; Rong, C.; Ma, X.; Qu, Y.; Li, Y.; Wang, Z. *Bioresour. Technol.*, **2011**, *102*, 1947.

64 Osswald, S.; Portet, C.; Gogotsi, Y.; Laudisio, G.; Singer, J. P.; Fischer, J. E ; Sokolov, V. V.; Kukushkina, J. A.; Kravchik, A. E. *J. Solid State Chem.*, **2009**, *182*, 1733.

65 Gogotsi, Y.; Portet, C.; Osswald, S.; Simmons, J. M.; Yildirim, T.; Laudisio, G.; Fischer, J. E. *Int. J. Hydrogen Energy*, **2009**, *34*, 6314.

66 Yeon, S.-H.; Osswald, S.; Gogotsi, Y.; Singer, J. P.; Simmons, J. M.; Fischer, J. E.; Lillo-Ródenas, M. A.; Linares-Solano, A.; *J. Power Sources*, **2009**, *191*, 560.

67 Sevilla, M.; Mokaya, R. *Energy Environ. Sci.*, **2014**, *7*, 1250.

68 Hu, M.; Reboul, J.; Furukawa, S.; Torad, N. L.; Ji, Q.; Srinivasu, P.; Ariga, K.; Kitagawa, S.; Yamauchi, Y. *J. Am. Chem. Soc.*, **2012**, *134*, 2864.

69 Kabbour, H.; Baumann, T. F.; Satcher, J. H.; Saulnier, A.; Ahn, C. C. *Chem. Mater.*, **2006**, *18*, 6085.

70 Wang, H.; Gao, Q.; Hu, J. *J. Am. Chem. Soc.*, **2009**, *131*, 7016.

71 Jordá-Beneyto, M.; Suárez-García, F.; Lozano-Castelló, D.; Cazorla-Amorós, D.; Linares-Solano, A. *Carbon*, **2007**, *45*, 293.

72 Wang, L.; Guo, Y.; Zou, B.; Rong, C.; Ma, X.; Qu, Y.; Li Y.; Wang, Z. *Bioresour. Technol.*, **2011**, *102*, 1947.

73 Osswald, S.; Portet, C.; Gogotsi, Y.; Laudisio, G.; Singer, J. P.; Fischer, J. E.; Sokolov, V. V.; Kukushkina, J. A.; Kravchik, A. E. *J. Solid State Chem.*, **2009**, *182*, 1733.

74 Gogotsi, Y.; Portet, C.; Osswald, S.; Simmons, J. M.; Yildirim, T.; Laudisio, G.; Fischer, J. E. *Int. J. Hydrogen Energy*, **2009**, *34*, 6314.

75 Yushin, G.; Dash, R.; Jagiello, J.; Fischer, J. E.; Gogotsi, Y. *Adv. Funct. Mater.*, **2006**, *16*, 2288.

76 Burress, J. W.; Gadipelli, S.; Ford, J.; Simmons, J. M.; Zhou, W.; Yildirim, T. *Angew. Chem. Int. Ed.*, **2010**, *49*, 8902.

77 Matsuo, Y.; Ueda, S.; Konishi, K.; Marco-Lozar, J. P.; Lozano-Castello, D.; Cazorla-Amoros, D. *Int J Hydrogen Energy*, **2002**, *37*, 10702.

78 Aboutalebi, S. H.; Aminorroaya-Yamini, S.; Nevirkovets, I.; Konstantinov, K.; Liu, H. K. *Adv. Energy Mater.*, **2012**, *2*, 1439.

79 Parambhath, V. B.; Nagar, R.; Sethupathi, K.; Ramaprabhu, S. *J Phys. Chem. C*, **2011**, *115*, 15679.

80 Parambhath, V. B.; Nagar, R.; Ramaprabhu, S. *Langmuir*, **2012**, *28*, 7826.

81 Vinayan, B. P.; Sethupathi, K.; Ramaprabhu, S. *Int. J Hydrogen Energy*, **2013**, *38*, 2240.

82 Vinayan, B. P.; Nagar, R.; Ramaprabhu, S. *J Mater. Chem. A*, **2013**, *1*, 11192.

83 Ruiz-García, C.; Pérez-Carvajal, J.; Berenguer-Murcia, A.; Darder, M.; Aranda, P.; Cazorla-Amorós, D. et al. *Phys. Chem. Chem. Phys.*, **2013**, *15,* 18635.

84 Ruiz-García, C.; Jiménez, R.; Pérez-Carvajal, J.; Berenguer-Murcia, A.; Darder, M.; Aranda, P. et al. *Sci. Adv. Mater.*, **2014**, *6*, 151.

85 Petit, C.; Burress, J.; Bandosz, T. J. *Carbon*, **2011**, *49*, 563.

86 Liu, S.; Sun, L.; Xu, F.; Zhang, J.; Jiao, C.; Li, F. et al. *Energy Environ. Sci.*, **2013**, *6*, 818.

87 Du, X.; Li, J.; Wu, E. *Progress in Chemistry*, **2010**, *22*, 248.

88 Corti, G.; Zhan, Y.; Wang, L.; Hare, B.; Cantrell, T.; Beaux II, M.; Prakash, T.; Ytreberg, M.; Miller, M.; McIlroy, D. *J. Phys. D: Appl. Phys.* **2013**, *46*, 505307.

89 McKeown, M.; Budd, P. *Chem. Soc. Rev.*, **2006**, *35*, 675.

90 Chen, Q.; Luo, M.; Hammershøj, P.; Zhou, D.; Han, Y.; Laursen, B. W.; Yan, C.-G.; Han, B.-H. *J. Am. Chem. Soc.*, **2012**, *134*, 6084.

91 Jhi, S. H.; Kwon, Y. K. *Phys. Rev. B*, **2004**, *69*, 245407.

92 Dai, J.; Wu, X.; Yang, J.; Zeng, X. C. *J. Phys. Chem. Lett.*, **2013**, *4*, 3484.

93 Dai, J.; Wu, X.; Yang, J.; Zeng, X. C. *J. Phys. Chem. Lett.*, **2014**, *5*, 393.

94 Han, W. Q.; Brutchey, R.; Tilley, T. D.; Zettl, A. *Nano Lett.*, **2004**, *4*, 173.

95 Dibandjo, P.; Chassagneux, F.; Bois, L.; Sigala, C.; Miele, P. *J. Mater. Chem.*, **2005**, *15*, 1917.

96 Alauzun, J. G.; Ungureanu, S.; Brun, N.; Bernard, S.; Miele, P.; Backov, R.; Sanchez, C. *J. Mater. Chem.*, **2011**, *21*, 14025.

97 Vinu, A.; Terrones, M.; Golberg, D.; Hishita, S.; Ariga, K.; Mori, T. *Chem. Mater.*, **2005**, *17*, 5887.

98 Schlienger, S.; Alauzun, J.; Michaux, F.; Vidal, L.; Parmentier, J.; Gervais, C.; Babonneau, F.; Bernard, S.; Miele, P.; Parra, J. B. *Chem. Mater.*, **2012**, *24*, 88.

99 Rushton, B.; Mokaya, R. *J. Mater. Chem.*, **2008**, *18*, 235.

100 Dibandjo, P.; Bois, L.; Chassagneux, F.; Miele, P. *J. Eur. Ceram. Soc.*, **2007**, *27*, 313.

101 Malenfant, P. R. L.; Wan, J.; Taylor, S. T.; Manoharan, M. *Nat. Nanotechnol.*, **2007**, *2*, 43.

102 Li, J.; Xiao, X.; Xu, X.; Lin, J.; Huang, Y.; Xue, Y.; Jin, P.; Zou, J.; Tang, C. *Sci. Rep.*, **2013**, *3*, 3208.

103 Liu, D.; Tang, C. C.; Xue, Y. M.; Li, J. *Prog. Chem.*, **2013**, 25, 1113.

104 Weng, Q.; Wang, X.; Bando, Y.; Golberg, D. *Adv. Energy Mater.*, **2014**, *4*, 1301525.

105 Corso, M.; Auwärter, W.; Muntwiler, M.; Tamai, A.; Greber, T.; Osterwalder, J. *Science*, **2004**, *303*, 217.

106 Bunk, O.; Corso, M.; Martoccia, D.; Herger, R.; Willmott, P.; Patterson, B.; Osterwalder, J.; van der Veen, J. F.; Greber, T.; *Surf. Sci.*; **2007**, *601*, L7.

107 Goriachko, A.; He, Y.; Knapp, M.; Over, H.; Corso, M.; Brugger, T.; Berner, S.; Osterwalder, J.; Greber, T. *Langmuir*, **2007**, *23*, 2928.

108 Martoccia, D.; Brugger, T.; Bjorck, M.; Schleputz, C. M.; Pauli, S. A.; Greber, T.; Patterson, B. D.; Willmott, P. R. *Surf. Sci.*, **2010**, *604*, L16–L19.

109 Berner, S.; Corso, M.; Widmer, R.; Groening, O.; Laskowski, R.; Blaha, P.; Schwarz, K.; Goriachko, A.; Over, H.; Gsell, S.; Schreck, M.; Sachdev, H.; Greber, T.; Osterwalder, J. *Angew. Chem. Int. Ed.*, **2007**, *46*, 5115.

110 Goriachko, A.; He, Y. B.; Over, H. *J. Phys. Chem. C*, **2008**, *112*, 8147.

111 Goriachko, A.; Zakharov, A. A.; Over, H. *J. Phys. Chem. C*, **2008**, *112*, 10423.

112 Wang, L.; Xu, L.; Sun, C.; Qian, Y. *J. Mater. Chem.*, **2009**, *19*, 1989.

113 Wang, M.; Li, M.; Xu, L.; Wang, L.; Ju, Z.; Li, G.; Qian, Y. *Catal. Sci. Technol.*, **2011**, 1, 1159.

114 Sun, C.; Xu, L.; Ma, X.; Qian, Y. *Chin. J Inorg. Chem.*, **2012**, *28*, 601.

115 Meng, X. L.; Lun, N.; Qi, Y. X.; Zhu, H. L.; Han, F. D.; Yin, L. W.; Fan, R. H.; Bai, Y. J.; Bi, J. Q. *J. Solid State Chem.*, **2011**, *184* , 859.

116 Meng, X. L.; Lun, N.; Qi, Y. Q.; Bi, J. Q.; Qi, Y. X.; Zhu, H. L.; Han, F. D.; Bai, Y. J.; Yin, L. W.; Fan, R. H. *Eur. J. Inorg. Chem.*, **2010**, *20*, 3174.

117 Nag, A.; Raidongia, K.; Hembram, K. P. S. S.; Datta, R.; Waghmare, U. V.; Rao, C. N. R. *ACS Nano*, **2010**, *4*, 1539.

118 Golberg, D.; Bando, Y.; Tang, C. C.; Zhi, C. Y. *Adv. Mater.*, **2007**, *19*, 2413.

119 Ma, R. Z.; Bando, Y.; Zhu, H. W.; Sato, T.; Xu, C. L.; Wu, D. H. *J. Am. Chem. Soc.*, **2002**, *124*, 7672.

120 Tang, C. C.; Bando, Y.; Ding, X. X.; Qi, S. R.; Golberg, D. *J. Am. Chem. Soc.*, **2002**, *124*, 14550.

121 Terao, T.; Bando, Y.; Mitome, M.; Kurashima, K.; Zhi, C. Y.; Tang, C. C.; Golberg, D. *Physica E*, **2008**, *40*, 2551.

122 Lim, S.H.; Luo, J.; Ji, W.; Lin. J. *Catal. Today*, **2007**, *120*, 346.

123 Portehault, D.; Giordano, C.; Gervais, C.; Senkovska, I.; Kaskel, S.; Sanchez, C.; Antonietti, M. *Adv. Funct. Mater.*, **2010**, *20*, 1827.

Chapter 2

Hierarchically porous BN microbelts for hydrogen storage

Chapter 2. Hierarchically porous BN microbelts for hydrogen storage

2.1 Introduction

Nanotubes and nanosheets are the two typical low-dimensional nano-morphologies. Both carbon and boron nitride (BN) compounds can be stabilized as such nanostructures. Low-dimensional BN nanomaterials, such as BN nanotubes (BNNTs) and BN nanosheets (BNNSs), are most known for their excellent chemical inertness and thermal stabilities.[1,2] They can be used for achieving excellent reinforcements of mechanical properties and rise in thermal conductivity of many traditional bulk materials, such as polymers, ceramics and metals.[3–5] In the case when maintaining or even enhancing the electrical insulation is needed, low-dimensional BN nanomaterials are the better choice than their carbon ones due to their wide energy band-gaps (~5−6 eV).[6,7] In the field of hydrogen storage, both theoretical and experimental studies have demonstrated that layered BN forms exhibit a higher uptake capacity due to the stronger interactions of H_2 with the heteropolar B-N bonds and partial chemisorption properties.[8–11] For example, BNNTs with different morphologies can irreversibly adsorb 0.9−2.6 wt % of H_2 at 10 MPa at room temperature,[8,12] the figure which is better than the performance of MWCNTs (<1 %) at the same testing conditions.[13] However, ~70 % of the absorbed H_2 was found to retain when the H_2 pressure was removed, indicating a chemisorption-dominated H_2 adsorption at room temperature and a relatively high pressure.

In a low pressure range, the dominating H_2 adsorbing mechanism on carbon and BN surfaces is physisorption, which is believed to be greatly affected by the specific surface area (SSA) and pore width of the adsorbents.[14] For the typical BNNTs with an average diameter of ~50 nm and an estimated inner diameter of ~20 nm, the reported BET SSA was 254 $m^2 g^{-1}$.[8] To obtain the porous BNs with an increased SSA and reduced pore width, the reported strategies have mainly been relied on the hard-template-based routes. For example, when using different porous silica as the templates, the reported SSAs of the obtained porous BNs were of 140−327 $m^2 g^{-1}$.[15–17] Mesoporous BN materials with SSAs ranging from 168 to 565 $m^2 g^{-1}$ consisted of ~ 3 nm pores, as was verified by using activated carbons as the templates.[15,18,19] Further increases of SSAs of the prepared BN materials could be achieved along with this strategy when other templates such as cationic surfactant (820 $m^2 g^{-1}$), zeolite (570 $m^2 g^{-1}$), or block copolymer (950 $m^2 g^{-1}$) were utilized.[20,21,22] However, the SSA and pore width of these template-derived porous BN materials have still been not satisfying for the purpose of practical hydrogen storage. Besides, this method is also prone to other

drawbacks, such as inefficient filling of the mesopores by precursors and harmful post treatment which is required to remove the used templates. Thus, other simple and environmental-friendly non-template methods are of high demand for fabrication of improved porous BN materials for hydrogen storage. Meanwhile, it is also very helpful to clarify the relationship between texture properties and hydrogen uptakes of BN materials, if simpler synthesis methods become available. To the best of my knowledge, the few-layered *h*-BN sheets, that were prepared from boric acid and urea, reportedly exhibited the highest SSA among all non-template derived BNs (927 m^2 g^{-1}).[23]

In this Chapter, I developed an easy method for the preparation of novel BN porous belts with the SSA ranging from 1144 to 1488 m^2 g^{-1}. This synthetic process was accomplished through a one-step reaction of boric acid-melamine (2B·M) precursors in ammonia at different temperatures (900 – 1100 ^oC; Corresponding to BNPB-900, BNPB-1000 and BNPB-1100 sample notations) at ambient pressure without using any templates. Their morphology and elemental compositions were thoroughly characterized using scanning electron microscopy (SEM), energy dispersive X-ray spectroscopy (EDS), high-resolution transmission electron microscopy (HRTEM) and electron energy loss spectroscopy (EELS). N_2 physisorption isotherms recorded at 77 K were used to calculate their pore size distributions and SSAs as based on the Brunauer-Emmett-Teller (BET) equation, while H_2 uptakes were evaluated by H_2 isotherms that were taken at 77 K and 1 MPa. It was demonstrated that these high-surface-area BN porous belts had exhibited high and reversible hydrogen uptakes from 1.6 to 2.3 wt %. Among them, BNPB-1100 was confirmed to have the highest hydrogen uptake capacity. (Note the major results of this chapter has been published in *ACS Nano 2013, 7(2), 1558*; *i.e.* Ref. 24)

2.2 Experimental methods

Synthesis of BN porous belts. 0.03 mol boric acid and 0.015 mol melanine (2B·M) were dissolved in ~ 70 ml 90 ^oC DI water. The solution was then heated and kept at a slightly boiling state to completely evaporate water to obtain the 2B·M adducts. Then, the dried 2B·M precursors were loaded into a horizontal quartz tube and heated in ammonia atmosphere at preset temperatures for 3 h, yielding the mixture of BN micro-rods (bundles that composed of aligned porous belts, Figure 6.1, Chapter 6) and BN porous belts. The received mixtures that contained BN micro-rods were dispersed in isopropyl alcohol and exfoliated under sonication for 30 min to obtain isolated belts and loosen belt bundles. Prolonging the sonication time would further increase the content of the isolated belts.

Structure and composition characterization. The morphology and structure observations were carried out using a Hitachi S-4800 SEM and a JEM-3000F high-resolution transmission electron microscope operated at 300 kV. Chemical compositions were determined by an EMAX energy dispersive X-ray

spectrometer (EDS) and a Gatan 766 electron energy loss spectrometer (EELS) 2D-DigiPEELS. XRD data were collected on a Rigaku Ultima III (Cu Kα) while Raman data were recorded on a Horiba Jobin-Yvon T6400 Raman system with a 514.5 nm excitation laser.

Specific surface areas measurements and H_2 uptake capacity evaluations. The nitrogen physisorption isotherms were measured at 77 K on a Quantachrome Autosorb-1 system after outgassing the samples at 150 °C for 24 h. Specific surface areas were computed using the Brunauer-Emmett-Teller (BET) equation for the relative pressure range from 0.02−0.12. The pore size distribution, combining with respective pore volume and average pore size, were calculated based on the NLDFT theory. The hydrogen absorption isotherms were recorded on a BELSORP-HP-30 hydrogen adsorption system (BEL Japan, Inc.) at 77 K and 0−1 MPa. Before the measurements, all samples were outgassed at 150 °C for 24 h.

2.3 Structural and compositional characterizations

The BNPB-1100 shows a belt-like structure, a typical BN morphology that is derived from 2B·M precursors at high temperature. The SEM images verify that the width and thickness of these belts are commonly located at the range of 0.3−1.0 and 0.2−0.5 μm, respectively, with the length varying from ~10 μm to hundreds of micrometers, see Figure 2.1 (a). Ultra-short and ultra-long belts also appear occasionally. Unlike smooth appearances of CNTs and BNNTs, many sheet-like protrusions and structural breakages were observed on these belt surfaces (Figure 2.1(b)). A fine structure analysis by means of SEM and TEM further indicates that there are many pores randomly distributed on the walls of BN porous belts, leading to a featured appearance similar to perforated tubes, see Figure 2.1 (c,d). Besides, dense tunnel openings which lead to the creation of belt inner portions are also found stacked at the terminal and breakage regions, indicating a high porosity of these BN belts. HRTEM characterizations (Figure 2.1 (f)) on many belt wall boundaries show that the average spacing between the adjacent fringes is 0.38 nm, obviously larger than the (0002) interplanar distance in bulk *h*-BN and BNNTs (0.33 − 0.34 nm).[25] Such an enlarged spacing was further confirmed by the X-ray diffraction (XRD) patterns; the deduced d_{0002} spacing was 0.376 nm, based on the corresponding (0002) peak, as shown in Figure 2.2 (a). The simultaneously obtained *in-plane* lattice spacing is 0.211 nm, in accordance with the HRTEM observations (~0.22 nm, Figure 2.1 (f,g)). It is noteworthy that the ordering observed for this novel BN material is between classical *h*-BN and amorphous BN (*a*-BN), it is closer to that reported for turbostratic BN materials (*t*-BN, d_{0002} = 0.356 nm).[26–28] Other BN porous belt samples that were obtained at different temperatures also show the similar structural features (Figure 6.3, Chapter 6). It is noted that the peculiar dislocation structures are evident in the present BN phases. Three common dislocation structures, radical-rich edge dislocations (1), helical screw dislocations (2) and Y-form dislocations (3), are illustrated in Figure 2.1 (f). Such dislocation types are similar to those observed in anthracites.[29]

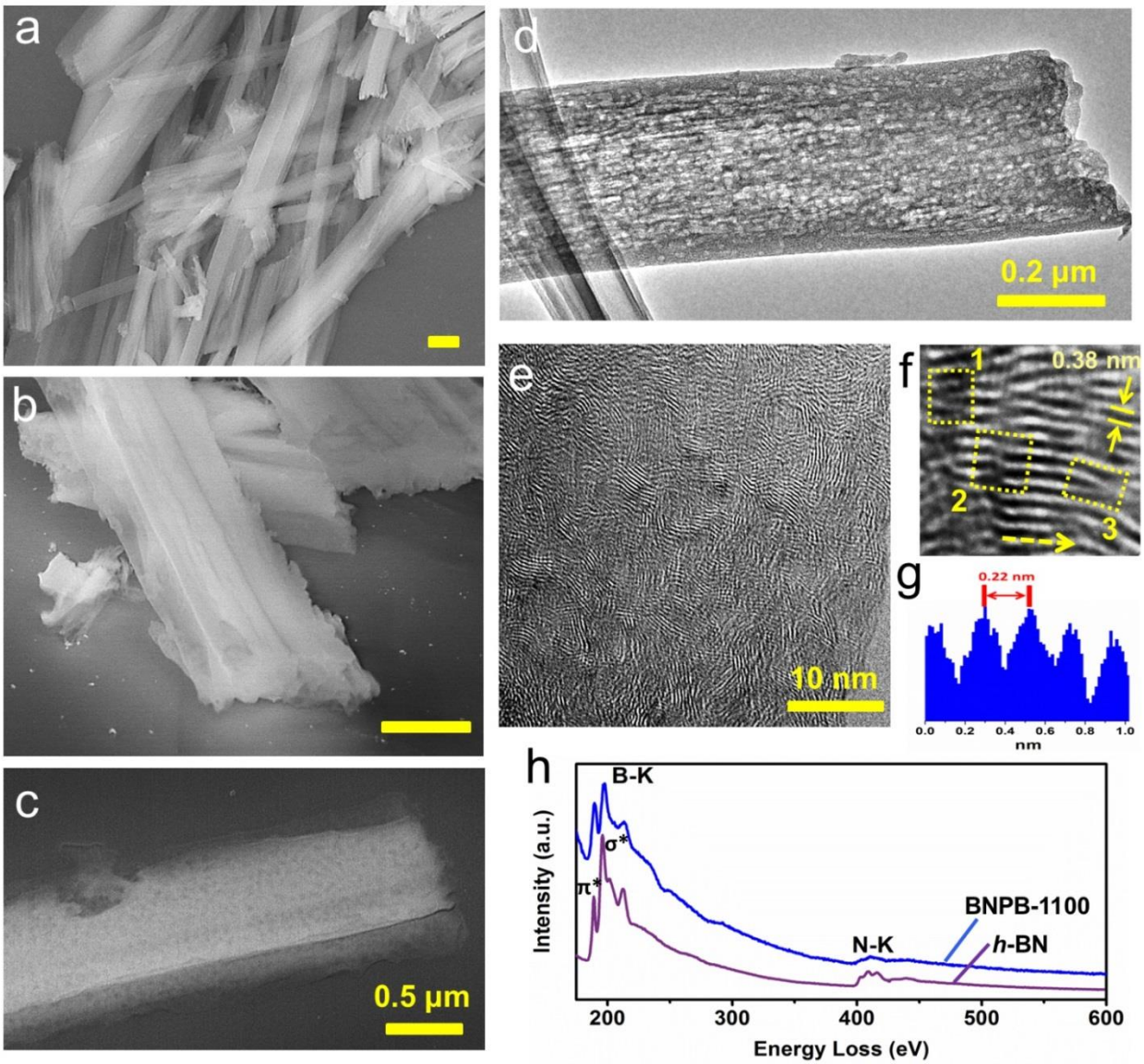

Figure 2.1 (a) Low magnification SEM image of BN porous belts fabricated at 1100 ^{o}C (BNPB-1100). (b,c) Inclined and top views of isolated porous belts, highlighting a belt-shaped morphology. (d) TEM image of a section of belt at a low magnification. (e,f) HRTEM images taken at the edge of belt walls. Three common dislocation structures are marked by yellow dashed frames in (f). (g) TEM contrast intensity profile recorded along the yellow dashed arrow, as labeled in (f). (h) EEL spectrum taken from a representative BN porous belt. Scale bars in (a) and (b) are both 1 μm. Reprinted from Ref. 23.

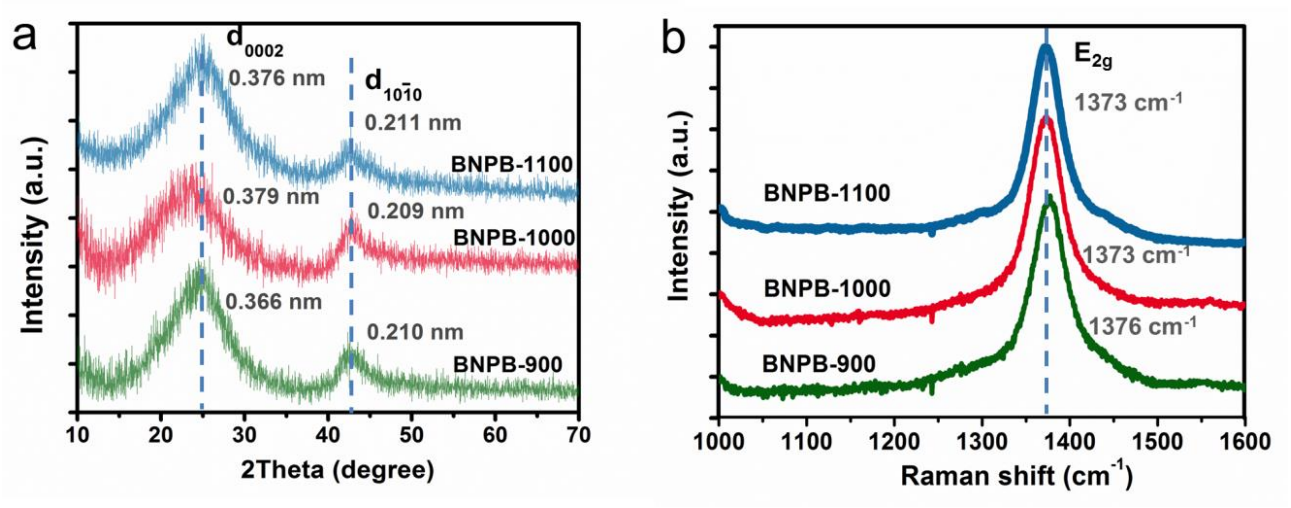

Figure 2.2 XRD patterns (a) and Raman spectra (b) of BN porous belts obtained at different temperatures (BNPB-900, BNPB-1000 and BNPB-1100 samples). Reprinted from Ref. 23.

Both amorphous and crystalline phases, as revealed in Figure 2.1 (e), coexist in the present BN porous belts. The most characteristic change caused by this partial disorder of BN phase in XRD patterns is broaden and less intense peak of the (0002) reflection at 2θ = 23.69°, as well as the 2θ = 42.89° for BNPB-1100 that corresponds to the (10-10) reflection. With the increase of synthesis temperatures, the corresponding (0002) patterns are not monotonously shifting. BNPB-1000 exhibits the smallest (0002) diffraction peak at 2θ = 23.22°, with the derived d_{0002} = 0.379 nm. The higher synthesis temperature (1100 °C) causes the shrinkage of interplanar spacing of BN phase, as shown in Figure 2a.

Raman spectroscopy is an effective tool that can probe BN phases. Both Raman shift and FWHM of E_{2g} vibration can be used to elucidate the crystallinity and ordering of hexagonal and other layered BN structures. It is known that *h*-BN single crystals with a high quality show an intrinsic E_{2g} vibration peak at 1367 cm^{-1} with the FWHM of 9.1 cm^{-1}.[29] For polycrystalline BN, its E_{2g} mode is clearly shifting to a higher frequency from 1367 to 1374 cm^{-1} as the crystal domain size decreases, with the FWHM increasing from 11 to 42 cm^{-1}, respectively.[30] Meanwhile, Raman shift and FWHM are also sensitive to the layer numbers of *h*-BN. With the decrease of layer number to *c.a.* 2 layers, E_{2g} mode was observed to shift to a higher frequency (1373.4 cm^{-1}) with a slight increase of FWHM to 11.7 cm^{-1}.[31] Figure 2.2 (b) shows sharp E_{2g} peaks at 1376, 1373 and 1373 cm^{-1} for the as-prepared BN porous belts obtained at 900, 1000 and 1100 °C with FWHMs of ~ 56, 43 and 38 cm^{-1}, respectively. An upshift of E_{2g} vibration mode to the higher frequency as compared to bulk *h*-BN manifests weaker interactions of interlayers in BN porous belts, while the obvious broadening of the E_{2g} peak shows a clear size reduction of the ordered BN phase.

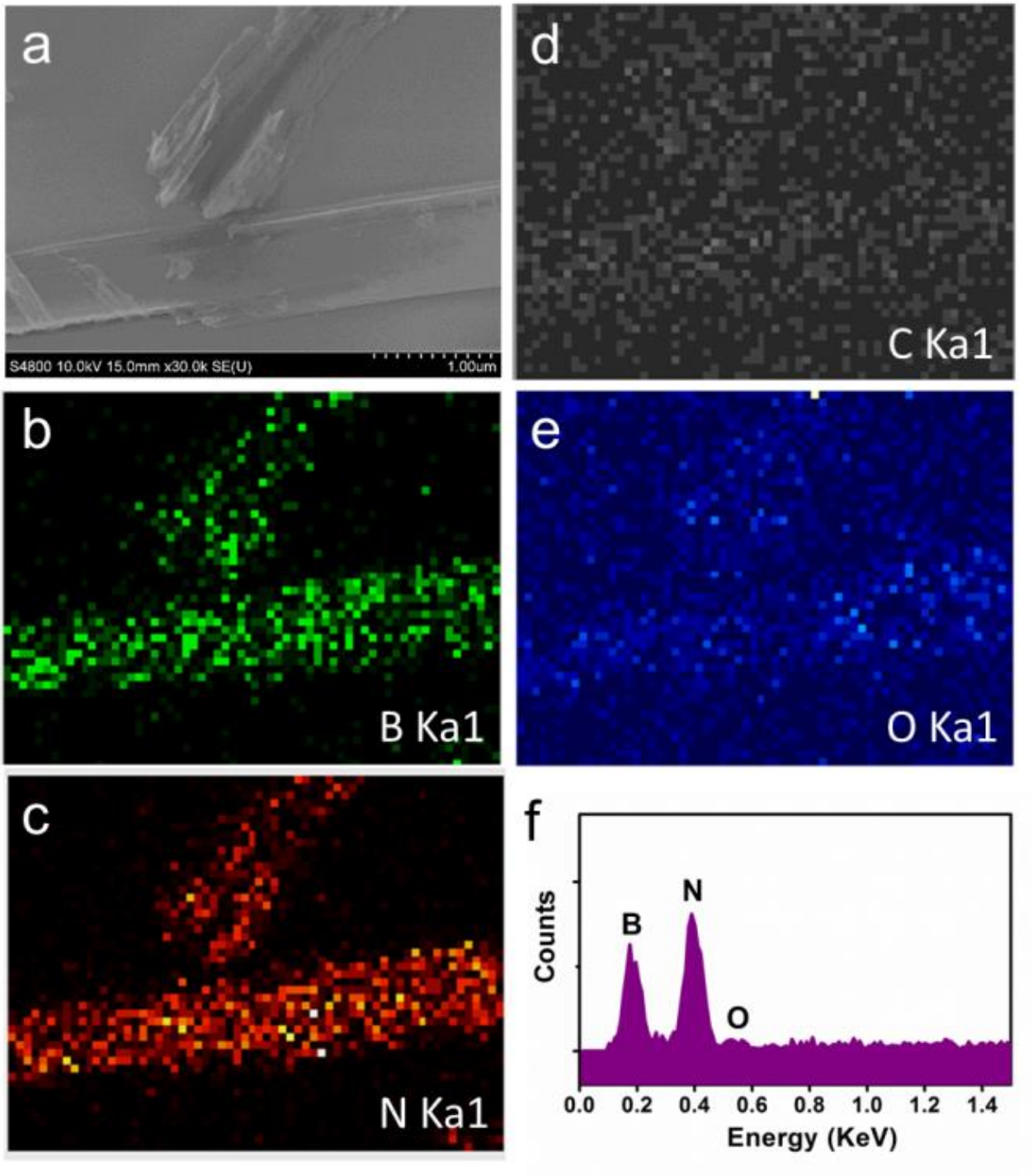

Figure 2.3 SEM image **(**a) and corresponding boron, nitrogen, carbon and oxygen maps (b-g) of BNPB-1100. (g) Corresponding Energy Dispersive X-ray spectrum (EDX), confirming pure BN composition. Reprinted from Ref. 23.

The chemical composition of BN porous belts was verified by EELS and EDX. The EEL spectrum of BNPB-1100 reveals distinct boron and nitrogen core loss K-edges at 188 eV and 401 eV respectively, as shown in Figure 2.1 (h). A trace of carbon K-edge at 284 eV was detected. The π* and σ*-peak shapes on the

left and right-hand sides of the boron K-edge imply that the as-prepared BN porous belts indeed belong to an intermediate state between *a*-BN and *h*-BN,[28] in accordance with HRTEM-, XRD- and Raman-based conclusions. To further confirm the chemical composition of the obtained BN porous belts and to obtain sufficient information regarding the elemental distributions, we also carried out EDS analysis and constructed elemental distribution maps. Figure 2.3 (a) is a typical image of the BNPB-1100 sample. Figure 2.3 (b,c) shows corresponding boron and nitrogen maps, indicating clear presences of boron and nitrogen species. Figure 2.3 (d) is a carbon map, in which minor signals are randomly distributed over the whole investigated area. The fuzzy oxygen signals (Figure 2.3 (e)) verify of the neglectful oxygen content in the present product. The accumulated EDS spectrum acquired from an area over 0.01 mm^2 of the samples is shown in Figure 2.3 (f); this further suggests that the major compositions of BN porous belts are indeed boron and nitrogen elements with a minor percentage of oxygen. A semi-quantitative analysis based on EDS result shows that the (B + N) at % content is no lower than 97 %. BNPB-1000 and BNPB-900 EDS spectra are shown in Figure 6.5, Chapter 6, also confirming the pure BN composition. It is noted that the oxygen content in the obtained BN samples becomes larger if the synthesis temperatures lower than 900 ^oC were chosen. *E. g.* the oxygen content can reach ~6 at % for a porous belt sample prepared at 700 ^oC.

2.4 Thermal stability studies

To exam the thermal stability of the obtained BNPS products, high-temperature annealing treatment was carried out. Under 1500 ^oC treatment for 5 h, the material belt-like morphology and phase ordering were generally maintained, as shown in Figure 2.4. In Figure 2.5, the resultant d_{0002} decreases from 0.376 nm to 0.364 nm after annealing, while the resultant E_{2g} vibration mode in the Raman spectrum shifts to 1370 cm^{-1} without obvious change of the FWHM value. A statistics based on HRTEM analysis also confirmed the general shrinkage of the (0002) distance. The documented dislocation structures that exist in the present BN porous microbelts provide a decent explanation for the high thermal stability. These not only widen the average BN (0002) layer distances, but also "screw" adjacent layers together, and therefore provide considerable strength to prevent further ordering of BN (0002) layers at a high temperature, *e.g.* 1500 ^oC (like in the case of appearing strength which suppresses the solubility of anthracite [29]).

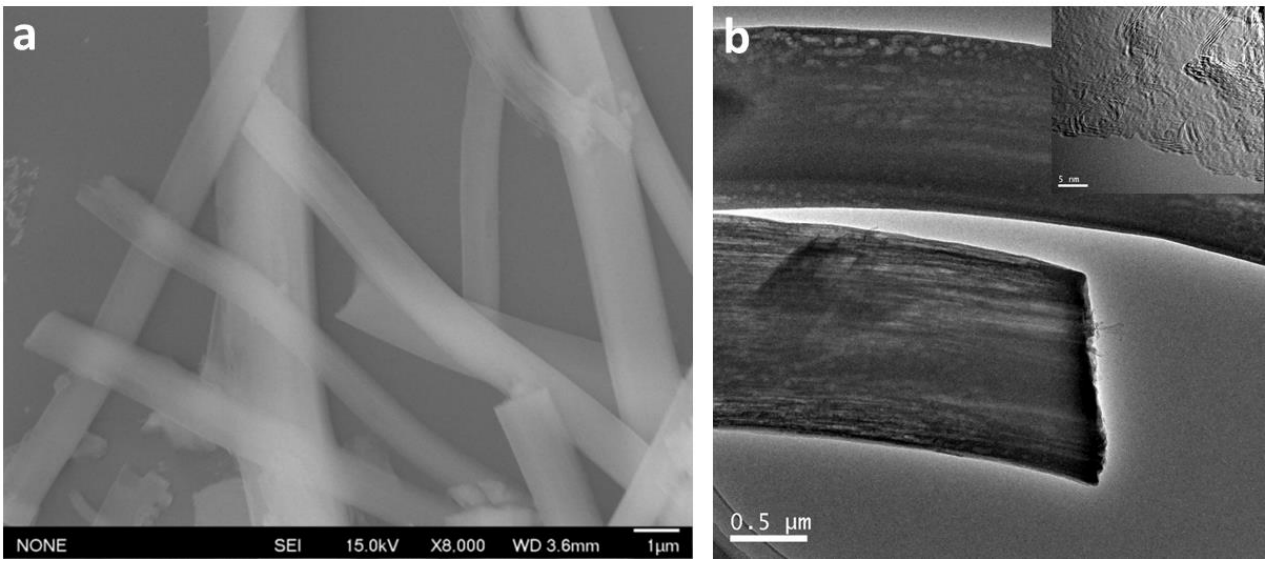

Figure 2.4 SEM (a) and TEM (b) images of BNPB-1100 sample after annealing at 1500 ^{o}C in argon for 5 h. The inset in (b) is the HRTEM image of the belt edge. Reprinted from Ref. 23.

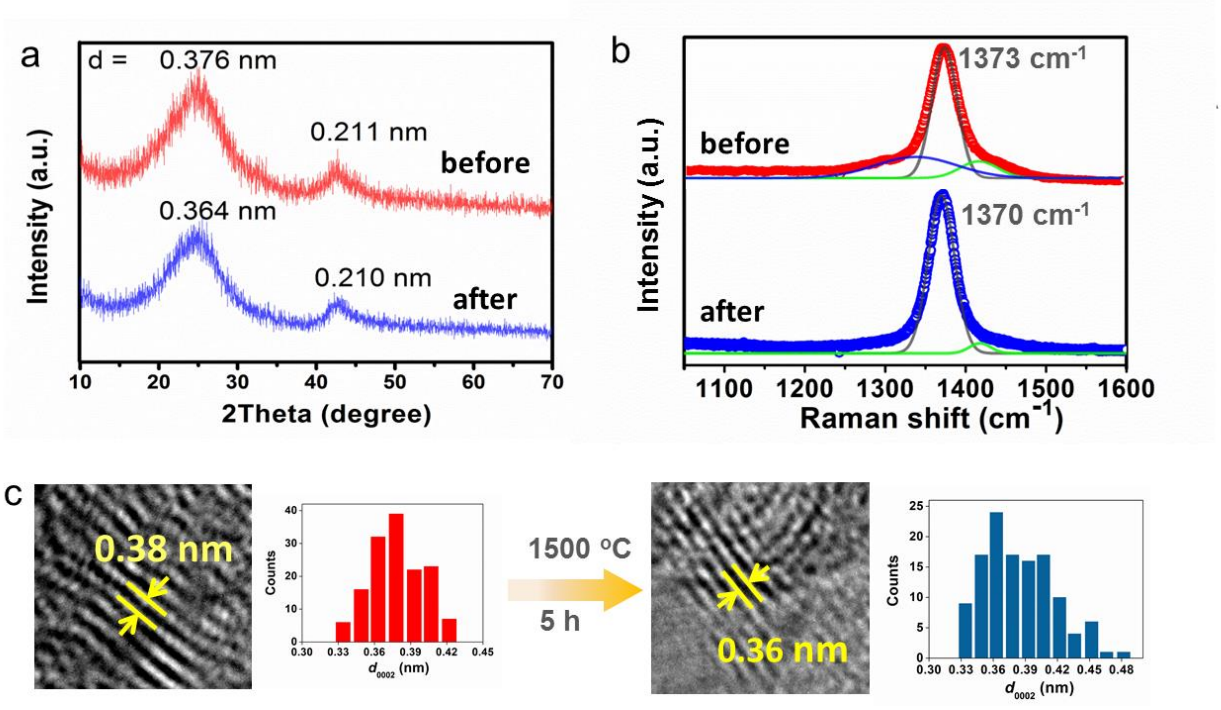

Figure 2.5 XRD patterns (a) and Raman spectra (b) of a BNPB-1100 sample before and after annealing. Top: as-prepared; bottom: after annealing at 1500 ^{o}C in argon for 5 h. The corresponding Gaussian simulations of E_{2g} peaks are also shown in (b). (c) HRTEM images of as-prepared (left) and annealed (right) BN porous microbelts showing a decreased distance between adjacent (0002) fringes after annealing. Reprinted from Ref. 23.

2.5 Material porosity characterization

In order to measure the BET SSA of BN porous belts, I have recorded its N_2 adsorption and desorption isotherms at 77 K. In case of mesoporous and macroporous materials, the standard BET analysis is carried out at the pressure range of $0.05 < P/P_0 < 0.35$.[32] In general, having no micropores, or any other type of strongly adsorbing sites, this range is well fitted to a linear plot. However, for microporous materials, this selection criterion is no longer right because all pores must be completely filled with N_2 molecules at pressures below this standard BET range. So, the respective pressure range acquired for the multi-point BET analysis of the regarded microporous BN samples was selected from 0.02 to 0.12 based on the criteria proposed elsewhere.[33] The selection of pressure range for BET analysis is judged as follows: (1) In a selected pressure range, $v(P_0 - P)$ should monotonically increase with P/P_0, as shown in Figure 2.6 (a − c). (2) For the obtained linear equation, the Y-axis intercept should be positive to yield a meaningful value of the C parameter. Based on these two criteria, P/P_0 range chosen for the analysis was 0.02 – 0.12.

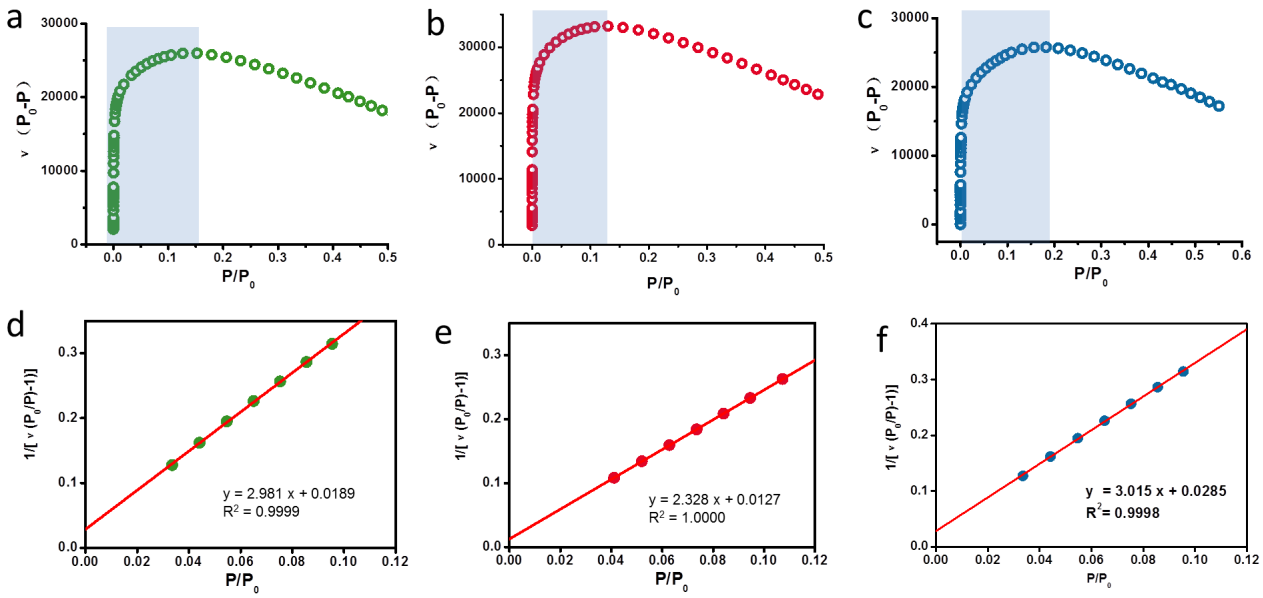

Figure 2.6 (a − c) $v(P_0 - P)$ *vs* P/P_0 plots for BNPB-900, BNPB-1000 and BNPB-1100 samples. The colored rectangles show the pressure ranges which satisfy the first criterion. (d − f) Seven-point BET plots in the selected pressure ranges for N_2 on BN porous belt samples. Reprinted from Ref. 23.

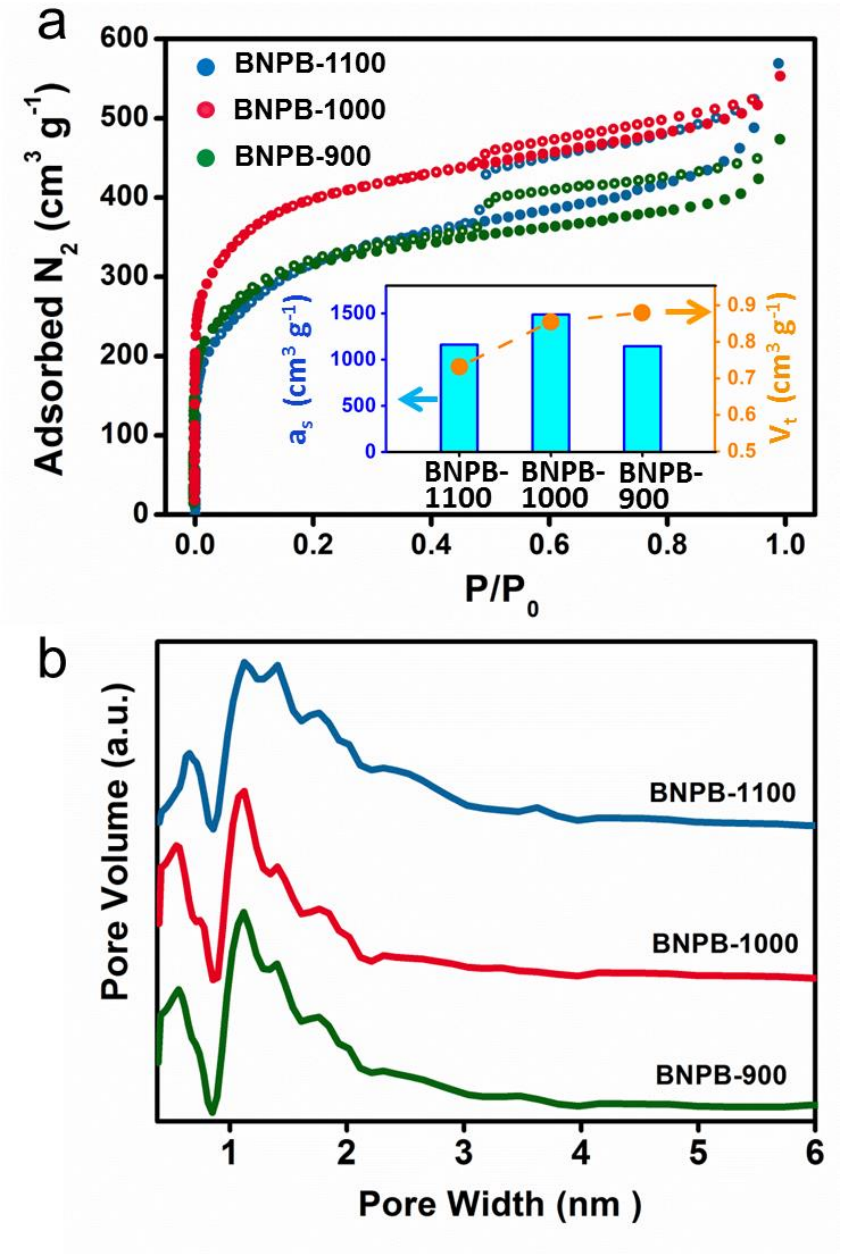

Figure 2.7 (a) Nitrogen adsorption-desorption isotherms of BN porous belts fabricated at various temperatures (BNPB-900, BNPB-1000 and BNPB-1100). The insets in (a) are the histogram of BET surface areas ($\mathbf{a_s}$) and total pore volumes ($\mathbf{V_t}$) for the as-made samples. (b) Pore size distributions of BN porous belts derived from non-local Density Functional Theory (DFT). Reprinted from Ref. 23.

The isotherm hysteresis loops of the BN porous belt samples that were made at various temperatures belong to the typical *H4* type, as based on the IUPAC classification, indicating microporosity and the presence of slit-shaped mesopores due to capillary condensation. Non-local density functional theory (NLDFT) was implemented to calculate the micropore width and pore size distribution of the obtained BN porous belts. As followed from both Figure 2.7 and Table 2.1, all BN porous belt samples prepared at

different temperatures display high BET SSAs of 1161, 1488 and 1144 m^2 g^{-1} for BNPB-900, BNPB-1000 and BNPB-1100, respectively, thus these figures are among the largest SSAs for all reported BN materials at that time. Besides, they also show high microporosity (0.350 – 0.502 cm^3 g^{-1}) as well as meso- and macroporosities (0.348 – 0.530 cm^3 g^{-1}) with an average micropore width of 1.1 nm. The total pore volume determined at P/P_0 = 0.99 reaches 0.880 cm^3 g^{-1} for BNPB-1100. Although the total pore volumes of the obtained BN porous samples increase with the rise of the synthesis temperature, BNPB-1000 exhibits the largest volume of micropores of 0.502 cm^3 g^{-1}.

2.6 Porosity formation mechanisms

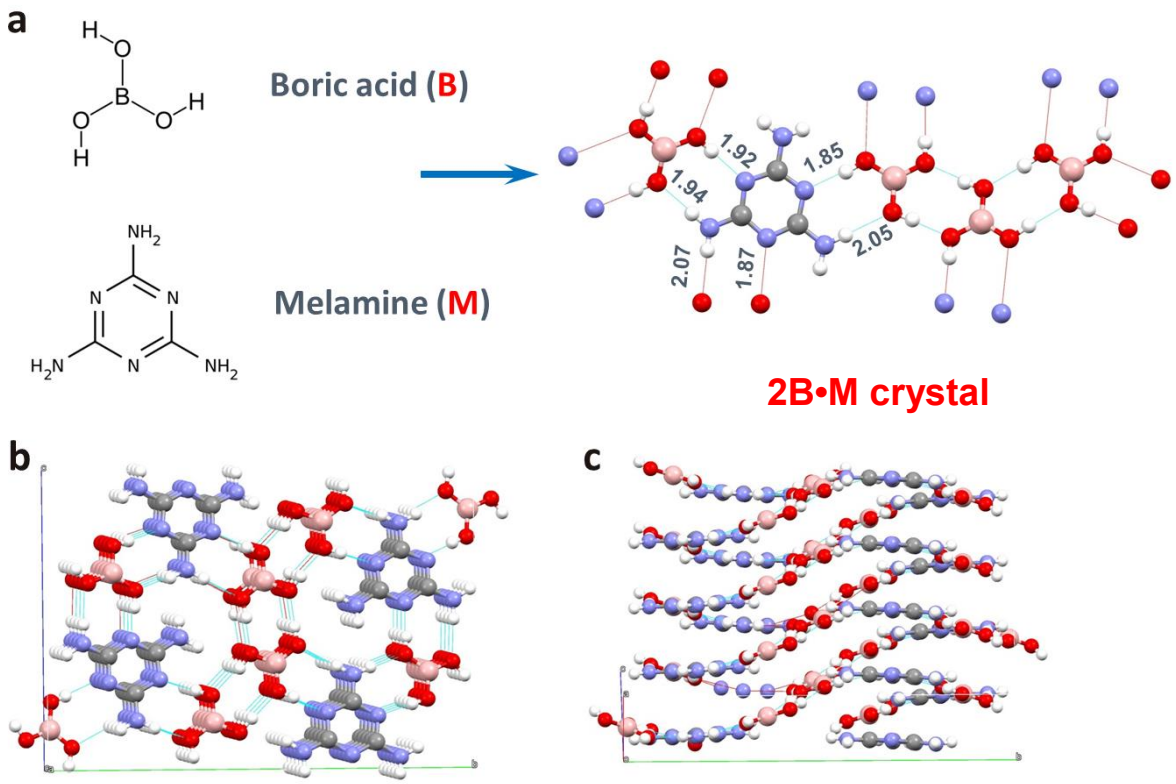

Figure 2.8 (a) Illustration of the formation of boric acid-melamine adduct (2B•M) with the ratio of 2:1. The length of H-bonds is labeled in Å. Top view (b) and side view (c) of the 2B•M crystal structure. Reprinted from Ref. 33.

Boric acid and melamine molecules can interact with each other to form insoluble adducts by H-bonding. The structure of boric acid-melamine adduct with the ratio of 2:1 is shown in Figure 2.8. Every boric acid (melamine) molecule in the crystal interacts with 3 adjacent melamine (boric acid) molecules through H-bonds. XRD characterization of 2B•M powders (Figure 2.9) also confirm the formation of a new phase, which is constructed by boric acid and melamine molecules at the molecular level. With the increase of

temperature to ~120 °C, the polymerization reactions between boric acid and melamine start with a loss of water (Figure 2.10). It is noticed that melamine without formation of the adduct sublimates at 200-300 °C. Strong covalent forces formed between B and N-precursors instead of the original weak H-bonds, while new 3D networks composed of a BCNO backbone and void space are formed instead of the initial compact structure. With a further loss of weight (C, O and partially N) induced by temperature rising or NH_3 etching, the BCNO backbone undergoes structural reconstructions to form a BN network. Meanwhile, more void space (pores) is formed. It is noted that the unwanted carbonaceous species could be removed from BN *via* a reaction with ammonia at 1000 °C following eq 1.[21]

$$C + NH_3 \rightarrow CH_4 + N_2 \quad (1)$$

Experientially, an excess of ammonia would favors the entire conversion of B_2O_3 to BN, and offset the loss of ammonia because of melamine decomposition.

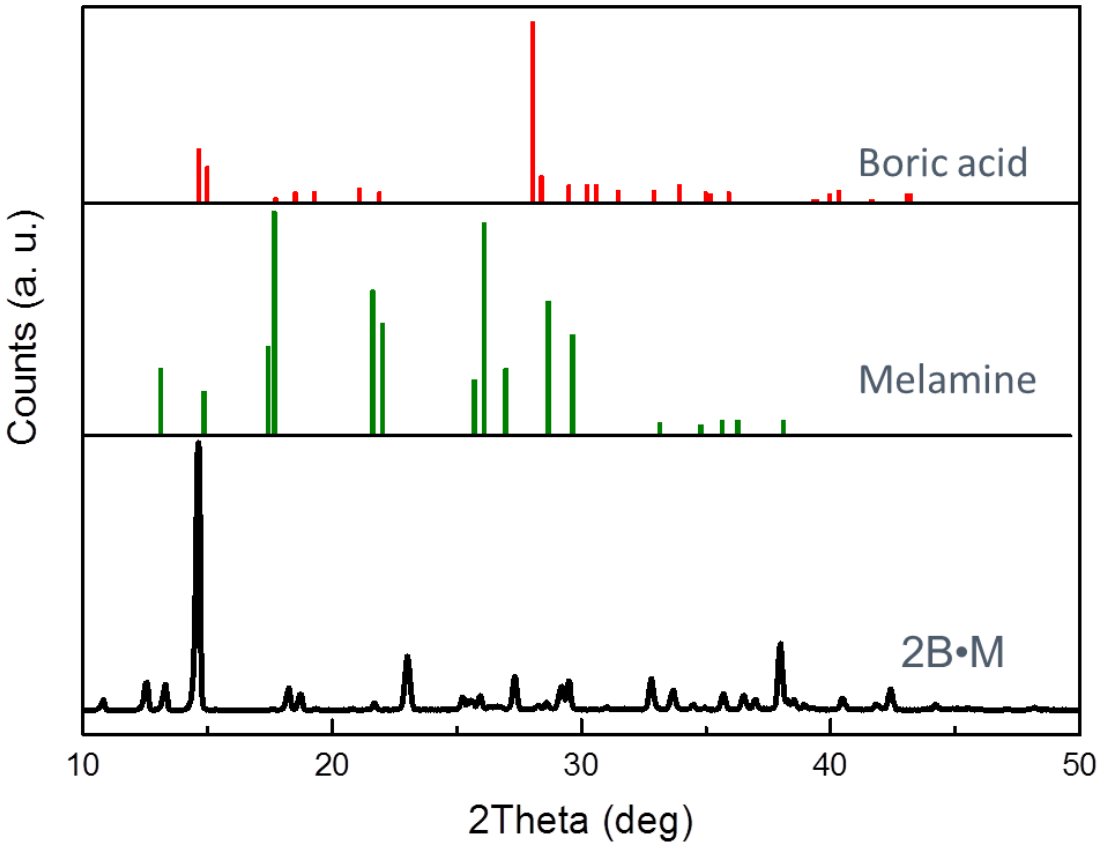

Figure 2.9 X-ray diffraction patterns of 2B•M precursors compared with those of standard boric acid (JCPDS 300199) and melamine (JCPDS 241654).

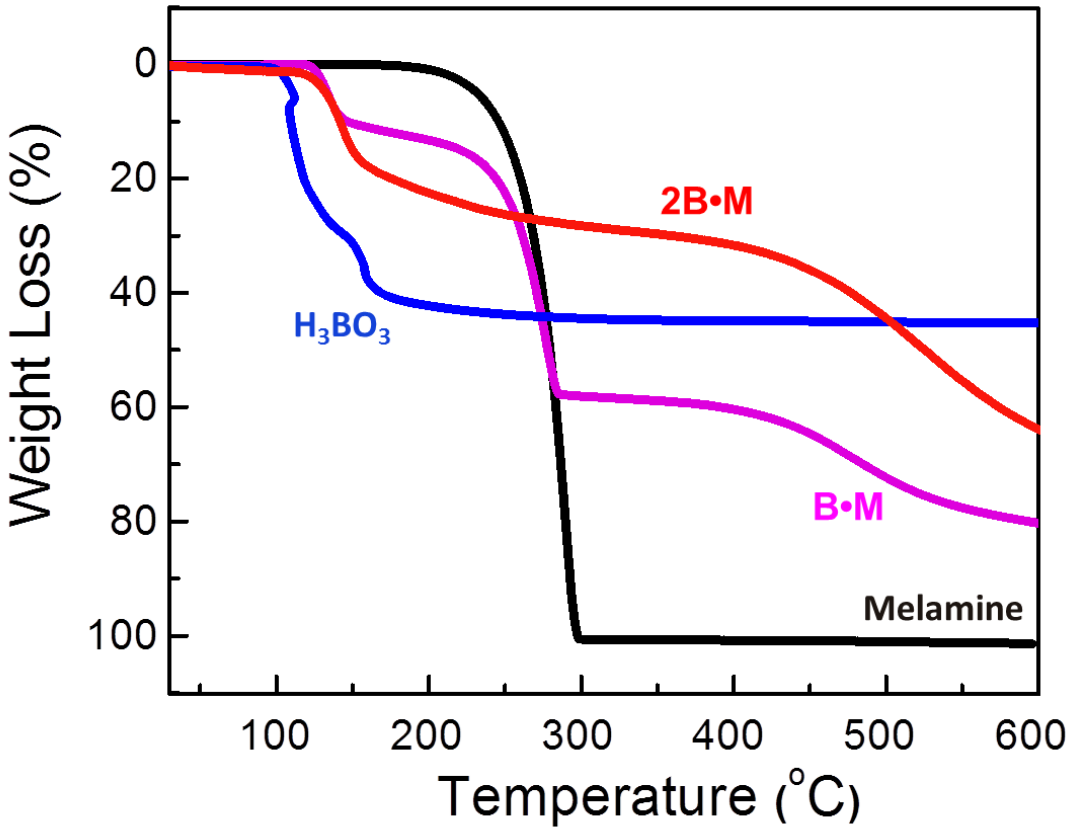

Figure 2.10 TG analysis of 2B•M and B•M precursors.

Regarding organic ammonia borane or borazine precursors, an advantage of using 2B·M precursors is their much easier access, a lower cost and toxicity. However, besides providing a N source, melamine also contains carbon atoms. One challenge to utilize this 2B·M precursor for the synthesis of BN materials is how to get rid of carbon atoms in a final product.[35] Before my report, numerous BN nanomaterials, including BNNTs, nanofibers, nanocable coatings, *etc.* were prepared based on this 2B·M precursor.[36–38] In order to eliminate carbon content, an extra-high temperature was usually implemented to obtain pure BN composition, *e.g.*, induction heating at 1700−2000 °C.[36,39] At such high temperature, it was difficult to maintain the original BN morphology; it insurmountably recrystallized to a standard BN phase; *i.e.*, any porous structures would be broken during this process. Actually, the role of the 2B·M precursor involved in these extra-high temperature reactions is to serve as a boron source. Thus, our results also provide a facile method to fabricate high purity BN materials under the reaction of 2B·M precursors with ammonia (P = 1 atm, T $\geqslant$ 900 °C). At such mild conditions, the formed porous structures would unlikely collapse to form the crystalline *h*-BNs. Their yield is as high as 20 wt % compared to the raw 2B·M and the massive production may be envisaged. The morphology of the products is fully controllable because the appearance of corresponding precursors can be diversified utilizing various conditions of crystallization.

2.7 Hydrogen adsorption results

The H_2 adsorption isotherms of BN porous belts, recorded at liquid nitrogen temperature (77 K) and 1 MPa by the volumetric method, are shown in Figure 2.11. With an increase of the preparation temperatures from 900 to 1100 °C, the obtained BN porous belt samples exhibit enhanced H_2 uptakes from 1.6 to 2.3 wt %, that not strictly follow their texture property changes, such as SSA or micropore volume. BNPB-1100 shows the highest H_2 uptake of 2.3 wt %. For comparison, the H_2 uptake of bulk *h*-BN measured at the same conditions reveals that its uptake capacity is negligible, far less than 0.1 wt %. However, a further increase of the synthesis temperature can't improve the H_2 uptake of the obtained BN products. Although all sorption isotherms are entirely reversible, the larger steady slope of BNPB-1100 implies that the better uptakes can be expected at higher H_2 pressure than for other samples. This peculiar H_2 adsorption behaviour may be caused by the intrinsic heterogeneous adsorption properties of H_2 on different sample surfaces, which may contain different densities of "active" H_2 adsorbing sites featuring the higher H_2 affinity.

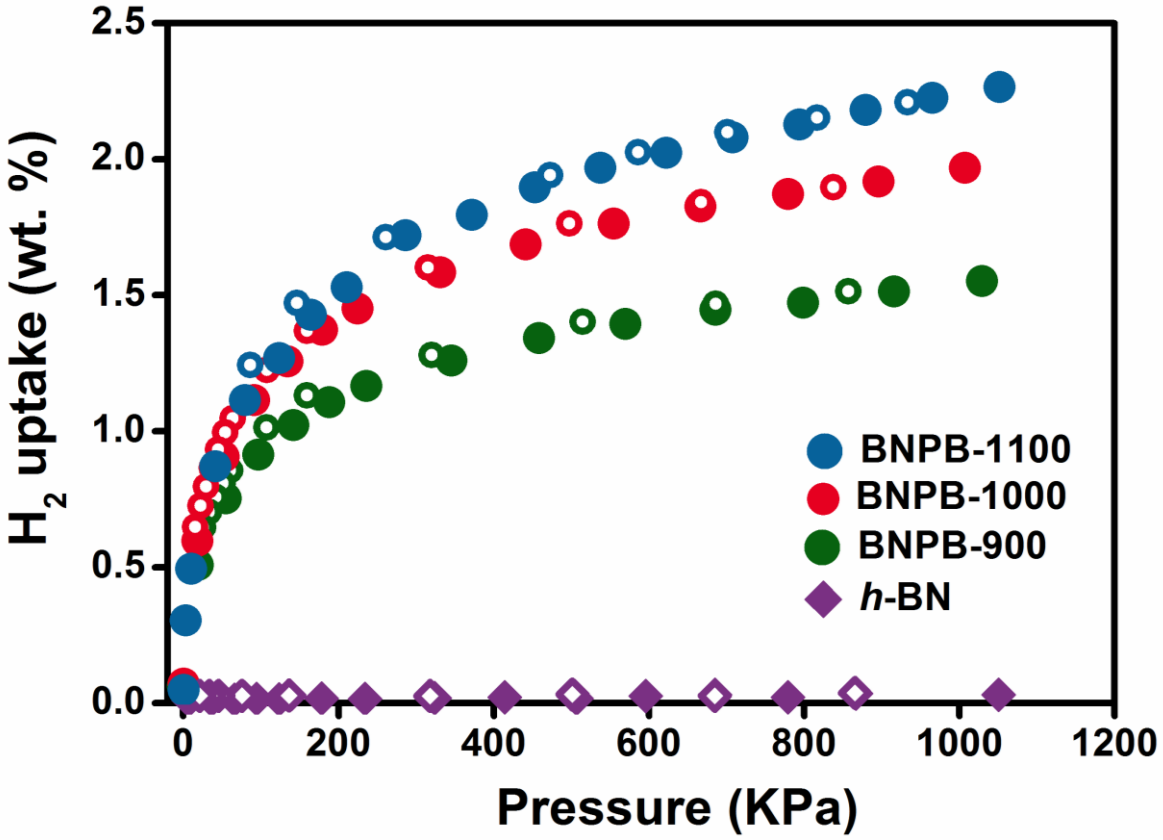

Figure 2.11 Hydrogen adsorption-desorption isotherms of BN porous belts at 77 K and 1 MPa. The hydrogen uptake of bulk *h*-BN is provided for comparison. Reprinted from Ref. 23.

Table 2.1 Textural characteristics and hydrogen uptakes of the products

Samples	BET SSA (m^2 g^{-1})	Langmuir SSA (m^2 g^{-1})	Total pore volume (cm^3 g^{-1})[a]	Micropore volume (cm^3 g^{-1})[b]	Meso + macro pore volume (cm^3 g^{-1})[c]	Micropore width (nm)[a]	H_2 uptake (wt %)[d]
BNPB-900	1161	1163	0.732	0.384	0.348	1.1	1.6
BNPB-1000	1488	1513	0.855	0.502	0.353	1.1	2.0
BNPB-1100	1144	1122	0.880	0.350	0.530	1.1	2.3

[a]The total pore volume is calculated at a relative pressure of 0.99. [b]The micropore volume and width are calculated by NLDFT method applied to nitrogen adsorption isotherm. [c]Meso- and macropore volumes are evaluated by subtracting the micropore volume from the total pore volume. [d]Hydrogen uptake capacities are measured volumetrically at 77 K and 1 MPa. Reproduced from Ref. 23.

2.8 Summary

To sum up, the current study invents a simple way to fabricate highly porous BN materials (*i.e.* BN porous belts) *via* a one-step reaction between boron acid-melamine precursor and ammonia under moderate conditions. The obtained BN phase in porous belts is partially disordered and shows an enlarged average spacing between the neighbouring (0002) layers, featuring it as an intermediate state between *h*-BN and *a*-BN. The as-prepared BN porous belts exhibit a high thermal stability under annealing treatment at 1500 ^oC, indicating the presence of peculiar dislocation structures which stabilize the porous morphology, as was thoroughly confirmed by HRTEM results. The BN porous belt samples made at 1000 ^oC show the largest SSA and micropore volume, hitting 1488 m^2 g^{-1} and 0.502 cm^3 g^{-1}, respectively. The 1100 ^oC-derived BN porous belt samples exhibit the largest total pore volume of 0.880 cm^3 g^{-1}, and their H_2 uptake evaluations at 77 K and 1 MPa reveal that such samples possess the highest reversible H_2 uptake capacity of 2.3 wt %.

2.9 References

1 Golberg, D.; Bando, Y.; Kurashima, K.; Sato, T. *Scr. Mater.* **2001**, *44*, 1561–1564.

2 Chen, Y.; Zou, J.; Campbell, S. J.; Caer, G. L. *Appl. Phys. Lett.* **2004**, *84*, 2430–2432.

3 Huang, Q.; Bando, Y.; Xu, X.; Nishimura, T.; Zhi, C. Y.; Tang, C. C.; Xu, F. F.; Gao, L.; Golberg, D. *Nanotechnology* **2007**, *18*, 485706.

4 Zhi, C. Y.; Bando, Y.; Tang, C. C.; Kuwahara, H.; Golberg, D. *Adv. Mater.* **2009**, *21*, 2889– 2893.

5 Wang, X. B; Zhi, C. Y; Li, L.; Zeng, H. B.; Li, C.; Mitome, M.; Golberg, D.; Bando, Y. *Adv. Mater.* **2011**, *23*, 4072–4076.

6 Zhi, C. Y.; Bando, Y.; Terao, T. S.; Tang, C. C.; Golberg, D. *Pure Appl. Chem.* **2010**, *82*, 2175–2183.

7 Tijerina, J. T.; Narayanan, T. N.; Gao, G.; Rohde, M.; Tsentalovich, D.; Pasquali, M.; Ajayan, P. M. *ACS Nano* **2012**, *6*, 1214–1220.

8 Ma, R. Z.; Bando, Y.; Zhu, H. W.; Sato, T.; Xu, C. L.; Wu, D. H. *J. Am. Chem. Soc.* **2002**, *124*, 7672–7673.

9 Wang, P.; Orimo, S.; Matsushima, T.; Fujii, H.; Majer, G. *Appl. Phys. Lett.* **2002**, *80*, 318–320.

10 Jhi, S. H.; Kwon, Y. K. *Phys. Rev.* B **2004**, *69*, 245407.

11 Lim, S. H.; Luo, J. Z.; Ji, W.; Lin, J. *Catal. Today* **2007**, *120*, 346–350.

12 Tang, C. C.; Bando, Y.; Ding, X. X.; Qi, S. R.; Golberg, D. *J. Am. Chem. Soc.* **2002**, *124*, 14550–14551.

13 van den Berg, A. W. C.; Otero Arean, C. *Chem. Commun.* **2008**, 668–681.

14 Yang, S. J.; Kim, T.; Im, J. H.; Kim, Y. S.; Lee, K.; Park, C. R. *Chem. Mater.* **2012**, *24*, 464–470.

15 Dibandjo, P.; Chassagneux, F.; Bois, L.; Sigala, C.; Miele, P. *J. Mater. Chem.* **2005**, *15*, 1917−1923.

16 Rushton, B.; Mokaya, R. *J. Mater. Chem.* **2008**, *18*, 235−241.

17 Alauzun, J. G.; Ungureanu, S.; Brun, N.; Bernard, S.; Miele, P.; Backov, R.; Sanchez, C. *J. Mater. Chem.* **2011**, *21*, 14025−14030.

18 Han, W. Q.; Brutchey, R.; Tilley, T. D.; Zettl, A. *Nano Lett.* **2004**, *4*, 173−176.

19 Vinu, A.; Terrones, M.; Golberg, D.; Hishita, S.; Ariga, K.; Mori, T. *Chem. Mater.* **2005**, *17*, 5887–5890.

20 Dibandjo, P.; Bois, L.; Chassagneux, F.; Miele, P. *J. Eur. Ceram. Soc.* **2007**, *27*, 313–317.

21 Schlienger, S.; Alauzun, J.; Michaux, F.; Vidal, L.; Parmentier, J.; Gervais, C.; Babonneau, F.; Bernard, S.; Miele, P.; Parra, J. B. *Chem. Mater.* **2012**, *24*, 88–96.

22 Malenfant, P. R. L.; Wan, J.; Taylor, S. T.; Manoharan, M. *Nat. Nanotechnol.*, **2007**, *2*, 43.

23 Nag, A.; Raidongia, K.; Hembram, K. P. S. S.; Datta, R.; Waghmare, U. V.; Rao, C. N. R. *ACS Nano* **2010**, *4*, 1539–1544.

24 Weng, Q. H.; Wang, X. B.; Zhi, C. Y.; Bando, Y.; Golberg, D. *ACS Nano*, **2013**, *7*, 1558.

25 Golberg, D.; Bando, Y.; Huang, Y.; Terao, T.; Mitome, M.; Tang, C. C.; Zhi, C. Y. *ACS Nano* **2010**, *4*, 2979–2993.

26 Thomas, J.; Weston, N. W.; O'Connor, T. E. *J. Am. Chem. Soc.* **1963**, *84*, 4619–4622.

27 Hamilton, E. J. M.; Dolan, S. E.; Mann, C. M.; Colijn, H. O.; Shore, S. G. *Chem. Mater.* **1995**, *7*, 111–117.

28 Zhao, Z. Y.; Yang, Z. G.; Wen, Y.; Wang, Y. H. *J. Am. Ceram. Soc.* **2011**, *94*, 4496–4501.

29 Kubota, Y.; Watanabe, K.; Tsuda, O.; Taniguchi, T. *Science* **2007**, *317*, 932–934.

30 Nemanich, R. J.; Solin, S. A.; Martin, R. M. *Phys. Rev.*B **1981**, *23*, 6348– 6356.

31 Song, L.; Ci, L. J.; Lu, H.; Sorokin, P. B.; Jin, C. H.; Ni, J.; Kvashnin, A. G.; Kvashnin, D. G.; Lou, J.; Yakobson, B. I.; Ajayan, P. M. *Nano Lett.* **2010**, *10*, 3209– 3215.

32 Sing, K. S. W.; Everett, D. H.; Haul, R. A. W.; Moscou, L.; Pierotti, R. A.; Rouquerol, J.; Siemieniewska, T. *Pure Appl. Chem.* **1985**, *57*, 603–619.

33 Rouquerol, J.; Llewellyn, P.; Rouquerol, F. *Stud. Surf. Sci. Catal.* **2007**, *160*, 49–56.

34 Roy, A.; et al., J. Mol. Struct., 2002, 613, 61.

35 Singh, L.; Chopra, V. *J. Mater. Sci. Technol.* **2011**, *27*, 967–972.

36 Ma, R.; Bando, Y.; Sato, T. *Chem. Phys. Lett.* **2001**, *337*, 61–64.

37 Yin, L. W.; Bando, Y.; Golberg, D.; Gloter, A.; Li, M. S.; Yuan, X. L.; Sekiquchi, T. *J. Am. Chem. Soc.* **2005**, *127*, 16354–16355.

38 Zhu, Y. C.; Bando, Y.; Ma, R. *Adv. Mater.* **2003**, *15*, 1377–1379.

39 Hagio, T.; Kobayashi, K.; Sato, T. *J. Ceram. Soc. Jpn* **1994**, *102*, 1051–1054.

Chapter 3

Microporous BN microsponges as hydrogen accumulators

Chapter 3. Microporous BN microsponges as hydrogen accumulators

3.1 Introduction

Hydrogen can be accumulated in a solid material due to physisorption, chemisorption, and/or chemical reactions. Compared to chemisorption and chemical reactions, there are numerous advantages peculiar to the physisorption storage, such as quick adsorbing and releasing kinetics, excellent reversibility and cycling performance, which eagerly motivate me to design and find new H_2 adsorbents based on physisorption mechanisms. In the past 10 years, H_2 physisorption studies based on metal-organic frameworks (MOFs) [1–3] and porous carbons [4–7] received considerable attentions. Both type of the materials could achieve very high specific surface areas (SSAs) and pore volumes, which were considered to be the most two important factors for H_2 uptake.[7] As structural analogues of porous carbons, investigations of H_2 sorption on BN porous materials are rather scarce. From the thermodynamics point of view, the interactions of H_2 molecules and adsorbent surfaces of MOF and C are fairly weak, as revealed by their low H_2 adsorption heats (usually obviously lower than ~10 kJ mol^{-1}).[2,5] However, the theoretical calculations have implied a remarkable enhancement of interactions between H_2 and layered BN surfaces; the binding energy of H_2 on planar BN surfaces is increased as much as 50 % compared to graphite surface.[8] Design of porous BNs with suitable pore widths will further enhance the interactions between H_2 molecules and BN surfaces. And indeed, recent experiments have confirmed that BNs display higher H_2 uptakes than their C counterparts at the similar measurement conditions.[9–12]

Since detailed and systematical studies of H_2 sorption on various C materials have been performed, researchers and engineers understand that many parameters have substantial effects on the final H_2 uptake capacities on them. Besides SSA and pore volume, a smaller pore width was found to favor a higher H_2 uptake, and a linear correlation between H_2 uptake capacity and the volume or SSA of pores below 1 nm has been pointed out.[4–5] Certainly, further efforts are still needed to clarify many other factors that affect H_2 sorption on porous C materials, such as pore shapes, degree of phase ordering, chemical dopants on surface, *etc*. However, in relation to the BN-based H_2 adsorbents, there are still no any clear correlations established between the related textural parameters and their H_2 sorption capacities. I think this is mainly caused by a lack of facile preparation methods able to provide qualified porous BN samples with varied textural parameters for the detailed investigations. As I stated in Chapter 1, most of the invented strategies for the purpose of getting porous and high-surface-area BNs were relied on hard-template methods. Regretfully, a lot of drawbacks are difficult to overcome presently for these hard-template-based approaches, e.g. an

inefficient degree of precursors filling, cost concerns, as well as complex and harmful post-treating proccessing needed in order to remove templates.[13] And most of all, the resultant textural parameters, especially the SSAs and porosities of template-derived BNs, were not optimistic for the application in H_2 storage; their reported SSAs were typically in a range from 100 to 950 m^2 g^{-1}.[14−20]

In this Chapter, I synthesized a series of highly porous BN microsponges (BNMSs) *via* a simple one-step template-free reaction, and for the first time performed a systematical study in regards of correlations between their textural parameters and H_2 sorption capacities. Sample morphology and chemical compositions were characterized by scanning electron microscopy (SEM), high-resolution transmission electron microscopy (HRTEM), comprehensive elemental analysis and X-ray photoelectron spectroscopy (XPS). BN phase structures were analyzed by X-ray diffraction (XRD) and Raman spectroscopy. N_2 adsorption-desorption isotherms measured at 77 K were implemented to elucidate SSAs, pore volumes and pore size distributions (PSDs) of a material, while H_2 sorption isotherms recorded at 77 K and 0−1 MPa were applied to evaluate their H_2 uptakes. It was documented that the SSAs and pore volumes of BNMSs could be simply tuned in a wide range (920−1900 m^2 g^{-1} and 0.516−1.070 cm^3 g^{-1}, respectively) by varying the synthetic conditions. Decent and totally reversible H_2 uptakes, from 1.65 to 2.57 wt % at 1 MPa and -196 ^oC, were documented for the BNMSs. (Note that the major results in this chapter have been published in *Adv. Energy Mater. 2014, 4(7), 1301525*; *i.e.* Ref. 21)

3.2 Experimental methods

Synthesis of BN microponges. Boric acid (BA) and dicyandiamide (Dcy) with various ratios were dissolved in a hot DI water, and precipitated at their boiling point till complete water evaporation. Then, the obtained Dcy-BA powders were loaded in a horizontal tubular furnace, and calcined under a flow of NH_3 gas at preset temperatures for 3 h under a heating rate of 10 ^oC min^{-1}. The used calcination temperatures were set from 800 to 1200 °C (Figure 3.1 and Table 3.1). The products were used for further morphological and chemical composition analyses, and N_2 and H_2 adsorption-desorption characterizations without any additional treatments.

Structural and compositional characterization. The morphology and structure observations of obtained BNMSs were performed by means of a 10 kV JSM-6700 SEM and a 300 kV JEM-3000F HRTEM, respectively. Elemental compositions were analyzed as follows: the content of boron (B) was measured by ICP-OES method (IRIS advantage, Nippon Jarrell-Ash Co.). Carbon (C) content was analyzed by a carbon/sulfur determinator (CS-444LS, LECO Co.) by using $CaCO_3$ as the standard substance, while nitrogen (N) and oxygen (O) contents were measured by an oxygen/nitrogen determinator (TC-436AR, LECO Co.) by using Si_3N_4 and Y_2O_3 as the N and O standard substances, respectively. Powder XRD diffraction data were collected on a Rigaku Ultima III diffractometer (Cu Kα); Raman spectra were taken on

a Horiba Jobin-Yvon T6400 Raman spectrometer (514.5 nm excitation laser). For each recorded spectrum, the samples were exposed to a ~10 mW laser with an accumulation time of 20 s.

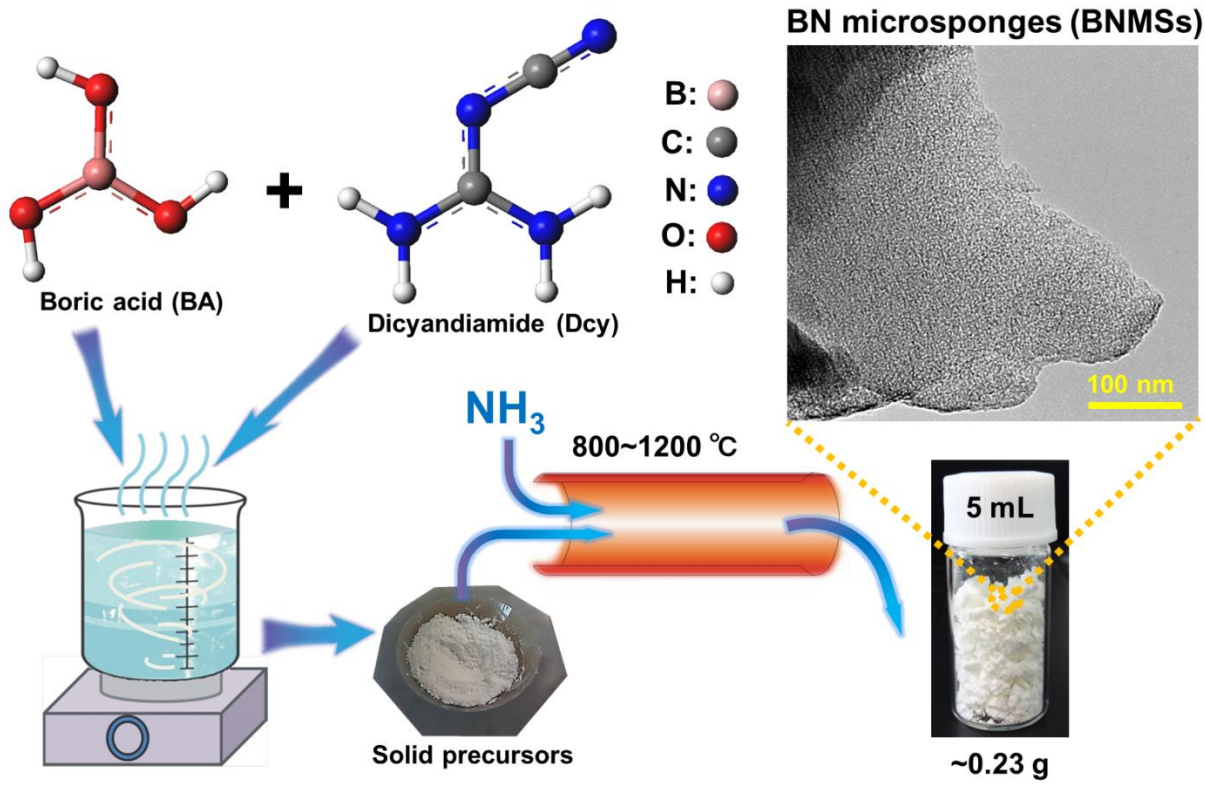

Figure 3.1 Synthesis approach for BN microsponges fabrication *via* a simple one-step template-free reaction of dicyandiamide (Dcy) and boric acid precursor. Reprinted from Ref. 21.

Table 3.1 Designation of BN microsponge samples fabricated under different conditions.

Sample notation	Dcy/BA ratios (mol/mol)	Synthesis temperature (^{o}C)
BNMS-Dcy-1-1000	1:1	1000
BNMS-Dcy-2-1000	2:1	1000
BNMS-Dcy-3-1000	3:1	1000
BNMS-Dcy-4-1000	4:1	1000
BNMS-Dcy-3-800	3:1	800
BNMS-Dcy-3-1200	3:1	1200

Reprinted from Ref. 21.

Specific surface area, porosity and H_2 sorption capacity charaterizations. N_2 physisorption isotherms recorded on a Quantachrome Autosorb-iQ system at 77 K were implemented for the calculation of specimen specific surface areas (SSAs) and porosities. The SSAs were evaluated based on the Brunauer-Emmett-Teller (BET) equation using a relative pressure range of 0.05−0.2. The pore size distribution (PSD), as well as the volume or SSA of pores below 1 nm, 2 nm and 5 nm, respectively, were calculated based on the NLDFT theory with adopting a N_2-carbon equilibrium and slit-pore model. The H_2 adsorption-desorption isotherms were recorded volumetrically on a BELSORP-HP-30 hydrogen adsorption system (BEL Japan, Inc.) at 77 K and 0−1 MPa. Prior to all N_2 and H_2 adsorption-desorption measurements, the samples were fully outgassed at 150 °C for 24 h.

3.3 Elemental analysis

One-step template-free method relying on direct reaction of B and N precursors at high temperature has been effectively employed for the syntheses of porous BN materials with high SSAs.[22,23] In the present study, BA was supplied as a B source while Dcy was selected as a N source due to its respectively high decomposition temperature. The sample notations and synthesis conditions for all BNMS samples are shown in Table 3.1. The purpose of introducing NH_3 during the calcination process at high temperatures was to remove C species that are present in the Dcy precursor and to yield finally pure BN products. To further check the chemical compositions of the obtained white and porous samples, the elemental analysis (B, C, N and O) was performed. The data show that the major B+N contents in the obtained BNMS samples are > 93 *at* %. The chemically stoichiometric ratios of B/N in different samples ranged from 0.98 to 1.02. The C component was successfully eliminated to a content lower than 0.4 *at* % in the received products by introducing NH_3 during the synthesis. I can also conclude that the higher synthesis temperatures favor more effective eliminations of the carbonaceous component in the samples. Because it was difficult to totally avoid the exposure of BNMS samples to air during the analysis, the real O contents in BNMS samples should be lower than the measured values (Table 3.2) due to adsorbed moisture. Thus, the purities of the BNMS products obtained *via* a one-step template-free reaction are considerably high.

Table 3.2 Elemental compositions of BN microsponges. Reprinted from Ref. 21.

	Samples	B (at %)	N (at %)	C (at %)	O (at %)
BNMS-Dcy-	1-1000	48	47	0.1	5.1
	2-1000	46	47	0.1	6.2
	3-1000	47	46	0.1	6.1
	4-1000	47	47	0.3	5.5
	3-800	46	46	0.4	7.2
	3-1200	47	47	<0.1	6.4

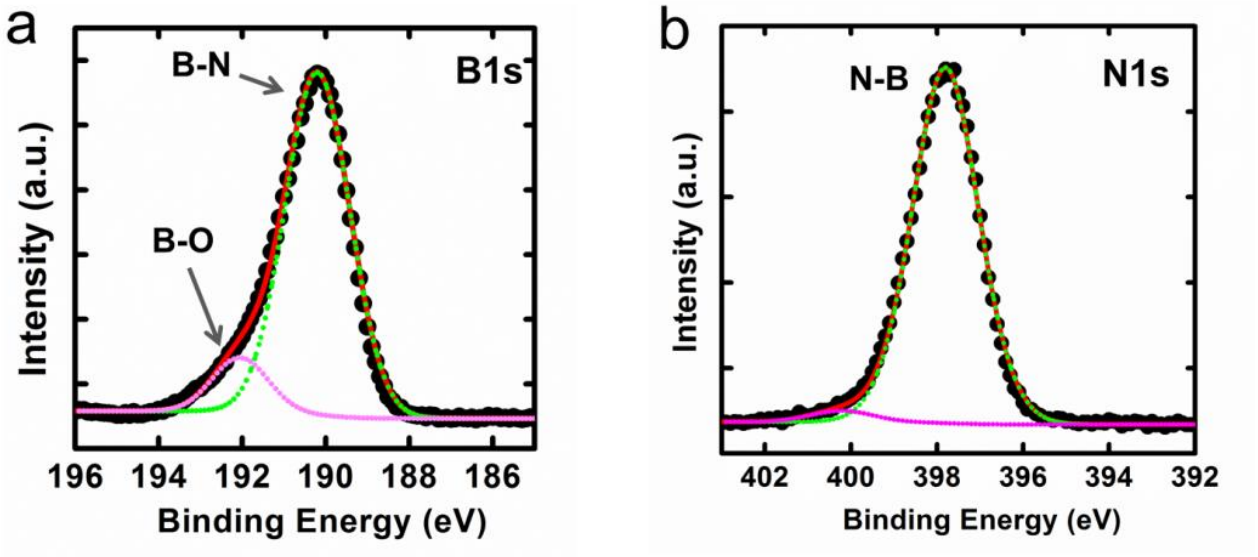

Figure 3.2 (a,b) B1s and N1s XPS spectra of a BNMS-Dcy-3-800 sample. Reprinted from Ref. 21.

Figure 3.2 shows the XPS results for a typical BNMS-Dcy-3-800 sample. The B1s spectrum reveals the main component (sp^2-hybridized BN structures) at 190.3 eV accompanied with a small peak at 191.7 eV. The minor component at high energy is assigned to B_2O_3 compound. In the N1s spectrum, the peak at 397.9 eV corresponds to the sp^2-hybridized BN structures.[24]

3.4 Structural characterizations

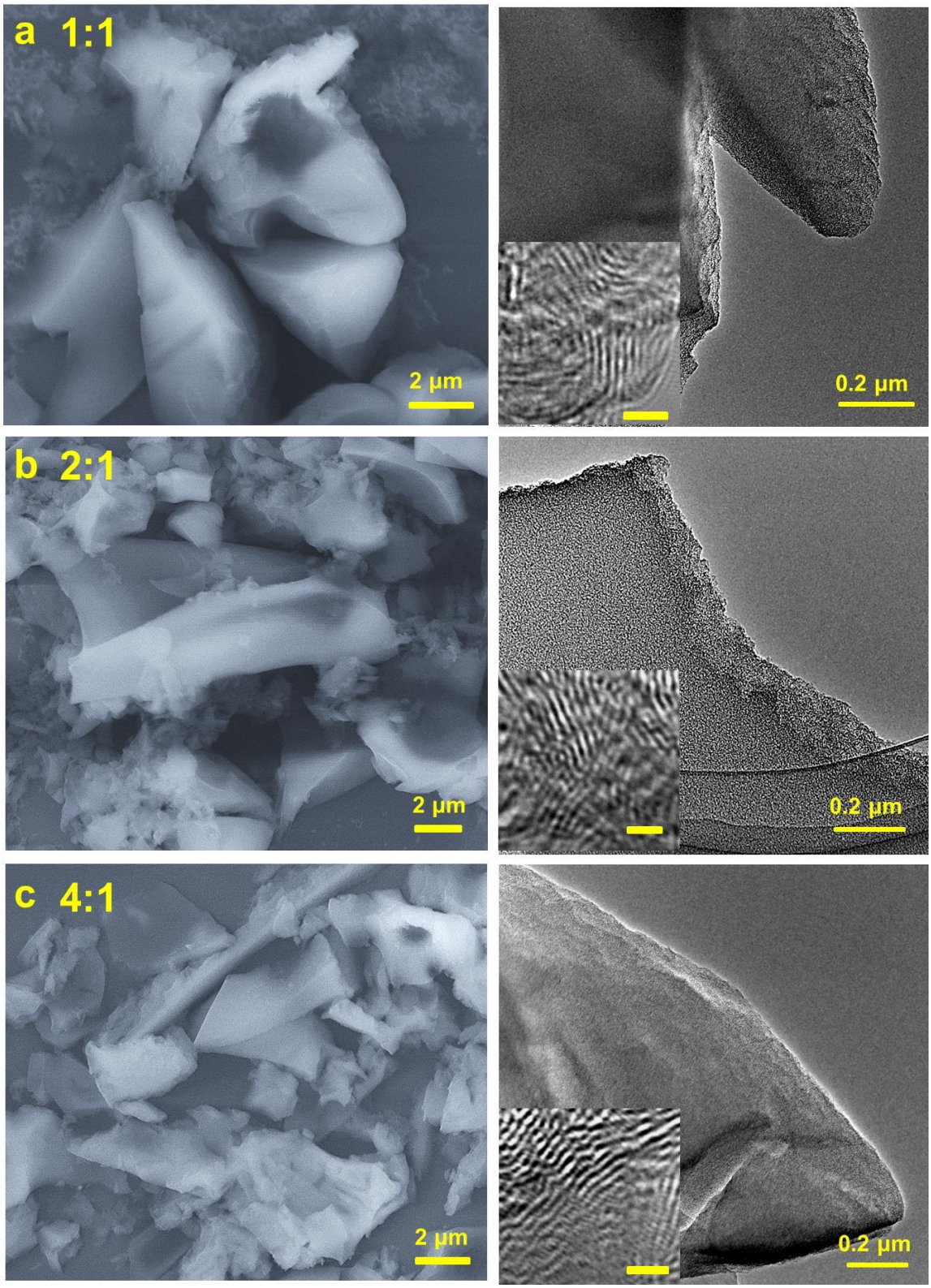

Figure 3.3 SEM (left-hand-side) and HRTEM (right-hand-side) images of BN microsponge samples prepared from Dcy-BA precursors at 1000 ^{o}C with various Dcy/BA ratios. a) 1:1, b) 2:1 and c) 4:1. The HRTEM image insets are the corresponding high-magnification TEM images. The inset scale bars are 2 nm. Reprinted from Ref. 21.

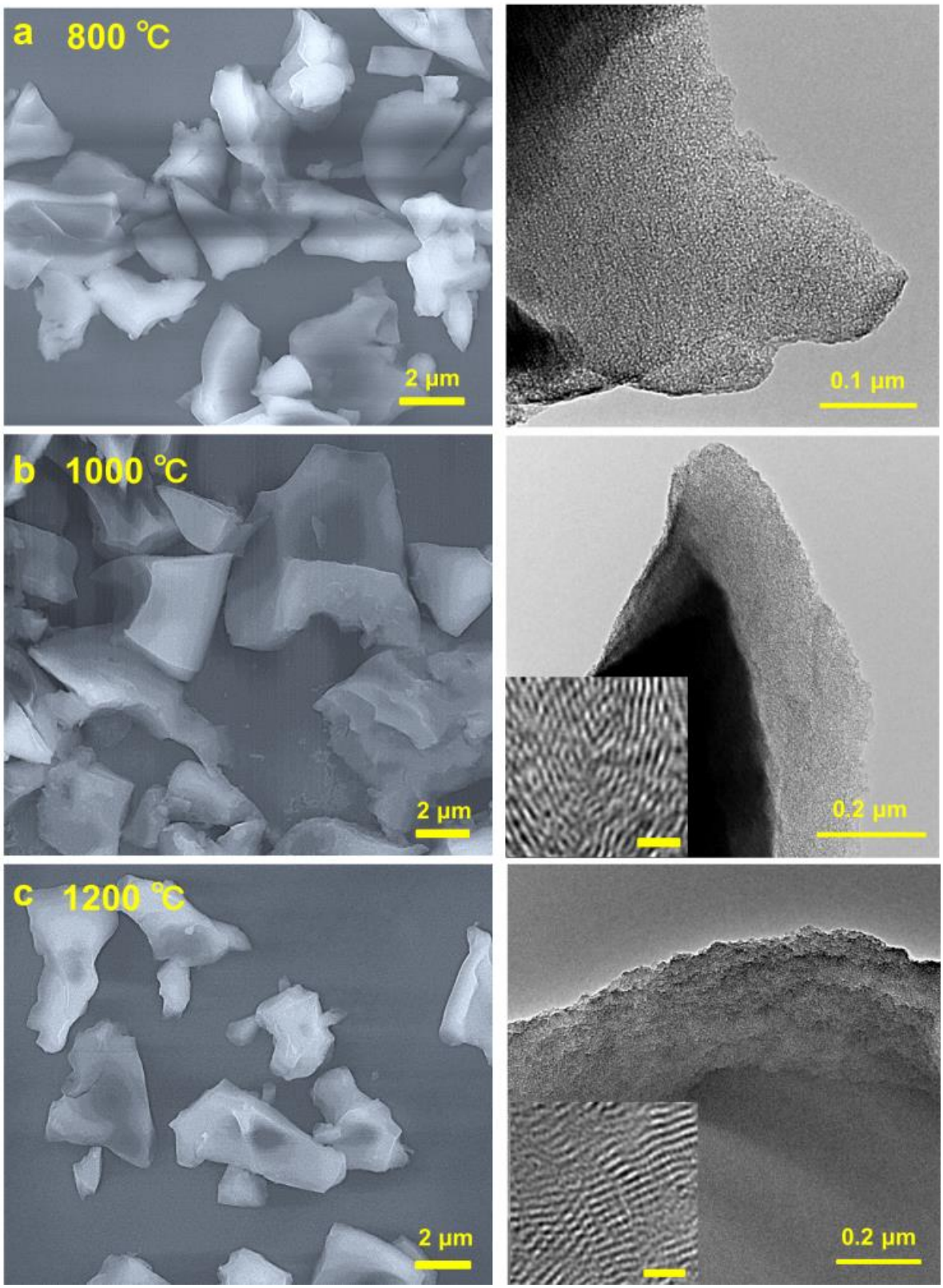

Figure 3.4 SEM (left-hand-side) and HRTEM (right-hand-side) images of BN microsponge samples prepared from the Dcy-BA precursor with a ratio of Dcy/BA = 3:1 at various temperatures. a) 800 °C, b) 1000 °C and c) 1200 °C. The insets in TEM images are corresponding HRTEM images. The inset scale bars are 2 nm. Reprinted from Ref. 21.

The as-made BN products typically exhibit irregular and twisted polygon appearances with the sizes varying from submicrometer to tens of micrometers. Careful SEM and low-magnification TEM characterizations (Figure 3.3 and 3.4) show no obvious presence of meso- and macropores in Dcy-derived BNMSs. Further high-magnification TEM characterizations of these BNMSs confirm the prevailing of dislocation structures in the fabricated BN phases, which provides indication of the formation of highly porous morphologies. Although no clear changes of the structures were found in the products along with the change of Dcy/BA ratio, the higher synthesis temperature favors the improvement of BN phase ordering in the BNMS products. Under increasing synthesis temperatures from 800 to 1200 ° C, the ordering of the BN phases improves (Figure 3.4). It is generally accepted that slit-shaped pores in BN materials that are derived from enlarged adjacent (0002) layer spacings are unfavourably formed in highly ordered BN materials like *h*-BN and multiwalled BN nanotubes (MWBNNTs). The reason is that the (0002) plane interactions in these highly ordered BN forms are usually quite strong due to a rather small (0002) distance (0.33−0.34 nm), which exceeds the minimum probing limit for normally used physical adsorption methods. Thus, the ordering problems in BN phases that take place at high temperatures, in fact, hinder the formation of highly porous BN materials.

Figure 3.5 (c) shows the schematic illustration of partially disordered phases of BNMSs, in which structural dislocations between BN (0002) layers and two types of pores (*P1* and *P2*) are highlighted. Usually, the pore width of *P1* micropores that originates from the enlarged interlayer distances is ~0.4 nm. However, *P2* pores, that are featured by the pore width larger than 1 nm, are much more structurally complicated and made of the un-parallel BN (0002) planes. Figure 3.5 (a) shows a typical HRTEM image of BNMS-Dcy-3-800, revealing branched dislocation structures, as well as *P1* and possible *P2* pore locations. It is not difficult to discover that the enlarged (0002) fringes are preferably formed near the dislocation positions. However, discerning *P2* pores in these projected 2D HRTEM images and further reconstruction of the real 3D porous structures for these BNMSs is a difficult task. In Figure 3.5 (a), the labeled locations that are surrounded by vertical BN multi-walls (in parallel with the e-beam incidence) also contain several horizontal BN layers (perpendicular, or nearly perpendicular to the e-beam). In many possible structural models that can shed a light on the formation of such regions, the existence of few-nanometer-sized hollow structures (*i.e. P2* pores), that are constructed *via* un-parallel or crossed BN (0002) layers, are very reasonable. Noting that dislocation structures that are prevailing in the present BNMSs introduce strong sp^3-hybridized bonds between or within BN layers to maintain such highly porous structures, and to avoid ordering and collapsing of pores at high temperatures under the syntheses. Similar peculiar dislocation structures have also been recently reported in anthracites and BN porous microbelts.[23,25]

BNMSs' XRD patterns show two broaden and less visible (0002) and (10-10) peaks located at 2θ = 23.17−24.86 and 42.76−42.92^o, respectively (Figure 3.5 (b) and Chapter 6). This is caused by their partially disordered BN phases, as also confirmed by HRTEM characterizations. The largest d_{0002} value derived from

(0002) patterns is 0.384 nm (BNMS-Dcy-3-800 and BNMS-Dcy-3-1000). Clearly, d_{0002} tends to shrink with an increase of the synthetic temperatures. This is because the layered BN materials with a (0002) distance of ~0.33 nm exhibit the highest thermal stability, such as *h*-BN. However, with an increase of Dcy/BA ratio, BNMS-Dcy-3-1000 with the Dcy/BA = 3:1 displays the largest (0002) distances of 0.384 nm, as shown in Figure 3.5 (b). Further increasing in the proportion of N precursor starts to narrow the (0002) distances. BN (0002) interlayer interactions and size of ordering phases can also be analyzed from their Raman shifts and FWHM values.[26,27] When E_{2g} vibration upshifts toward the higher frequency compared to bulk *h*-BN, this implies a weaker (0002) interlayer interaction for the measured BN phases.[26,28] As shown in Figure 3.5 (b), the prepared BNMS samples display obviously broadened and upshifted E_{2g} peaks at 1372.2−1376.5 cm^{-1} with FWHM values of 29−42 cm^{-1}. Just like the changing trends of d_{0002} values, the E_{2g} vibrations tend to downshift with an increase of the synthetic temperature, while a moderate Dcy/BA ratio = 3:1 is able to minimize the interlayer interactions in the prepared BNMS sample, as seen from its upshifted E_{2g} value.

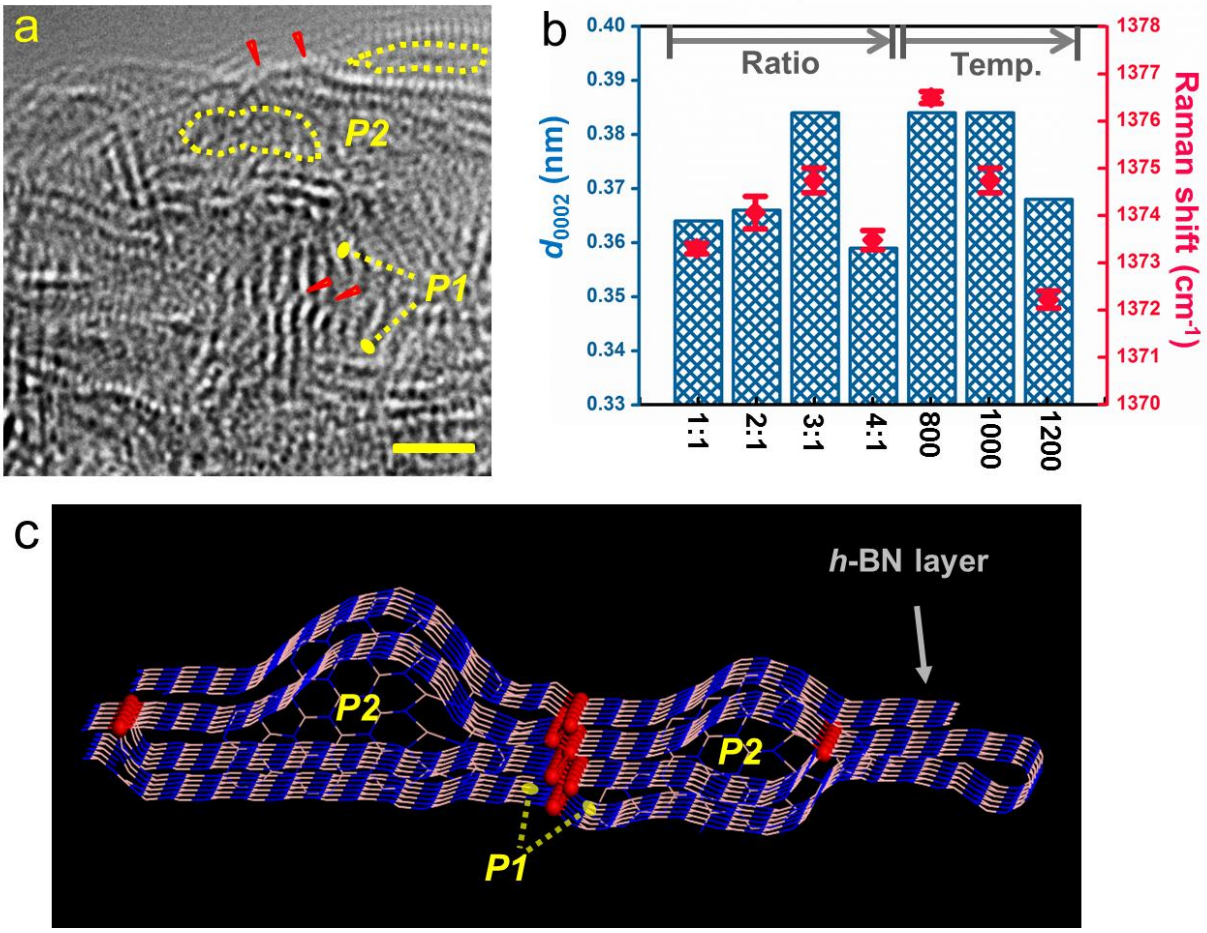

Figure 3.5 (a) HRTEM image of a BN microsponge specimen obtained while using Dcy/BA = 3 and T= 800 ^{o}C. Dislocation sites, *P1* and possible *P2* pores are labeled with red arrows and yellow dashed frames, respectively. Scale bar in (a) is 2 nm. (b) Summary of XRD (0002) lattice distances and Raman E_{2g} shifts of the BNMS products. (c) Schematics of the dislocation and pore structures in the obtained BN microsponges. The corresponding dislocation positions are marked in red; *P1* and *P2* pore types are also labeled. Reprinted from Ref. 21.

-

3.5 Porosity of the BN microsponge materials

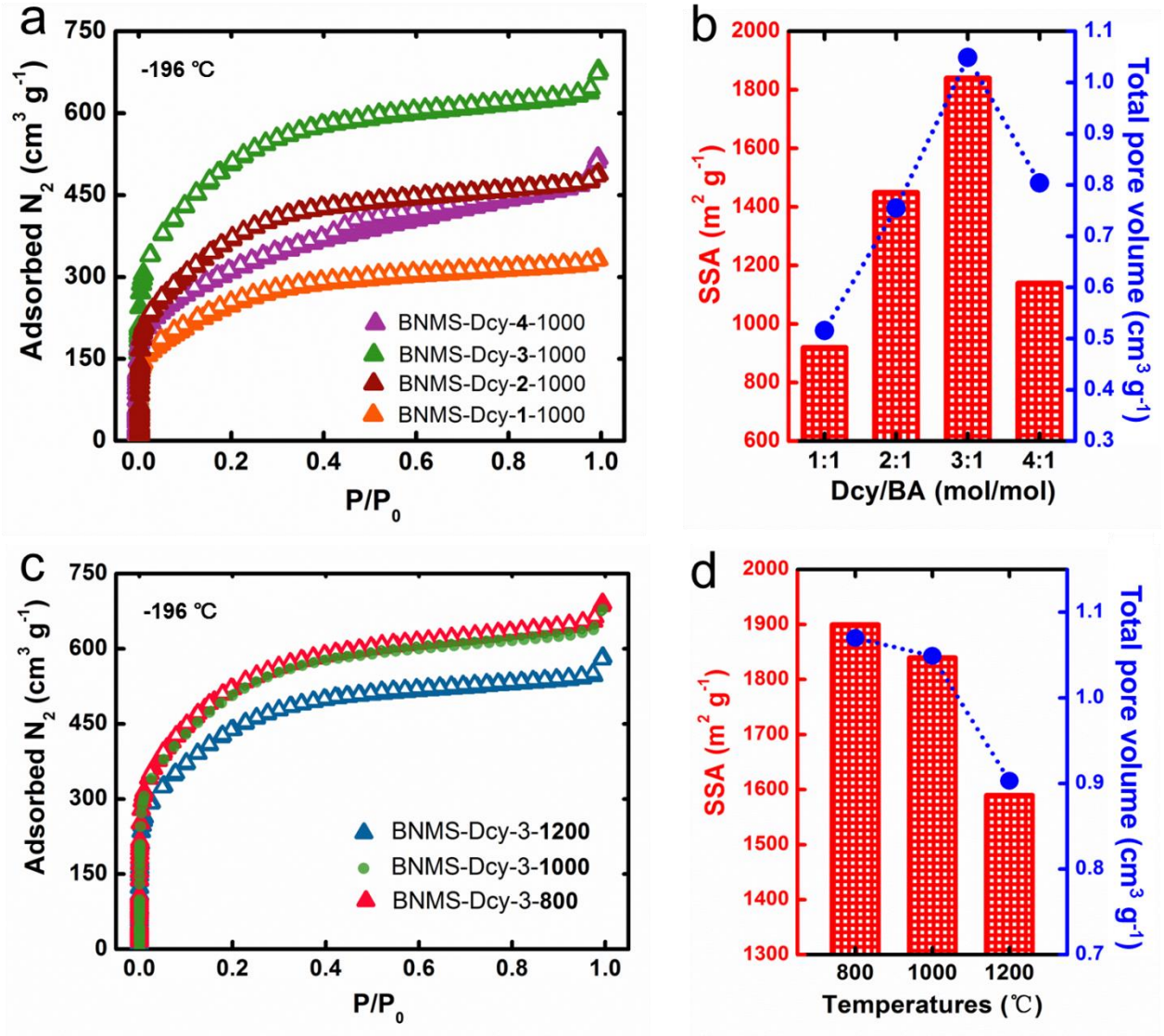

Figure 3.6 (a) Nitrogen adsorption-desorption isotherms and (b) BET specific surface areas (SSAs) and total pore volumes of BN microsponges synthesized with different Dcy/BA ratios at a fixed temperature of 1000 ^{o}C. (c) Nitrogen adsorption-desorption isotherms and (d) BET SSAs and total pore volumes of BNMSs synthesized at various temperatures while maintaining the fixed ratio of Dcy/BA = 3:1. Reprinted from Ref. 21.

The SSAs and porosity of all BNMS samples were characterized by N_2 adsorption-desorption method. The isotherms of Dcy-derived BNMSs belong to the typical type Ⅰ isotherm, and no remarkable hysteresis loops are recorded for these BNMS products. The presence of micropores is nicely revealed by the dramatic increases of N_2 adsorptions at a low relative pressure range for all Dcy-BNMSs (Figure 3.6). Following the BET analysis criteria for microporous materials, the relative pressure range selected in the present studies

was 0.05−0.2.[29] As depicted in Figure 3.6 (b), the SSA of Dcy-BNMSs increases from 920 to 1840 m^2 g^{-1} along with an increase of Dcy/BA ratio from 1:1 to 3:1. Further increase of Dcy/BA ratio to 4:1 leads to decreasing the SSA value to 1140 m^2 g^{-1}. The corresponding total pore volume (P/P_0 = 0.99) shows a similar trend as a function of Dcy/BA ratio (Figure 3.6 (b)), suggesting the necessity of a proper Dcy/BA ratio for the optimization of the sample textural properties, including SSA and pore volume. Besides, temperature-dependent experiments further evidence that the Dcy-derived BN microsponge synthesized at Dcy/BA = 3:1 and T = 800 °C shows the largest SSA and pore volume (up to 1900 m^2 g^{-1} and 1.070 cm^3 g^{-1}). This is among the largest SSA values for any BN materials ever reported. As seen in Figure 3.6 (d), rising synthesis temperatures makes corresponding SSAs and total pore volumes to shrink; *e.g.*, the SSA and total pore volume of BNMS-Dcy-3-1200 that prepared at 1200 °C reduce to 1590 m^2 g^{-1} and 0.903 cm^3 g^{-1}, respectively. Combined with the corresponding HRTEM, XRD and Raman results, I can attribute this decrease phenomenon of SSAs and pore volumes to the ordering or crystallization of BN phases in BNMSs along with the rise of synthesis temperature.

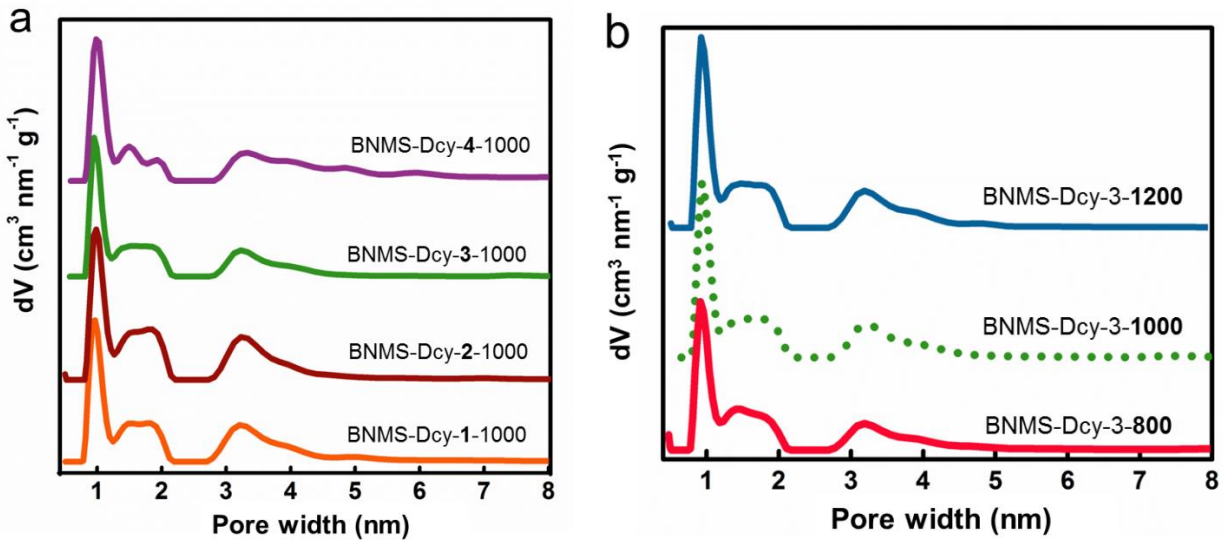

Figure 3.7 (a) Pore size distribution (PSD) profiles derived in the frame of quenched solid density functional theory (QSDFT) for BN microsponges made at different Dcy/BA ratios and at a fixed synthesis temperature of 1000 °C. (b) PSD profiles of BNMSs synthesized at different temperatures while fixing the ratio of Dcy/BA as 3:1. Reprinted from Ref. 21.

Then the quenched solid density functional theory (QSDFT) was applied by me to calculate the pore widths and PSDs. The advantage of this method is taking into account the surface heterogeneity and roughness, that is more reasonable for the cases of BN and C materials.[30-32] As depicted in the PSD profiles of all BNMSs, the dominant peak is 1.0 nm along with the two broad and less intense peaks located within 1.2−2.1 and 2.8−4.5 nm ranges, respectively (Figure 3.7). The main type of porosity for the investigated BNMSs is microporosity (0.273−0.625 cm^3 g^{-1}, Table (3.2), except the BNMS-Dcy-4-1000 sample. This is

also eveidenced by an obvious N_2 adsorption in a higher pressure range for the BNMS-Dcy-4-1000 isotherm, which is different from other isotherms shown in Figure 3.6. Meanwhile, the corresponding PSD profile of BNMS-Dcy-4-1000 also confirms the existence of larger pores with a width >4.5 nm. However, the general lack of mesopores and macropores in the obtained BNMS products, as implied by their PSD profiles, is in a good agreement with the above-discussed SEM and HRTEM observations.

3.6 Porosity formation mechanisms via a non-template reaction

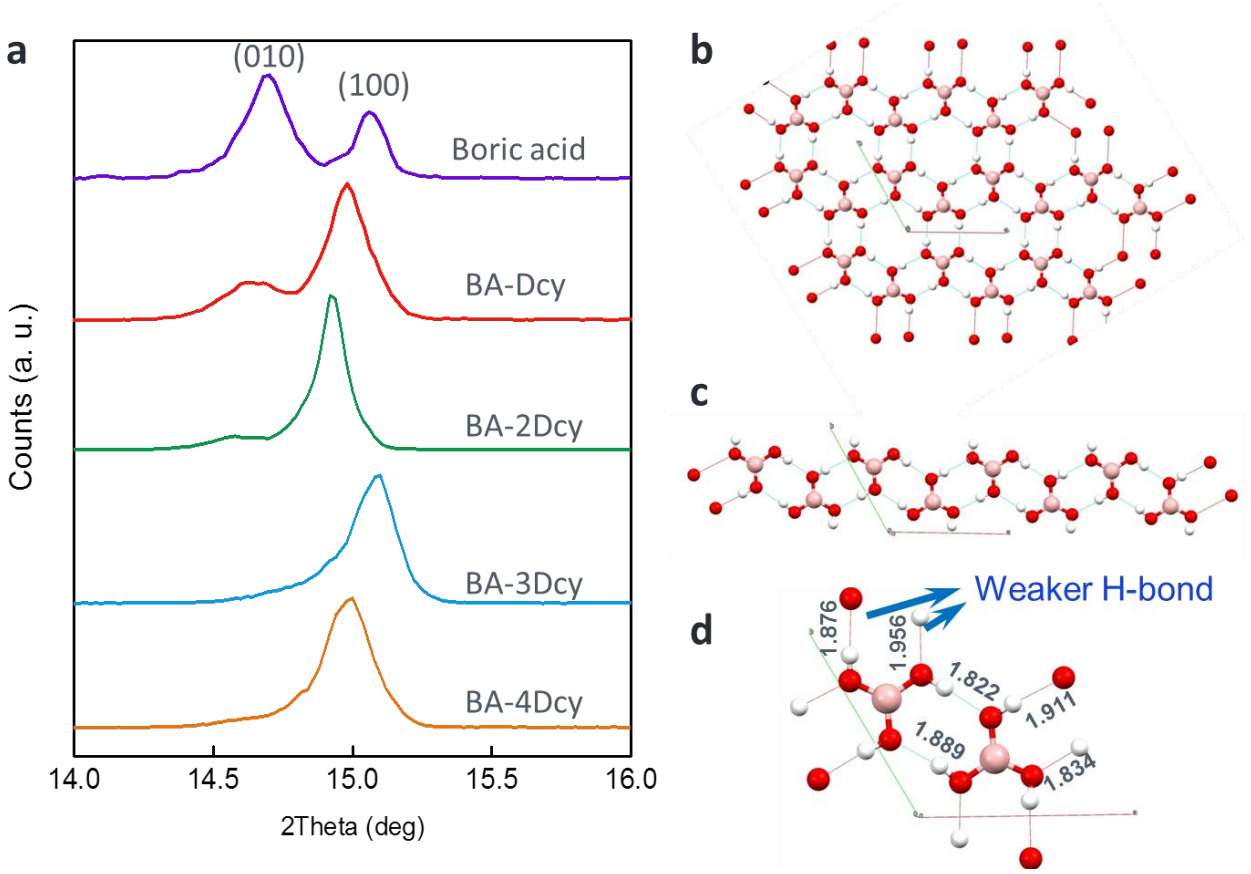

Figure 3.8 (a) XRD patterns of Dcy/BA precursors with different ratios. (b) Crystal structure of boric acid viewed along the [001] direction. (c) Boric acid molecular chains with H-bond interactions along the [100] direction. (d) Bond lengths for the H-bonds within boric acid molecules.

As described above, the SSA and pore volume of the obtained BNMS products show ratio-dependent behavior with respect to the precursors used. To have deeper insights into the formation mechanisms of the porous structures for the present BN materials, XRD characterization was carried out. Figure 3.8 (a) shows the evolution of the BA(010) and (100) reflections along with the change of the Dcy/BA ratio. The interactions for BA(100) planes are basically maintained, while the long-range ordering of (010) planes

gradually disappears, forming BA molecule chains surrounded by Dcy molecules in the Dcy/BA adducts. This phenomenon is particularly obvious in the Dcy/BA precursors with ratios of 3:1 and 4:1.

A reasonable explanation for this ratio-dependent BNMS porosity formation is that the pores in BNMSs should be formed along with the decomposition of N precursors (Dcy) at a high temperature. A molecular-level mixing of BA and Dcy is vital for the effective reaction between hydroxyl groups and amino groups to form a BN product with the loss of water. With the generation and release of water and other small gaseous molecules, open pores are formed being accompanied by the reconstructions BN phase and the "void" spaces caused by the loss of H, C and O atoms. Without enough N precursors, BA may hardly react completely, and plentiful number of closed pores that can't adsorb N_2 and H_2 molecules would still retain in the BN solids. On the contrary, with a supply of the excess N precursors, most of the space that has firstly been occupied by N precursors is emptied under the decomposition of Dcy, larger pores would thus be formed like in the case of BNMS-Dcy-4-1000 sample.

3.7 Hydrogen storage performance

H_2 uptakes of the obtained BNMSs were evaluated while analyzing their adsorption-desorption isotherms at -196 ^oC and 0−1 MPa. As depicted in Figure 3.9, the total reversibility seen in these isotherms implies the physisorption-dominated H_2 adsorption mechanism in the fabricated materials. H_2 uptake as a function of different synthetic conditions, i.e. Dcy/BA ratio and synthesis temperature, follows the corresponding trends of SSA or total pore volume. Among all BNMSs synthesized with different Dcy/BA ratios, the BNMS made while using a proper Dcy/BA ratio (3:1) exhibits the highest H_2 uptake of 2.39 wt % at 1 MPa. Meanwhile, using a bit lower synthesis temperature favors obtaining the BNMS with larger H_2 uptakes. *E.g.* BNMS-Dcy-3-800 shows the largest H_2 uptakes of 1.34 (0.1 MPa) and 2.57 wt % (1 MPa) among all Dcy-BNMS samples. Taking into consideration the compressed H_2 that has been filled in free pore volumes, the total H_2 uptake of BNMS-Dcy-3-800 is calculated as 2.60 wt % at 1 MPa and -196 ^oC with the corresponding gravimetric energy capacity of ~0.87 kWh kg^{-1} on a materials basis. It is noted that the enhanced H_2 uptake documented here presents a ~7.6-fold increase compared to a value of surface-modified BNNTs at the same measurement conditions (1 MPa and -196 ^oC),[33] and it is also larger than the best H_2 sorption capacity for the recently developed BN microbelts (discussed in Chapter 2).[23] However, these achieved storage capacities are still lower of those for the compressed H_2 at 70 MPa on the system basis, also they are still not fully satisfying the DOE's goals.[34,35]

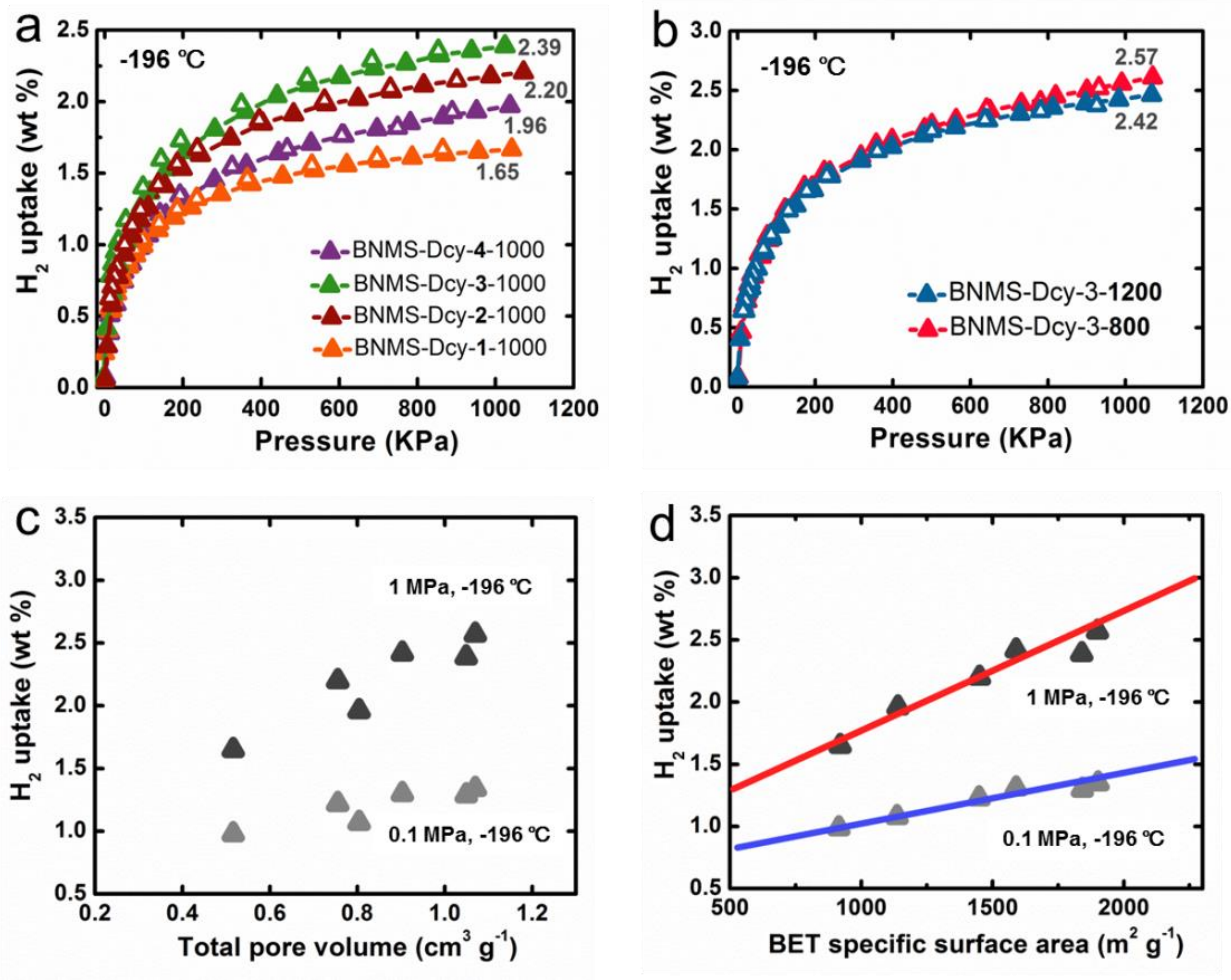

Figure 3.9 Hydrogen adsorption-desorption isotherms measured at -196 °C for BNMSs synthesized with different Dcy/BA ratios at 1000 °C (a), and at various temperatures with a fixed Dcy/BA = 3:1 (b). (c,d) H_2 uptake at 0.1 and 1 MPa (-196 °C) for BNMSs as a function of total pore volume and BET SSA, respectively. Reprinted from Ref. 21.

Besides SSAs and pore volumes, additional parameters which are not considered in my discussion, i.e. pore width, pore geometry and surface chemistry, can also have potential influences on H_2 sorption capacities and behaviors. For porous C materials, a narrower pore width (<1 nm) was found to favour a larger H_2 uptake.[5,6] This is because the attraction force between the adsorbates and solid surface is larger if the adsorbate molecules are located in narrower pores, wherein these molecules can be attracted by more surface atoms. It is still not certain what should be the most effective pore width in the porous BN materials for H_2 storages. However, due to the stronger interactions between H_2 and BN surfaces, one can expect that the effective pore width for porous BNs during H_2 sorption is larger than for their C analogues.[5,8] Pore geometry would have a similar effect on the resultant H_2 uptake by affecting the interactions between H_2 molecules and a solid surface. It is generally accepted that H_2 affinity on porous adsorbent surfaces is greatly influenced through their chemical environments. This is understandable because the electronic structure of the material surfaces can be changed by the dopant introduction. In case of porous C materials, such effects

were already documented under both experimental and theoretical investigations *via* introducing nitrogen or sulfur dopants in a C network.[36-40] Obviously, more efforts are still needed to further clarify on the above-discussed potential factors for H_2 sorption in porous BN materials. And notably, my study has provided a simple and effective method to fabricate porous BN materials with ultra-high SSAs and porosities, which is the decent background for attacking these problems in the nearest future.

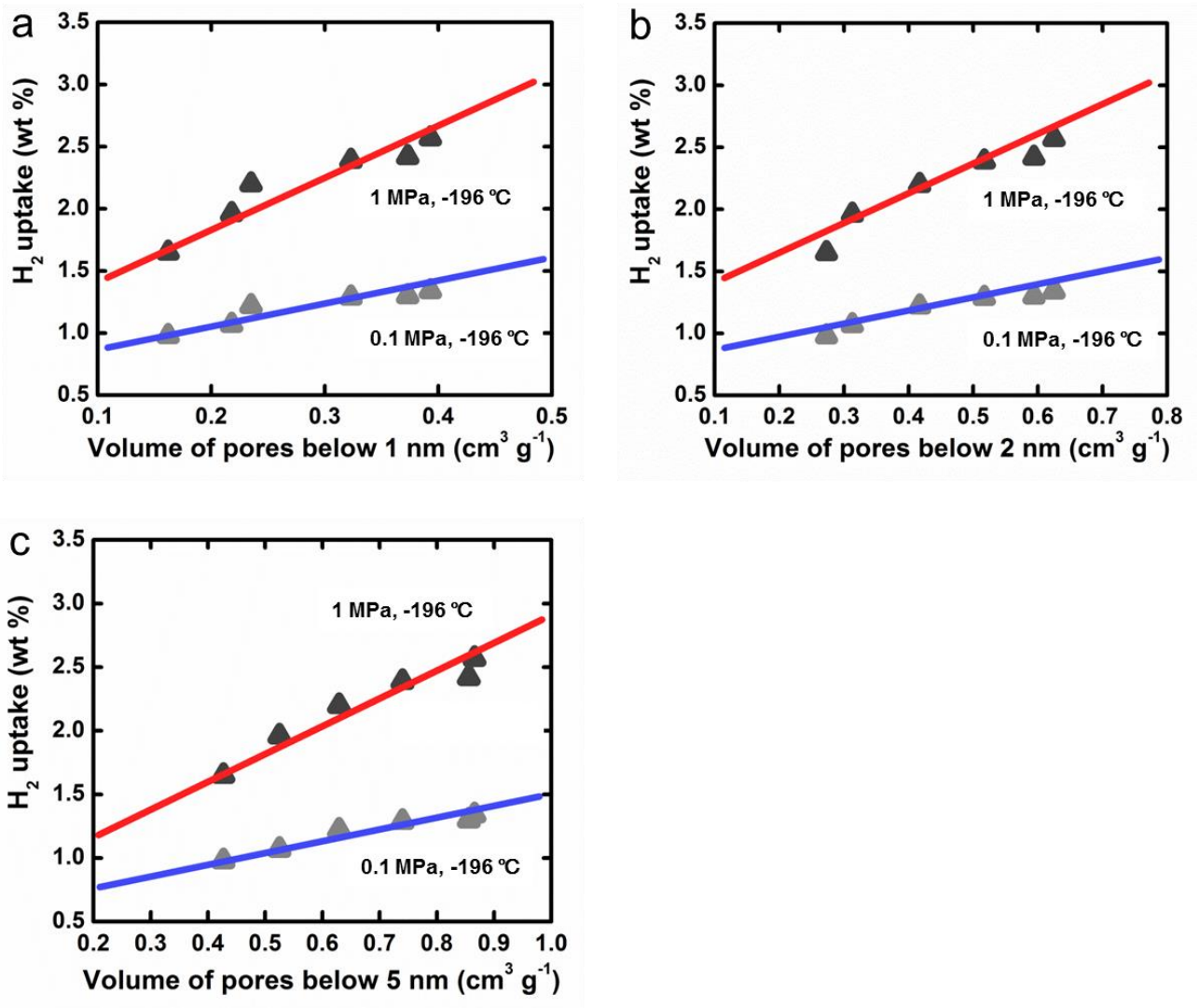

Figure 3.10. Plotting of H_2 uptake capacity at 0.1 and 1 MPa (-196 ^{o}C) for BNMSs *versus* the volume of pores below 1 nm (a), *versus* the volume of pores below 2 nm (b), and *versus* the volume of pores below 5 nm (c), respectively. Reprinted from Ref. 21.

Table 3.2 Summary of textural characteristics and H_2 uptake of the BNMS samples.

Samples		BET SSA ($m^2\ g^{-1}$)	Langmuir SSA ($m^2\ g^{-1}$)	Total pore volume ($cm^3\ g^{-1}$)[a]	Micropore volume ($cm^3\ g^{-1}$)[b]	H_2 uptake (wt %)[c]	
						0.1 MPa	1 MPa
BNMS-Dcy-	1-1000	920	600	0.516	0.273	0.98	1.65
	2-1000	1450	1070	0.755	0.417	1.22	2.20
	3-1000	1840	1270	1.049	0.517	1.29	2.39
	4-1000	1140	1090	0.804	0.313	1.07	1.96
	3-800	1900	1310	1.070	0.625	1.34	2.57
	3-1200	1590	1550	0.903	0.594	1.30	2.42

[a]The total pore volume is calculated at $P/P_0 = 0.995$. [b]The micropore volumes are calculated by QSDFT method applied to nitrogen adsorption isotherm. [c]Hydrogen sorption capacities are measured volumetrically at -196 ^oC and different pressures. Reprinted from Ref. 21.

3.8 Summary

In this Chapter, I effectively prepared highly porous sponge-like BN materials *via* a simple one-step template-free method at moderate conditions. By controlling the used N precursor/boric acid ratios and temperatures, a large number of BN sponge-like samples with varied SSAs and porosities (dominated by microporosity) were obtained. The BN microsponges are characterized by the widen (0002) interlayer spacings, partially disordered BN phase and the appearance of specific dislocation structures. The availability of plentiful porous BN samples offers the rare possibility to systematically investigate the correlations between textural properties and H_2 sorption capacities. An appropriate N precursor/boric acid ratio combined with a moderate synthetic temperature are necessary for the production of the BN microsponge samples with the ultra-high SSA (up to 1900 $m^2\ g^{-1}$), porosity (1.070 $cm^3\ g^{-1}$), and H_2 uptake (2.57 wt %, at –196 °C and 1 MPa).

3.9 References

1 Rowsell, J. L. C.; Yaghi, O. M. *Angew. Chem., Int. Ed.* **2005**, *44*, 4670–4679.

2 Murray, L. J.; Dincă, M.; Long, J. R. *Chem. Soc. Rev.* **2009**, *38*, 1294–1314.

3 Suh, M. P.; Hye, J. P.; Prasad, T. K.; Lim, D. W. *Chem. Rev.* **2012**, *112*, 782–835.

4 Gogotsi, Y.; Dash, R. K.; Yushin, G.; Yildirim, T.; Laudisio, G.; Fischer, J. E. *J. Am. Chem. Soc.* **2005**, *127*, 16006–16007.

5 Yushin, G.; Dash, R.; Jagiello, J.; Fischer, J. E.; Gogotsi, Y. *Adv. Funct. Mater.* **2006**, *16*, 2288–2293.

6 Wang, H. L.; Gao, Q. M.; Hu, J. *J. Am. Chem. Soc.* **2009**, *131*, 7016–7022.

7 Yang, S. J.; Kim, T.; Im, J. H.; Kim, Y. S.; Lee, K.; Park, C. R. *Chem. Mater.* **2012**, *24*, 464–470.

8 Jhi, S. H.; Kwon, Y. K. *Phys. Rev. B* **2004**, *69*, 245407.

9 Ma, R. Z.; Bando, Y.; Zhu, H. W.; Sato, T.; Xu, C. L.; Wu, D. H. *J. Am. Chem. Soc.* **2002**, *124*, 7672–7673.

10 Wang, P.; Orimo, S.; Matsushima, T.; Fujii, H.; Majer, G. *Appl. Phys. Lett.* **2002**, *80*, 318–320.

11 Lim, S. H.; Luo, J. Z.; Ji, W.; Lin, J. *Catal. Today* **2007**, *120*, 346–350.

12 Van den Berg, A. W. C.; Otero Arean, C. *Chem. Commun.* **2008**, 668–681.

13 Portehault, D.; Giordano, C.; Gervais, C.; Senkovska, I.; Kaskel, S.; Sanchez, C.; Antonietti, M. *Adv. Funct. Mater.* **2010**, *20*, 1827–1833.

14 Han, W. Q.; Brutchey, R.; Tilley, T. D.; Zettl, A. *Nano Lett.* **2004**, *4*, 173−176.

15 Dibandjo, P.; Chassagneux, F.; Bois, L.; Sigala, C.; Miele, P. *J. Mater. Chem.* **2005**, *15*, 1917−1923.

16 Rushton, B.; Vinu, A.; Terrones, M.; Golberg, D.; Hishita, S.; Ariga, K.; Mori, T. *Chem. Mater.* **2005**, *17*, 5887–5890.

17 Dibandjo, P.; Bois, L.; Chassagneux, F.; Miele, P. *J. Eur. Ceram. Soc.* **2007**, *27*, 313–317.

18 Mokaya, R. *J. Mater. Chem.* **2008**, *18*, 235−241.

19 Alauzun, J. G.; Ungureanu, S.; Brun, N.; Bernard, S.; Miele, P.; Backov, R.; Sanchez, C. *J. Mater. Chem.* **2011**, *21*, 14025−14030.

20 Schlienger, S.; Alauzun, J.; Michaux, F.; Vidal, L.; Parmentier, J.; Gervais, C.; Babonneau, F.; Bernard, S.; Miele, P.; Parra, J. B. *Chem. Mater.* **2012**, *24*, 88–96.

21 Weng, Q. H., Wang, X., Bando, Y., Golberg, D. *Adv. Energy Mater*. **2014**, 4, 1301525.

22 Nag, A.; Raidongia, K.; Hembram, K. P. S. S.; Datta, R.; Waghmare, U. V.; Rao, C. N. R. *ACS Nano* **2010**, *4*, 1539–1544.

23 Weng, Q. H.; Wang, X. B.; Zhi, C. Y.; Bando, Y.; Golberg, D. *ACS Nano* **2013**, *7*, 1558–1565.

24 Lei, W.; Portehault, D.; Dimova, R.; Antonietti, M. *J. Am. Chem. Soc.* **2011**, *133*, 7121–7127.

25 Sun, Y. Q.; Alemany, L. B.; Billups, W. E.; Lu, J. X.; Yakobson, B. I. *J. Phys. Chem. Lett.* **2011**, *2*, 2521–2524.

26 Gorbachev, R. V.; Riaz, I.; Nair, R. R.; Jalil, R.; Britnell, L.; Belle, B. D.; Hill, E. W.; Novoselov, K. S.; Watanabe, K.; Taniguchi, T. *et al. Small* **2011**, *7*, 465–468.

27 Nemanich, R. J.; Solin, S. A.; Martin, R. M. *Phys. Rev. B* **1981**, *23*, 6348–6356.

28 Kubota, Y.; Watanabe, K.; Tsuda, O.; Taniguchi, T. *Science* **2007**, *317*, 932–934.

29 Rouquerol, J.; Llewellyn, P.; Rouquerol, F. *Stud. Surf. Sci. Catal.* **2007**, *160*, 49–56.

30 Neimark, A. V.; Lin, Y.; Ravikovitch, P. I.; Thommes, M. *Carbon* **2009**,*47*, 1617–1628.

31 Zhu, Y.; Murali, S.; Stoller, M. D.; Ganesh, K. J.; Cai, W.; Ferreira, P. J.; Pirkle, A.; Wallace, R. M.; Cychosz, K. A.; Thommes, M.; Su, D.; Stach, E. A.; Ruoff, R. S. *Science* **2011**, *332*, 1537–1541.

32 Cychosz, K. A.; Guo, X.; Fan, W.; Cimino, R.; Gor, G. Y.; Tsapatsis, M.; Neimark, A. V.; Thommes, M. *Langmuir* **2012**, *28*, 12647–12654.

33 Terao, T.; Bando, Y.; Mitome, M.; Kurashima, K.; Zhi, C. Y.; Tang, C. C.; Golberg D. *Physica E* **2008**, *40*, 2551–2555.

34 von Helmolt, R.; Eberle, U. *J. Power Sources* **2007**, *165*, 833–843.

35 US Department of Energy, Targets for Onboard Hydrogen Storage Systems for Light-Duty Vehicles, http://www1.eere.energy.gov/hydrogenandfuelcells/storage/pdfs/targets_onboard_hydro_storage_explanation.pdf

36 Zhu, Z. H.; Hatori, H.; Wang, S. B.; Lu, G. Q. *J. Phys. Chem. B* **2005** ,*109*, 16744–16749.

37 Yang, Z.; Xia, Y.; Sun, X.; Mokaya, R.; *J. Phy. Chem. B* **2006**, *110*, 18424–18431.

38 Pacula, A.; Mokaya, R. *J. Phys. Chem. C* **2008**, *112*, 2764–2769.

39 Xia, Y.; Walker, G. S.; Grant, D. M.; Mokaya, R. *J. Am. Chem. Soc.* **2009**, *131*, 16493–16499.

40 Xia, Y.; Mokaya, R.; Grant, D. M.; Walker, G. S. *Carbon* **2011**, *49*, 844–853.

41 Sevilla, M.; Fuertes, A. B.; Mokaya, R. *Int. J. Hydrogen Energy* **2011**, *36*, 15658–15663.

Chapter 4

Hydrogen sorption behaviors of BCNO porous microbelts with ultra-narrow and tunable pore widths

Chapter 4. Hydrogen sorption behaviors of BCNO porous microbelts with ultra-narrow and tunable pore widths

4.1 Introduction

Carbon (C) and boron nitride (BN) are the two isoelectronic materials; both of them can form analogous structures, from cages,[1-3] tubes,[4,5] sheets,[6,7] to other high-dimensional structures. C and BN nanotubes and nanosheets share superb performances featuring huge mechanical strength and high thermal conductivity.[7-9] However, some other features, particularly perfect chemical innerness and thermal stability, remarkably distinguish nano-/micro BNs from their C analogues.[10,11] Due to the partially ionic property of B-N bonds, BN materials are wide energy-band-gap semiconductors, these are very different from metallic, semi-metallic and narrow-band semiconducting C materials.[12,13] It is a smart and practical idea to tune band gaps of BN or C *via* introducing C atoms into BN nano/mcirostructures or *vice versa* to form BCN hybrids with controlled compositions. In addition, the heteropolar nature of B-N bond is also thought to be the origin of the higher H_2 affinity on BN surfaces compared to that on C.[14] In addition, through C and O-doping, it is possible to introduce structural defects and to modify the local electric fields of BN surface, and thus to provide possibilities for more effective screening H_2 adsorbents within the BN system. And indeed, graphene oxide (GO) and carbon nanotube (CNT) composite were reported to show higher H_2 uptakes than the reduced GO-CNT composites,[15] indicating an important role of O on the material surfaces for improving the H_2 affinity on the regarded adsorbents. Taken all these factors together, it is timely-warrant to study the H_2 adsorption behaviors on fabricated quaternary B-C-N-O materials and to design novel optimized H_2 accumulators.

For physisorption-dominated adsorbents, textural properties of the materials play an important role in their H_2 uptake performances. A direct approach to achieving high H_2 uptake is to increase material specific surface area (SSA) and its micropore volume,[16] although the exact relationship between textural parameters and H_2 uptakes is yet clear. It is established that BNNTs reveal partial chemisorption at the high H_2 pressure and at room temperature, *i.e.* 10 MPa,[17] but the major adsorption mechanism of H_2 on BN or BCNO surfaces is a reversible physisorption at low temperature (77 K) and pressure.[18,19] As for the carbon systems, tuning pore width of the H_2 adsorbents was tentatively confirmed to be effective for improving sorption performances.[20-22] However, understanding of such correlations of textural parameters and H_2 sorption capacities for other physisorption-dominated materials is yet available. Several reports addressing the preparation of BCN(O) ternary or quaternary compounds for practical applications, such as phosphors [23,24] and lithium battery electrodes may be found.[25] Rather, there have

been seldom effective attempts toward fabricating high-surface-area porous BCN(O) structures with ultra-narrow pore widths used for gas sorption, especially in regards of H_2 storage. Only the BCNO products using a hard-template approach, that displayed the H_2 uptake of 1.07 wt % H_2 at 0.1 MPa and 77 K, is noticed in this respect.[19]

In this Chapter, I prepared highly porous BCNO adsorbents with the ultra-narrow and tunable pore widths, and also characterized the material textural properties and studied their H_2 adsorption behaviors in detail. The obtained products exhibit microbelt-like morphologies, partially disordered phases, high SSAs and pore volumes. They show enhanced H_2 uptakes of 1.90–2.14 wt % at 1 MPa and 1.41–1.60 wt % at a lower pressure of 0.1 MPa, better than those previously reported for any BCNO adsorbents.[19] The origin of the enhanced H_2 uptake is addressed, shedding the light on the importance of pore width for a design of efficient BCN(O) system-based H_2 adsorbents that may be used at a respectively low pressure range. (Note that the major results in this chapter have been published in *Chem. Asian J. 2013, 8, 2936*; *i.e.* Ref. 26)

4.2 Experimental methods

Synthesis procedure: The boric acid–melamine precursor was obtained by evaporating water from a boric acid and melamine (mol/mol=2:1) solution at ~100 ^{o}C. The white whisker-like precipitate was composed of boric acid and melamine molecules *via* hydrogen bond interactions.[27] The precursors were then loaded into a quartz tube with a 46 mm internal diameter and heated at 10 ^{o}C min^{-1} in an argon flow (0.5 L min^{-1}). The aimed synthesis temperatures were 900, 1100 and 1300 ^{o}C, and the reagents were maintained for 3 h before cooling to room temperature naturally. Previous studies have pointed out that water, CO_2, NH_3, and NH_2CN may be produced under decomposition of the 2B·M adducts under vacuum up to ~800 ^{o}C.[28] However, under the present synthetic conditions, C species could not be removed completely as was shown in *Ref. 26*. Dark brownish products were finally obtained and collected for the following structural, compositional, porosity and H_2 sorption characterizations without further treatments.

Structural characterization: The morphology observations were made out using a JSM-6700F SEM equipped with an EDS spectrometer and a 300 kV JEM-3000F HRTEM.

Quantitative elemental analysis method: The content of boron (B) was analyzed by ICP-OES method (IRIS advantage, Nippon Jarrell-Ash Co.). Carbon (C) content was measured in a carbon/sulfur determinator (CS-444LS, LECO Co.) using $CaCO_3$ as the standard substance, while nitrogen (N) and oxygen (O) contents were taken in an oxygen/nitrogen determinator (TC-436AR, LECO Co.) using Si_3N_4 and Y_2O_3 as the N and O standard substances.

Specific surface area and H_2 adsorption measurements: The N_2 and H_2 physisorption isotherms were taken at 77 K on a Quantachrome Autosorb-1 and BELSORP-HP-30 hydrogen adsorption set-up

independently (BEL Japan, Inc.) after sample outgassing at 150 ℃ over 24 h. Specific surface areas were computed by the Brunauer-Emmett-Teller (BET) equation using the relative pressure range of 0.02−0.08. NLDFT method was applied to calculate pore size distribution (PSD) and cumulative pore volumes. The H_2 isotherms were measured in a range of 0−1 MPa.

4.3 Structures and compositions of the materials

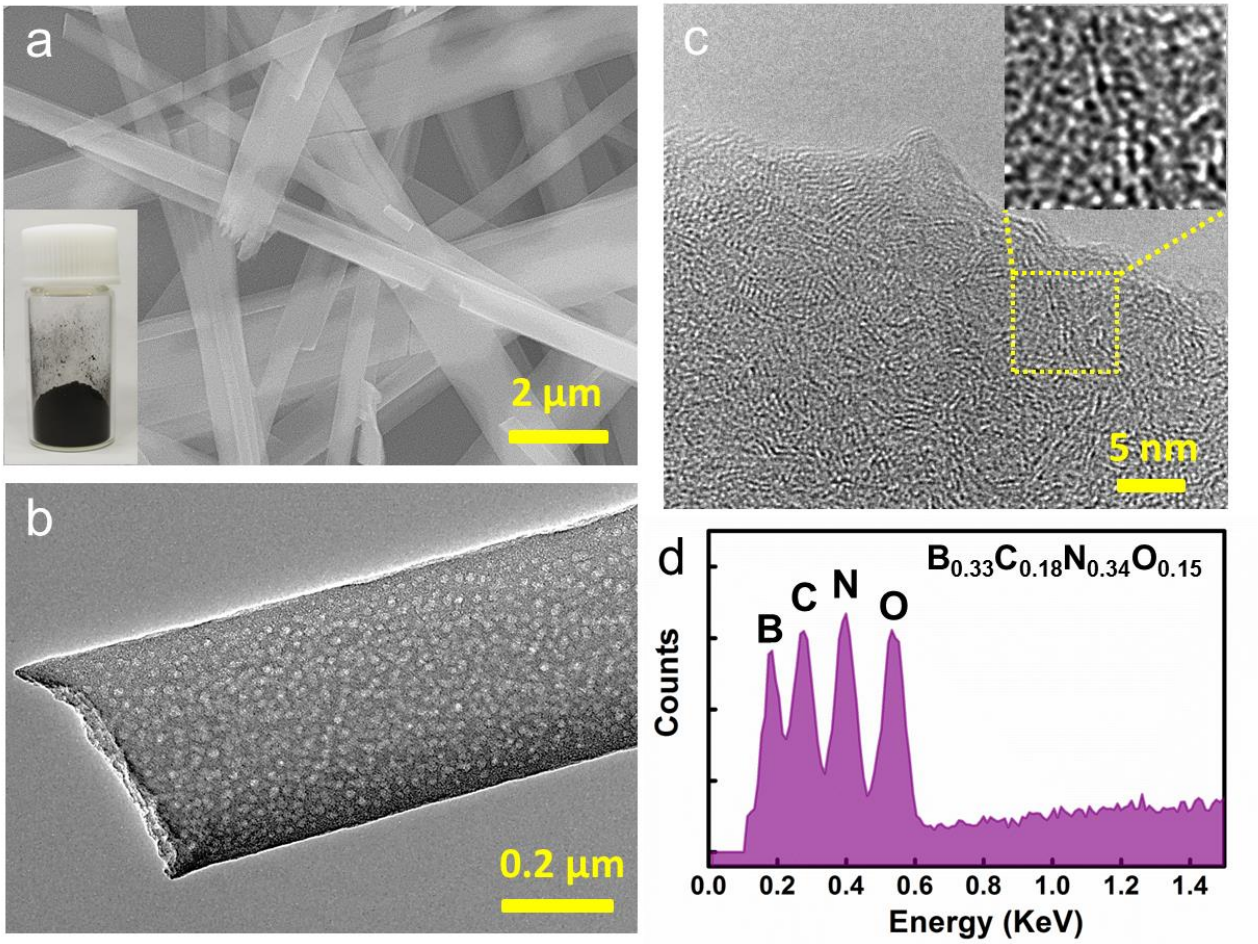

Figure 4.1 (a) SEM image of the BCNO numerous porous microbelts (BCNO-1100) prepared at 1100 °C. The inset displays a photograph of the as-prepared BCNO-1100 sample. (b) Low-magnification TEM image of a BCNO microbelt. (c) HRTEM image taken at the edge of the belt. The inset is the enlarged figure labelled in (c) after the low pass filtering. (d) Energy-Dispersive X-ray spectrum (EDS) of the BCNO-1100 sample. Quantitative chemical composition data given in (d) are calculated *via* the comprehensive analysis method. Reprinted from Ref. 26.

The one-step template-free approach previously discussed by me for making BN porous microbelts was utilized for the current synthesis of BCNO porous microbelts after modifications. In brief, while using argon as the protection atmosphere instead of C-reactive ammonia, the dark brownish BCNO porous samples

(Figure 4.1 (a)) were fabricated from the boric acid–melamine (2B·M) precursor at different T (900, 1100 and 1300 ^{o}C, named as BCNO-900, 1100 and 1300 samples, respectively) for 3 h. Their UV/Vis spectra reveal the strong absorptions in the whole spectrum of UV-visible range, as shown in section 6.10, Chapter 6. The yields were very high, up to 22–26 wt % with respect to the raw 2B·M precursors. All the BCNO products exhibit similar belt-like mophologies (Figure 4.1 and 4.2). For BCNO-1100, many randomly distributed pores were found on the belt surfaces in the corresponding low-magnification TEM images (*e.g.* Figure 4.2 (b)), implying a high porosity of the prepared quaternary microbelts. HRTEM analyses further reveal that the BCNO phase is partially disordered, resembling a turbostratic BN material[29,30] (*i.e.* an intermediate phase between the amorphous and ordered phases, Figure 4.1 (c)). So, the uniform and ultra-narrow micropores are created between or among the regarded partially disordered BCNO layers.

Table 4.1 Elemental compositions of BCNO porous microbelt samples

Samples	B (at %)	C (at %)	N (at %)	O (at %)
BCNO-900	34	13	35	18
BCNO-1100	33	18	34	15
BCNO-1300	40	12	34	13

Reprinted from Ref. 26.

As marked in Figure 4.1 (d), the qualitative chemical compositions of received new porous products were measured by Energy-Dispersive X-ray spectroscopy (EDX). A comprehensive and quantitative analysis further documents the chemical compositions for the samples as follows: 33–40 at % B, 12–18 at % C, 34–35 at % N, 13–18 at % O (Table 4.1).

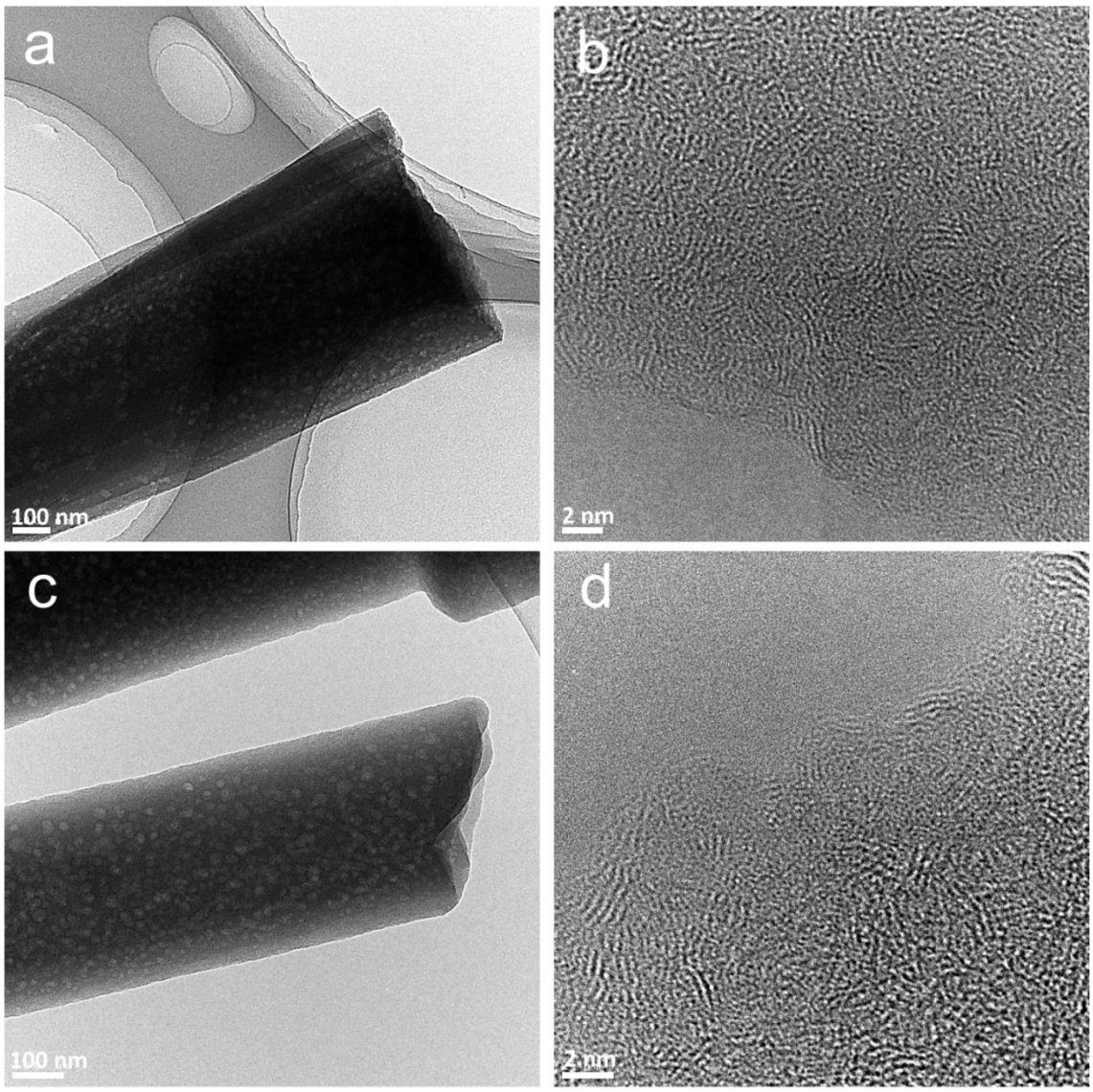

Figure 4.2 Low- and high-magnification TEM images of BCNO-900 (a,b) and BCNO-1300 (c,d) samples, respectively. Reprinted from Ref. 26.

4.4 XRD and XPS analysis

XRD patterns of the BCNO microbelt materials show two weak and broad diffraction bands corresponding to (0002) and (10-10) facets of a layered structure. (Figure 4.3) No other peaks were found in the XRD patterns, indicating the single-phase of the material. Thus, C and O atoms should be chemically "alloyed" into BN layers, which are still the backbones of the structural layered units. Unexpectedly, the total and/or local ordering of BCNO phases was not remarkably improved, even when they had been synthesized at temperature as high as 1300 ^{o}C, indicating a very high thermal stability of these BCNO strcutures.

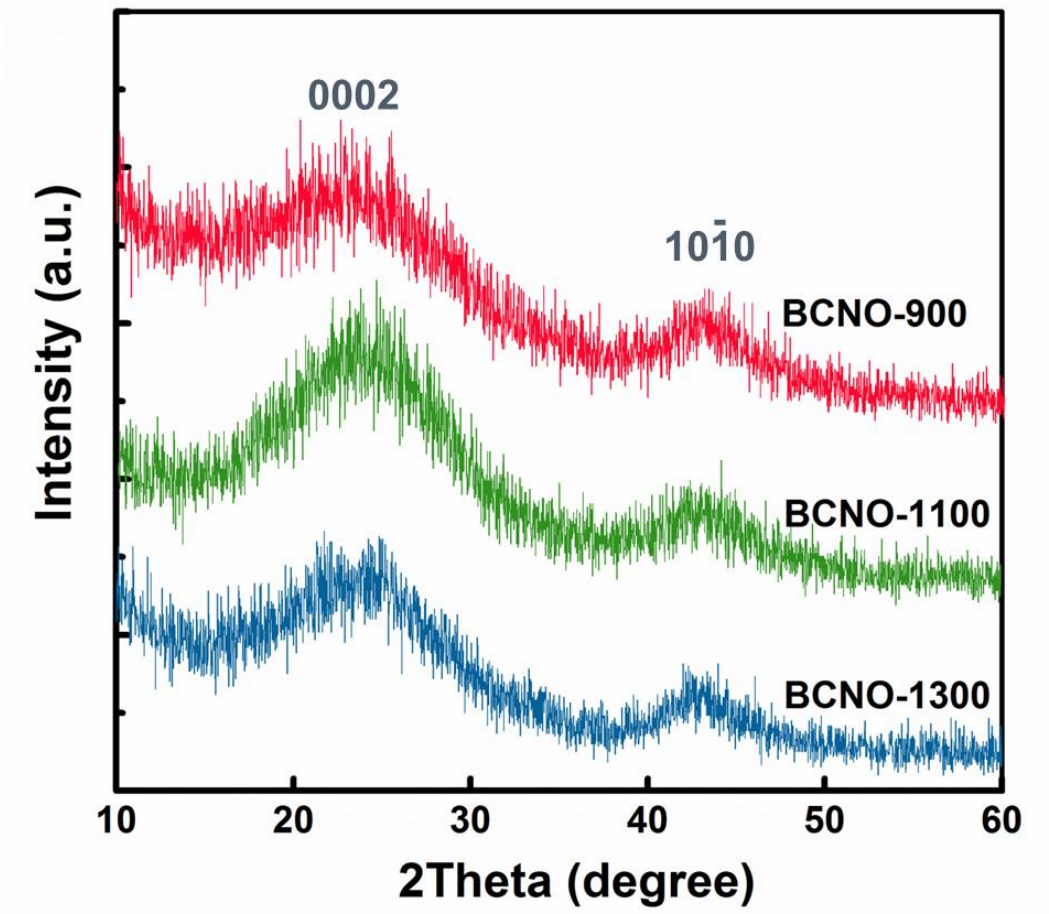

Figure 4.3 XRD patterns of the BCNO porous microbelts. Reprinted from Ref. 26.

As shown in Figure 4.4, B1s peak at 190.6 eV belongs to a B-N structure of the materials. The downshifts of B1s binding energies along with the rising synthetic temperatures are caused by an increased proportion of B−N units and a decrease of B−O (191.8 eV) units in the materials. From C1s, N1s and O1s spectra, the chemical states of C, N and O in the material show no obvious changes. A slight shift toward lower binding energy in the N1s spectra along with the rising synthetic temperatures is arisen from an increase of B−N domains (398.1 eV) accompanied with a decrease of C-N units (~399 eV). These XPS results also confirm that the basic framework for these quaternary materials is a B-C-N network, and O is mainly bonded to the B sites.

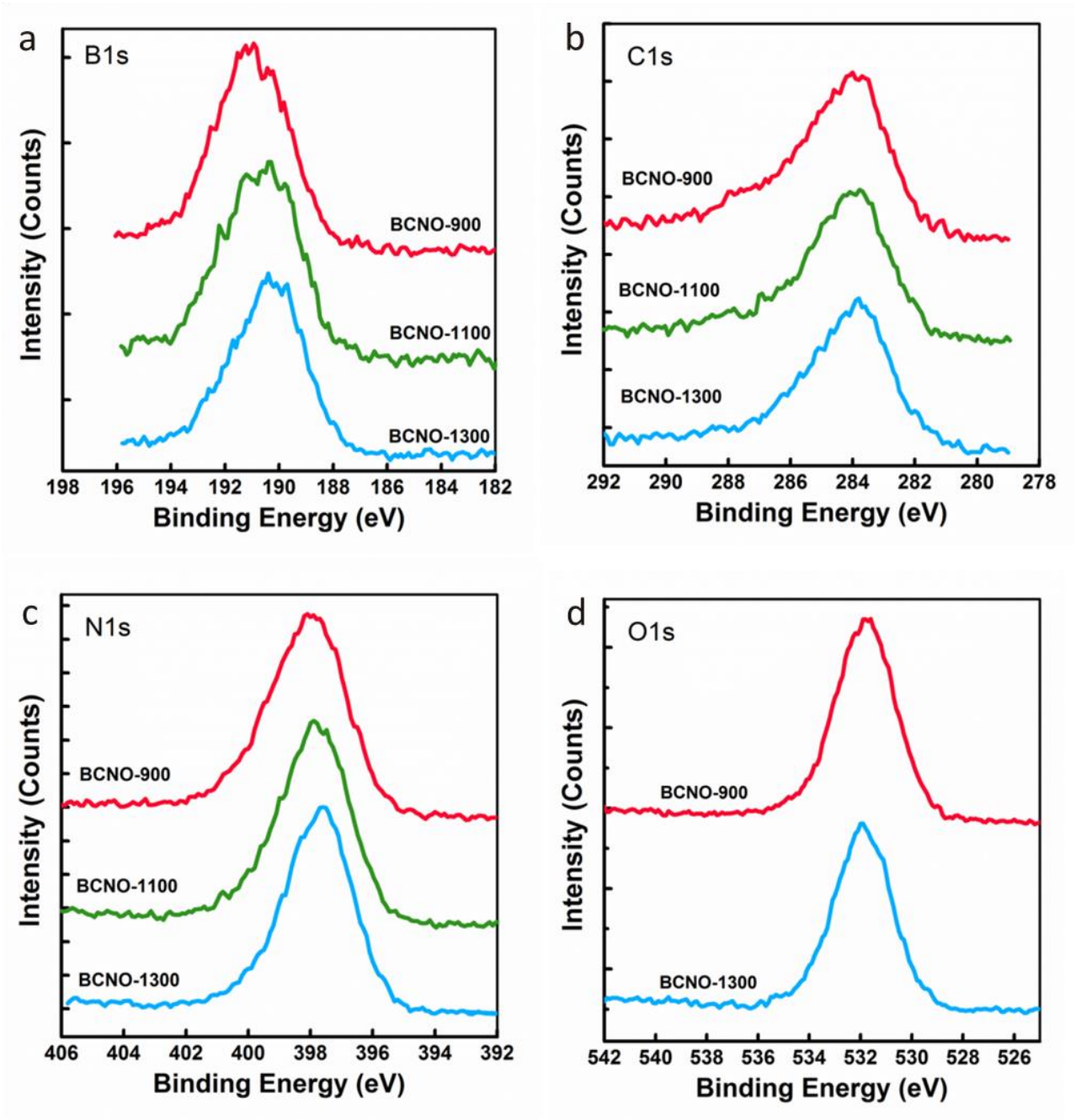

Figure 4.4 XPS B1s (a), C1s (b), N1s (c) and O1s (d) spectra for the BCNO microbelts. Reprinted from Ref. 26.

4.5 Porosity of the BCNO mircobelts

The porosity and SSAs of BCNO microbelts were determined by N_2 adsorption and desorption methods. For all samples, dramatic increases of N_2 adsorption are seen at a low relative pressure range of $P/P_0 < 0.01$, implying the micropore presence. Their hysteresis loops and isotherms are analogs of H4

and I types. Notable downsteps that appear at a respective pressure of P/P_0=0.45 in the desorption branches are due to cavitation caused by abrupt evaporation of liquid N_2 from the pore ink-bottle-like structures.[31] The calculated BET SSAs for these BCNO samples (from BCNO-900 to BCNO-1300) are 1070, 1040 and 1040 m^2 g^{-1}, with the total pore volume values of 0.575, 0.611 and 0.587 cm^3 g^{-1}, respectively, implying that the textural values of the materials derived from different synthetic temperatures are very close (Figure 4.5 and Table 4.2). As confirmed by their pore size distribution (PSD) profiles computed using a nonlocal density functional theory (NLDFT),[32] all the BCNO microbelt samples exhibit high and close microporosity (0.385, 0.354 and 0.368 cm^3 g^{-1}). However, their corresponding pore widths change drastically with the increase of the synthesis temperatures; BCNO-900 and BCNO-1100 samples show very sharp peaks at 0.4 and 0.6 nm, respectively, whereas BCNO-1300 starts to display an even and broad pore distribution at 0.4-1.1 nm. Therefore, the present porous BCNO products may serve as an ideal model for the study of pore width effect on H_2 adsorptions, which have excluded many other factors that may also influence H_2 sorption behaviors, *e.g.* SSAs, pore volumes, chemical compositions, *etc*.

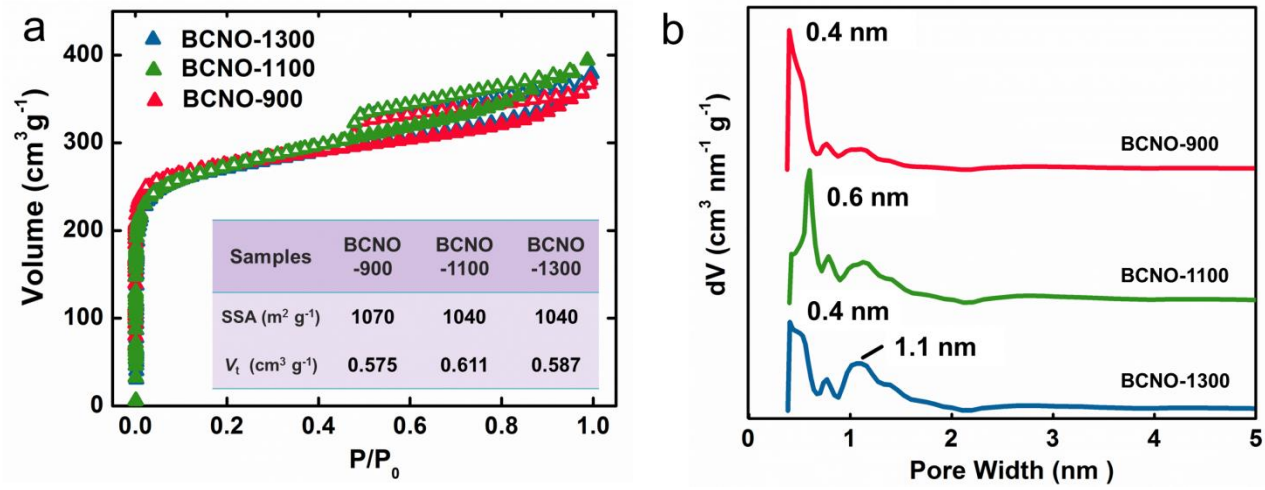

Figure 4.5 (a) Nitrogen adsorption-desorption isotherms of the BCNO microbelt samples (77 K). The table inset in (a) summarizes the BET SSAs and total pore volumes (P/P_0 = 0.99). (b) Pore size distribution (PSD) profiles of BCNO microbelts calculated by nonlocal Density Functional Theory (NLDFT). Reprinted from Ref. 26.

Table 4.2 Textural characteristics of the microbelt samples.

	BET SSA (m^2 g^{-1})	Langmuir SSA (m^2 g^{-1})	Total pore volume (cm^3 g^{-1})[a]	Micropore volume (<1 nm) (cm^3 g^{-1})[b]	Micropore volume (cm^3 g^{-1})[b]	Meso + macro pore volume (cm^3 g^{-1})[c]	Micropore width (nm)[b]
BCNO-900	1070	1020	0.575	0.311	0.385	0.190	0.4
BCNO-1100	1040	1110	0.611	0.231	0.354	0.257	0.6
BCNO-1300	1040	908	0.587	0.217	0.368	0.219	0.4, 1.1

[a]The total pore volume is calculated at a relative pressure of 0.99. [b]The micropore volume and width are computed via NLDFT method applied to nitrogen adsorption isotherm. [c]Meso- and macropore volumes are calculated through subtraction of the micropore volume from the total pore volume. Reprinted from Ref. 26.

4.6 Hydrogen sorption behaviors for the BCNO materials

The H_2 adsorption and desorption isotherms for the BCNO samples measured at 77 K and 0–1 MPa are illustrated in Figure 4.6. The BCNO-1100 exhibits a high and close H_2 excess uptakes of 2.14 wt % comparable to that of BCNO-1300 sample at 1 MPa (2.12 wt %). However, the former product reveals clearly higher capacities at a lower pressure range of 0–1 MPa, implying the higher efficiency of the narrower pores for H_2 uptakes. And interestingly, although the pore width of BCNO-900 (0.4 nm) is narrower than for other two BCNO samples, the corresponding H_2 uptake capacity in the pressure range of 0.45–1 MPa is remarkably lower than those of BCNO-1100 and BCNO-1300. Only at a very low pressure range (<50 kPa), the H_2 uptake capacity shows an inverse correlation with the pore widths.

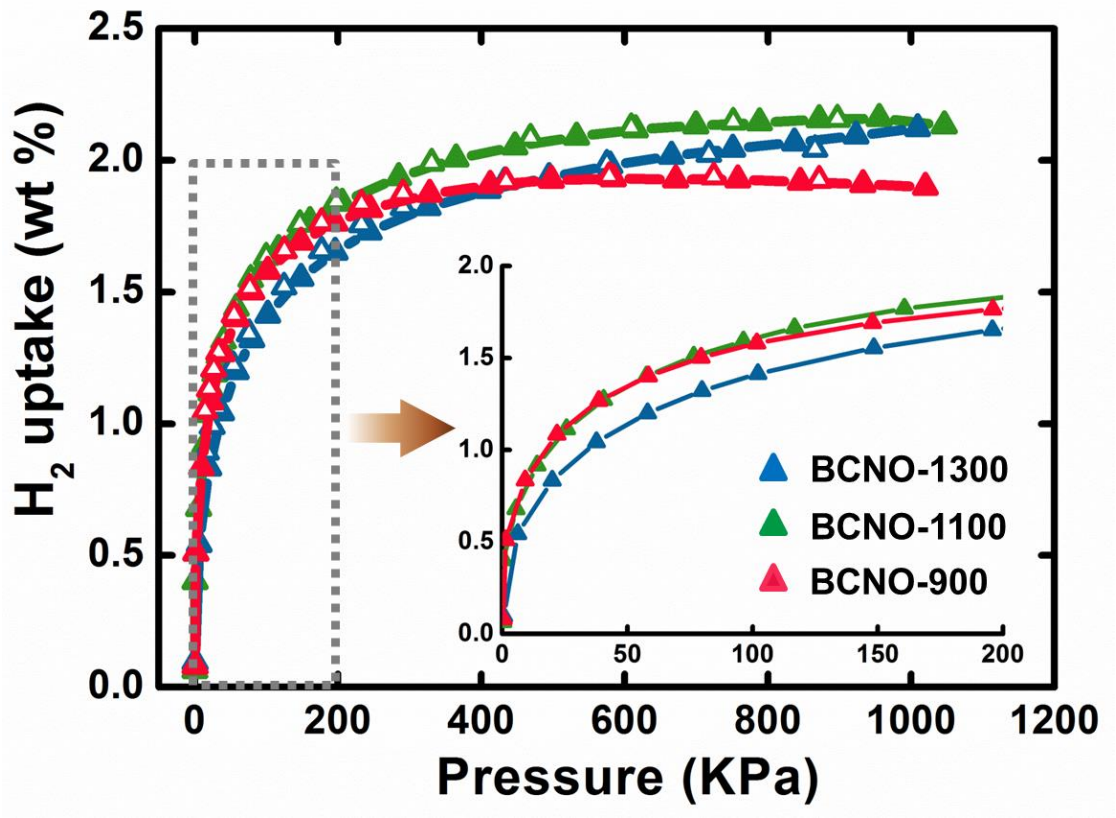

Figure 4.6 Hydrogen adsorption-desorption isotherms of the BCNO porous microbelt samples taken at 77 K and 0–1 MPa. Reprinted from Ref. 26.

Analogous correlation of the pore width and H_2 uptakes, *i.e.*, narrower pore which favors a higher H_2 uptake, was observed in porous carbons.[20,21] Based on the H_2 sorption behaviors for the materials, we conclude that ultra-narrow pores (0.4 and 0.6 nm) are more efficient than the larger micropores (1.1 nm) for H_2 uptakes at the low pressure range in the present porous BCNO system. However, the latter micropores are indeed still effective for H_2 storage at a raised pressure of ~1 MPa, which is still acceptable in practical applications. A surface made of more B-N units instead of B-O and C-N units is beneficial to enhance the interactions between H_2 and the material surface.[19] This phenomenon also explains the observed data of higher H_2 uptakes for the BCNO-1100 and BCNO-1300 samples at elevated pressures. It is noticed that the H_2 uptakes of all BCNO porous microbelts evidenced in this work (1.41–1.60 wt %) are better than for the porous BCNO sample prepared *via* a hard-template method ($B_{0.36}C_{0.12}N_{0.32}O_{0.11}H_{0.09}$, 1.07 wt % H_2 uptake at 77 K and 0.1 MPa).[19] This is because the main pore widths of the regarded hard-template-derived porous BCNO materials were between 6 and 8 nm, which are too spacious to adsorb H_2 molecules effectively, despite of their higher SSAs and nearly identical chemical compositions.

4.7 Summary

As a summary, I have successfully synthesized a series of quaternary BCNO porous microbelts. They are featured by similar morphologies and chemical compositions, and partially disordered phases. Furthermore, they show high and close SSAs, and pore volumes (including micropore and macropore volumes), but peculiar ultra-narrow pore widths varied from 0.4 to 1.1 nm. These thorough studies of the correlation between the pore width and H_2 storage performance of a material allows me to draw the following conclusions for the present material system: 1) a narrower pore width favors a higher H_2 uptake at a low pressure range of 0–50 kPa; 2) the micropores with a pore width up to 1.1 nm are still effective for H_2 uptakes at a pressure of ~1 MPa and 77 K. Thus, increasing the volume for pores having a width below 1 nm is envisaged be an efficient way to improve the H_2 storage ability of porous BCNO materials.

4.8 References

1 Kroto, H. W.; Heath, J. R.; O'Brien, S. C.; Curl, R. F.; Smalley, R. E. *Nature* **1985**, *318*, 162.

2 Stéphan, O; Bando, Y.; Loiseau, A.; Willaime, F.; Shramchenko, N.; Tamiya, T.; Sato, T. *Appl. Phys. A: Mater. Sci. Process.* **1998**, *67*, 107.

3 Golberg, D.; Bando, Y.; Stéphan, O.; Kurashima, K. *Appl. Phys. Lett.* **1998**, *73*, 2441.

4 Iijima, S. *Nature* **1991**, *354*, 56.

5 Chopra, N. G.; Luyken, R. J.; Cherrey, K.; Crespi, V. H.; Cohen, M. L.; Louie, S. G.; Zettl, A. *Science* **1995**, *269*, 966.

6 Novoselov, K. S.; Geim, A. K.; Morozov, S. V.; Jiang, D.; Zhang, Y.; Dubonos, S. V.; Grigorieva, I. V.; Firsov, A. A. *Science* **2004**, *306*, 666.

7 Golberg, D.; Bando, Y.; Huang, Y.; Terao, T.; Mitome, M.; Tang, C.; Zhi, C. *ACS Nano* **2010**, *4*, 2979.

8 Balandin, A. A. *Nat. Mater.* **2011**, *10*, 569.

9 Tijerina, J. T.; Narayanan, T. N.; Gao, G.; Rohde, M.; Tsentalovich, D. A.; Pasquali, M.; Ajayan, P. M. *ACS Nano* **2012**, *6*, 1214.

10 Golberg, D.; Bando, Y.; Kurashima, K.; Sato, T. *Scr. Mater.* **2001**, *44*, 1561.

11 Chen, Y.; Zou, J.; Campbell, S. J.; Caer, G. L. *Appl. Phys. Lett.* **2004**, *84*, 2430.

12 Lee, C. H.; Xie, M.; Kayastha, V.; Wang, J. S.; Yap, Y. K. *Chem. Mater.* **2010**, *22*, 1782.

13 Song, L.; Ci, L.; Lu, H.; Sorokin, P. B.; Jin, C.; Ni, J.; Kvashnin, A. G.; Kvashnin, D. G.; Lou, J.; Yakobson, B. I.; Ajayan, P. M. *Nano Lett.* **2010**, *10*, 3209.

14 Jhi, S. H.; Kwon, Y. K. *Phys. Rev. B* **2004**, *69*, 245407.

15 Aboutalebi, S. H.; Aminorroaya-Yamini, S.; Nevirkovets, I.; Konstantinov, K.; Liu, H. K. *Adv. Energy Mater.* **2012**, *2*, 1439.

16 Yang, S. J.; Kim, T.; Im, J. H.; Kim, Y. S.; Lee, K.; Jung, H.; Park, C. R. *Chem. Mater.* **2012**, *24*, 464.

17 Ma, R. Z.; Bando, Y.; Zhu, H. W.; Sato, T.; Xu, C. L.; Wu, D. H. *J. Am. Chem. Soc.* **2002**, *124*, 7672.

18 Weng, Q. H.; Wang, X. B.; Zhi, C. Y.; Bando, Y.; Golberg, D. *ACS Nano*, **2013**, *7*, 1558.

19 Portehault, D.; Giordano, C.; Gervais, C.; Senkovska, I.; Kaskel, S.; Sanchez, C.; Antonietti, M. *Adv. Funct. Mater.* **2010**, *20*, 1827.

20 Gogotsi, Y.; Dash, R. K.; Yushin, G.; Yildirim, T.; Laudisio, G.; Fischer, J. E. *J. Am. Chem. Soc.* **2005**, *127*, 16006.

21 Yang, Z.; Xia, Y.; Mokaya, R. *J. Am. Chem. Soc.* **2007**, *129*, 1673.

22 Masika, E.; Mokaya, R. *J. Phys. Chem. C* **2012**, *116*, 25734.

23 Ogi, T.; Kaihatsu, Y.; Iskandar, F.; Wang, W. N.; Okuyama, K. *Adv. Mater.* **2008**, *20*, 3235.

24 Lei, W. W.; Portehault, D.; Dimova, R.; Antonietti, M. *J. Am. Chem. Soc.* **2011**, *133*, 7121.

25 Lei, W. W.; Qin, S.; Liu, D.; Portehault, D.; Liu, Z. W.; Chen, Y. *Chem. Commun.* **2013**, *49*, 352.

26 Weng, Q. H.; Wang, X. B.; Wang, X.; Liu, D. Q.; Jiang, X. F.; Zhi, C. Y.; Bando, Y.; Golberg, D. *Chem. Asian J.* **2013**, *8*, 2936–2939.

27 Roy, A.; Choudhury, A.; Rao, C. N. R. *J. Mol. Struct.* **2002**, *613*, 61-66.

28 Hagio, T.; Kobayashi, K.; Sato, T. *J. Ceram. Soc. Jpn* **1994**, *102*, 1051–1054.

29 Thomas, J.; Weston, N. W.; O'Connor, T. E. *J. Am. Chem. Soc.* **1963**, *84*, 4619;

30 Hamilton, E. J. M.; Dolan, S. E.; Mann, C. M.; Colijn, H. O.; Shore, S. G. *Chem. Mater.* **1995**, *7*, 111.

31 Neimark, A. V.; Lin, Y.; Ravikovitch, P. I.; Thommes, M. *Carbon* **2009**, *47*, 1617.

32 Evans, R.; Tarazona, P. *Phys. Rev. Lett.* **1984**, *52*, 557.

Chapter 5

Summary and outlook

Chapter 5. Summary and outlook

5.1 Summary

In this Thesis, a variety of porous BN materials with different porosity and composition characteristics were successfully fabricated. The developed novel one-step and template-free preparation method was found to be effective to obtain highly porous BNs compared with previously reported template-directing methods. Correlations between material textural parameters and H_2 uptake capacities were also carefully studied and discussed.

In Chapter 2, I proposed a simple route toward hierarchically porous BN materials applyingg a one-step, template-free reaction within a boron acid–melamine precursor in ammonia atmosphere under moderate conditions. The phase of fabricated porous belt-like products was partially disordered, and exhibited a widen spacing between the adjacent (0002) layers, thus belonging to an intermediate state between hexagonal and amorphous BN phases. The porous BN sample synthesized at 1000 °C showed the largest specific surface area (SSA) and a high micropore volume among all samples, featuring the values of 1488 $m^2\ g^{-1}$ and 0.502 $cm^3\ g^{-1}$, respectively, whereas the 1100 °C-derived sample exhibited the largest total pore volume of 0.880 $cm^3\ g^{-1}$. H_2 uptake measurements carried out at 77 K and 1 MPa confirmed that the latter sample possessed the largest reversible H_2 uptake capacity of 2.3 wt %.

In Chapter 3, I described the successful synthesis of highly porous sponge-like BN materials through a simple, one-step, template-free method under ambient conditions. These porous BN materials were characterized by their dominated pore sizes of 1.0 nm, suggesting they were mainly microporous. Structural characterizations revealed the enlarged (0002) spacings, partially disordered BN phase and the presence of mumerous dislocations in these materials. A proper N precursor/boric acid ratio and a moderate synthesis temperature were found to be necessary to obtain the BN microsponge samples with the optimized SSA (up to 1900 $m^2\ g^{-1}$), porosity (1.070 $cm^3\ g^{-1}$), and H_2 uptake (2.57 wt%, at –196 °C and 1 MPa).

In Chapter 4, partially disordered BCNO porous microbelts with similar morphologies and chemical compositions were prepared. They exhibited high and close SSAs, pore volumes (including micropore and macropore volumes), but distinct ultra-narrow pore widths which varied in the range from 0.4 to 1.1 nm. A narrower pore width favors a higher H_2 uptake at a low pressure range, while the micropores with the pore width up to 1.1 nm are found to be still effective for H_2 uptake at a pressure of ~1 MPa and 77 K. Furthermore, the surface chemical environment was also found to influence the final H_2 uptakes.

Overall, the achieved results included in this Thesis are envisaged to promote timely-warrant top-notch studies on porous BN and to lift them to a new level. For instance, the SSA of the BN materials was raised in

my PhD work to a value of 1900 $m^2 g^{-1}$, twice of the best reported results before my project has been started. And importantly, this was also the first systematic study on the correlations between BNs textural properties and their H_2 sorption capacity.

5.2 Outlook

Though obvious progress has been achieved, there are still many works need to be done to realize the practical goal of using porous BN for H_2 storage. In this section, I would like to finally express my own view of the future developments in this field.

5.2.1 Develop the method to increase the SSA and pore volume of BN enormously

To date, the highest reported SSA for BN materials are still around 2000 $m^2 g^{-1}$. This value is still far below the cutting-edge SSA values reported for porous carbons and MOFs. Thus, due to the fundamental role of SSA and pore volume on H_2 uptake performance for a physisorption-based material, the direct way to further improve the H_2 sorption capacity of BN materials is increasing their SSAs and pore volumes.

There are several theoretical BN models (Figure 5.1) that have been proposed in the recent two years by Zeng's group.[1,2] Normal sp^2-hybridized BN domains are linked by sp^3-BN chains. They are not only mechanically and thermal stable, but also have SSAs up to 4800 $m^2 g^{-1}$. Furthermore, the computed hydrogen adsorption energy (-0.18 eV, *i.e.* -17.3 kJ mol^{-1}) is very close to the optimal adsorption energy (-0.15 eV), thus it is highly favourable for a reversible hydrogen storage at room temperature. This work indicates that porous BNs are good candidates as a H_2 accumulator, and pursuing the porous BNs with higher SSAs and pore volumes is a practical way to find final porous BN products that can satisfy DOE's requirements.

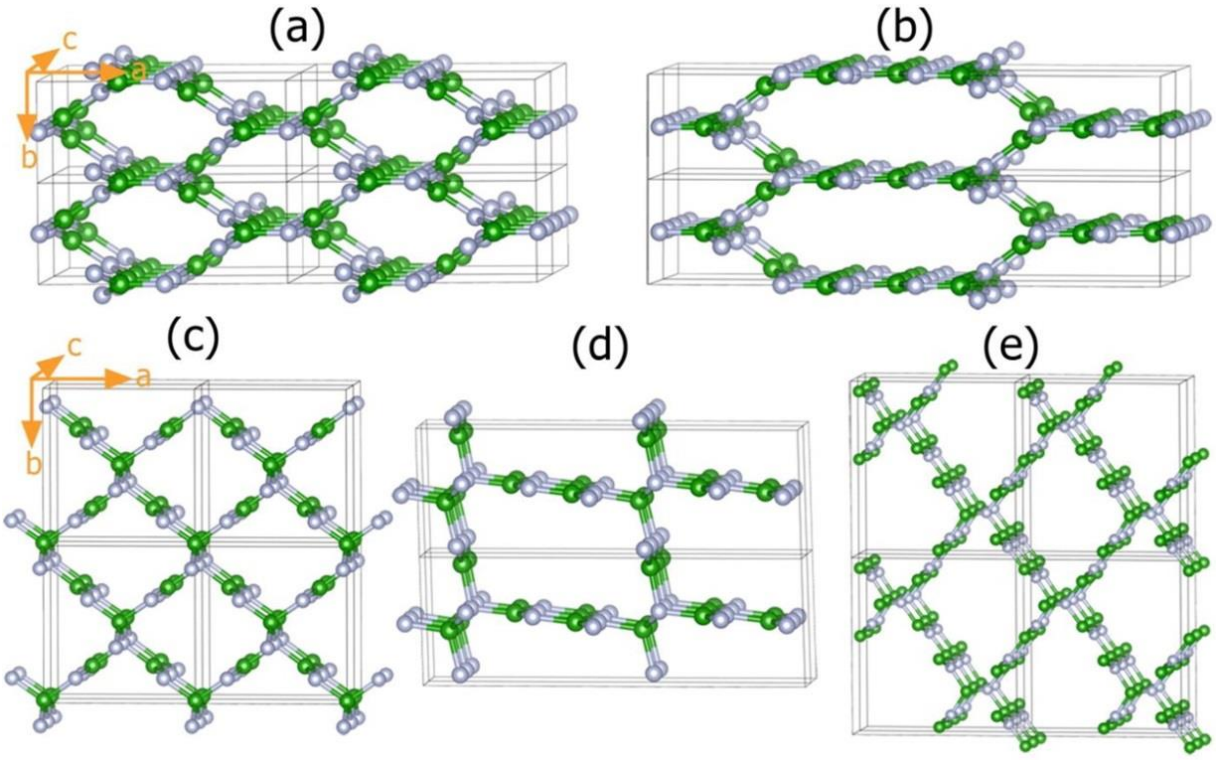

Figure 5.1 Theoretically predicted stable porous BN structures. The SSAs (m^2 g^{-1}) for the models are ~4800 (a), ~3800 (b), ~3700 (c), ~3400 (d) and ~3300 (e). Reproduced from Ref. 1.

5.2.2 To understand the role of surface chemistry of BN on H_2 sorption

My work in Chapter 4 has preliminary showed the potential importance of the adsorbent surface environment on the H_2 sorption capacity. Indeed, the affinity between H_2 molecules and the material surface can be tuned by modifying its surface composition.

Several theoretical works performed by Xue *et al.* have confirmed this point.[3,4] They explored Li and Ca-decorated carbon-doped BN monolayers (BC_2N) for H_2 storage. The BC_2N–Li complexes may serve as high-capacity hydrogen-storage media with gravimetric hydrogen capacity of 9.94 wt % at ambient conditions, which can desorb H_2 molecules at c.a. 373 K and at a pressure of 1.5 atm. These conditions are desirable for practical applications, see Figure 5.2.

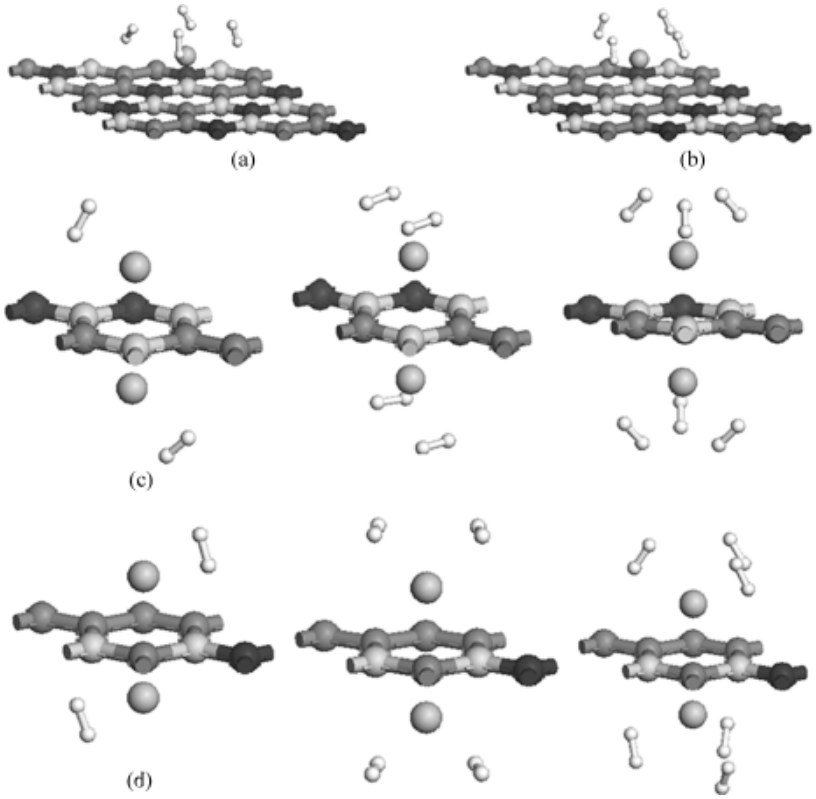

Figure 5.2 (a,b) Optimized structures of adsorption of four H_2 molecules on a single side of two Li-decorated BC_2N monolayers. (c,d) Optimized structures of two Li atoms adsorbed at two BC_2N monolayers with one to three adsorbed H2 molecules around each Li atom. Reproduced from Ref. 3.

Experimentally, Lei *et al.* found that 4 at % oxygen-doped BN sheets with a SSA of 536 $m^2\ g^{-1}$ has shown a H_2 storage capacity of 5.7 wt % under 5 MPa at room temperature. ~89 % of the stored hydrogen was released when the hydrogen pressure had been reduced to ambient conditions.[5] This is a relatively high value with respect to its SSA, which may be explained by the modified BN surface.

Though researches on this aspect have just been initiated, one can expect the prosperous future of this direction due to the infinite possibilities on BN surface modifications and functionalizations.

5.2.3 To explore BN-based hybrid materials for H_2 storage

Other H_2 storage materials, especially those relied on chemisorption, can be incorporated into a porous BN matrix to make a hybrid for advanced H_2 storage. Mg, Pd, $LaNi_5$, Li_3N *etc.*, if structured down to the nanoscale, can improve the kinetic behaviors remarkably. Porous BNs themselves are very stable, and can stabilize the nanoparticles mentioned above to form novel hybrids. Such hybrids can adsorb H_2 both physically and chemically, and may pave a new way toward a smart design of future H_2 storage materials.

5.3 Refereces

1 Dai, J.; Wu, X.; Yang, J.; Zeng, X. C. *J. Phy. Chem. Lett.* **2014**, *5*, 393–398.

2 Dai, J.; Wu, X.; Yang, J.; Zeng, X. C. *J. Phy. Chem. Lett.* **2013**, *4*, 3484–3488

3 Qiu, N. X.; Zhang, C. H.; Xue, Y. *ChemPhysChem*, **2014**, *15*, 3015–3025.

4 Qiu, N. X.; Tian, Z.; Guo, Y.; Zhang, C.; Luo, Y.; Xue, Y. *Int. J. Hydrogen Energy* **2014**, *39*, 9307–9320.

5 Lei, W.; Zhang, H.; Wu, Y.; Zhang, B.; Liu, D.; Qin, S.; Liu, Z.; Liu, L.; Ma, Y.; Chen, Y. *Nano Energy* **2014**, *6*, 219–224.

Chapter 6

Appendix

Chapter 6. Appendix

Additional Figures and data are provided in this Chapter to support the results in Chapter 2-4.

6.1 Structures of BN microrods, loosen belt bundles and isolated microbelts

The as-prepared products after heating contain BN microrods, as shown in Figure 6.1 (a). They are composed of aligned BN porous belts, which become loosen and isolated after supersonic exfoliation (Figure 6.1 (b,c)).

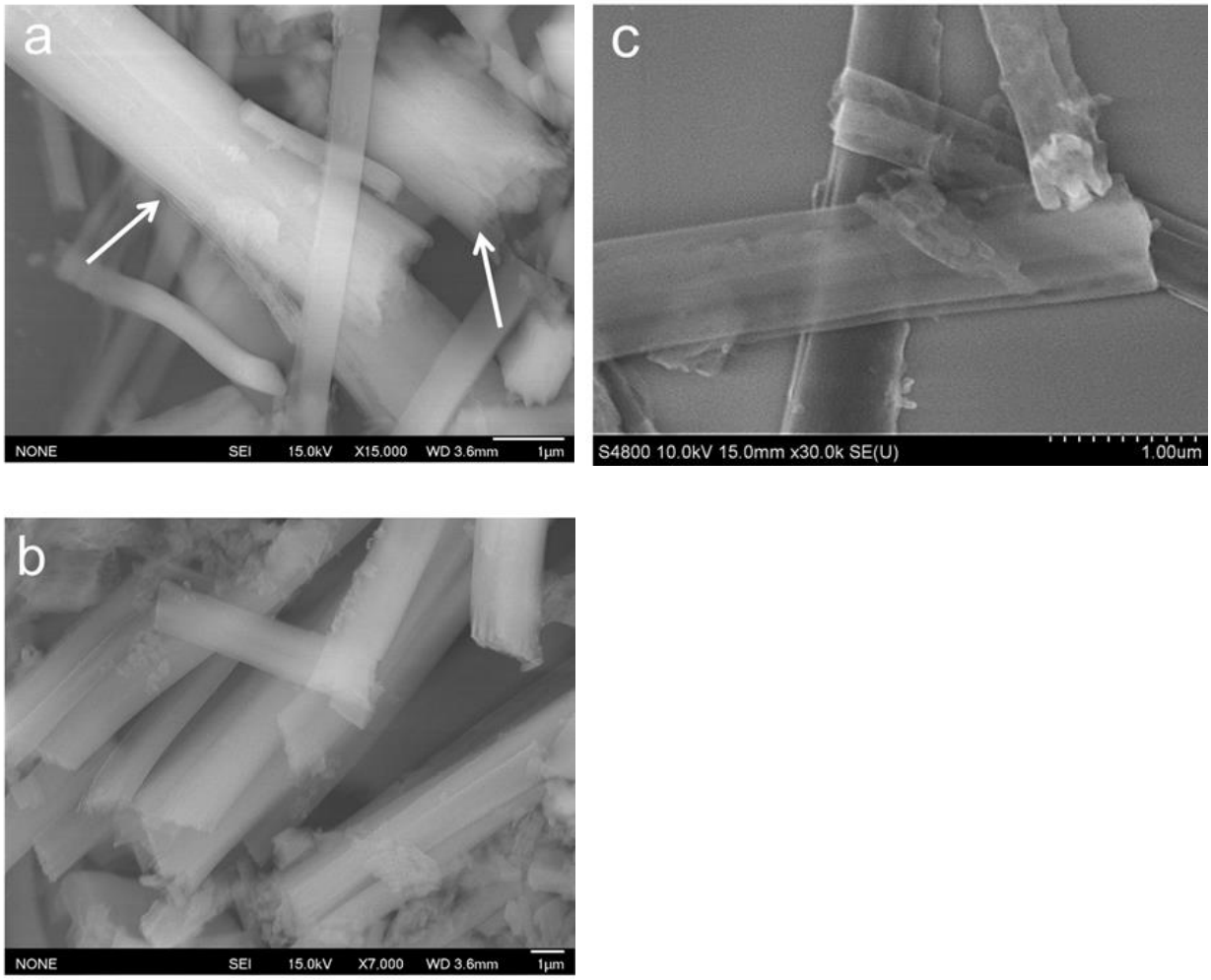

Figure 6.1 SEM images of as-prepared BN porous microbelt and microrod mixtures (a), loosen belt bundles (b) and isolated microbelts (c). White arrows drawn in (a) indicate microrod structures. Reproduced from Ref. 23, Chapter 2.

6.2 Morphologies of the BNPBs prepared from 4B•M and B•M precursors

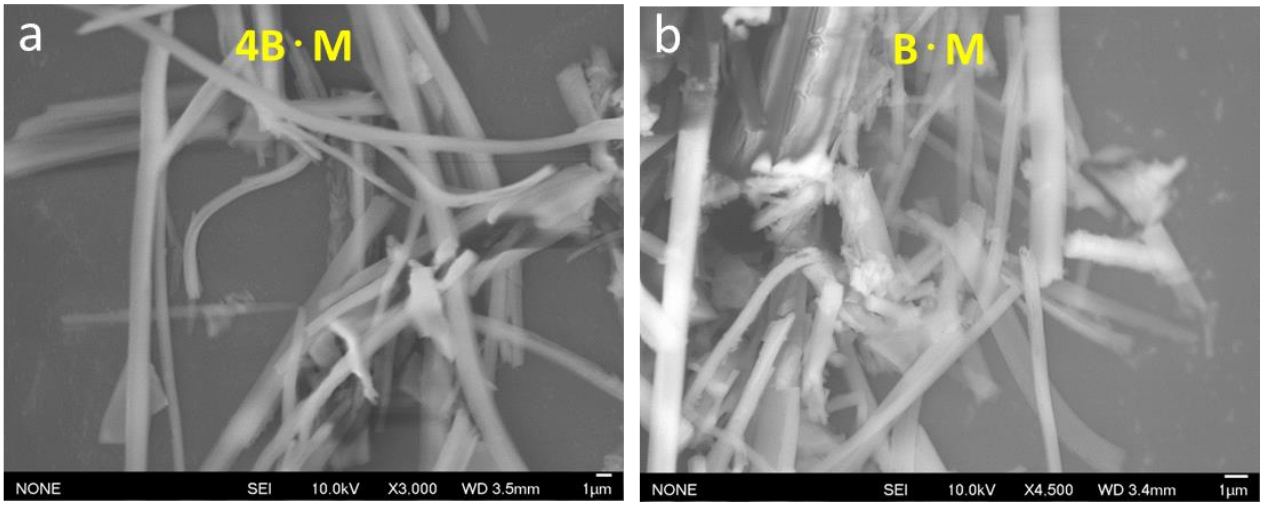

Figure 6.2 SEM images of the BNPS samples obtained from 4B•M (a) and B•M (b) precursors at 1100 ^{o}C for 3 h. Reproduced from Ref. 23, Chapter 2.

6.3 Morphologies of BNPB-900 and BNPB-1000

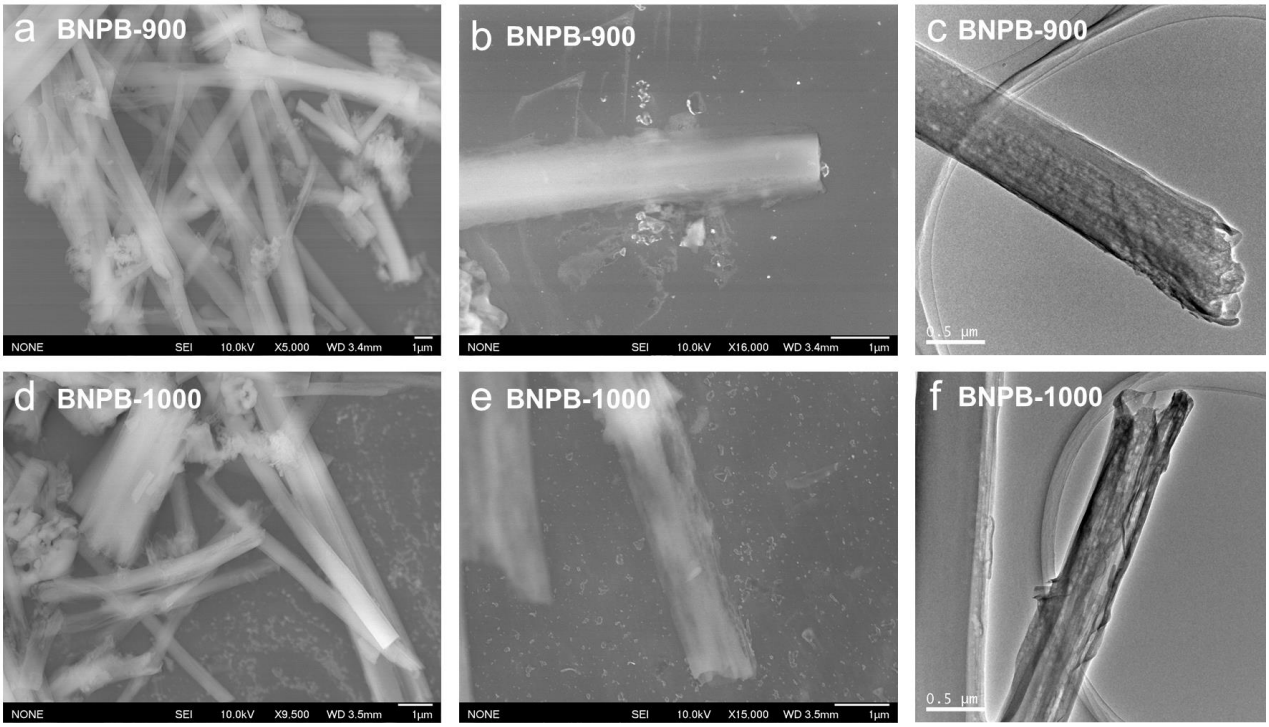

Figure 6.3 (a,b) SEM images of BN porous microbelts synthesized at 900 ^{o}C (BNPB-900). (c) Low-magnification TEM image of a BNPB-900 section. (d,e) SEM images of BN porous microbelts synthesized at 1000 ^{o}C (BNPB-1000). (f) Low-magnification TEM image of a BNPB-1000 section. Reproduced from Ref. 23, Chapter 2.

6.4 Table 6.1. List of Raman shifts (E_{2g} mode) recorded from different isolated microbelts for each sample

	1	2	3	Average shifts (cm^{-1})
BNPB-900	1376.17	1376.47	1375.82	1376.15
BNPB-1000	1373.10	1373.12	1373.02	1373.08
BNPB-1100	1373.11	1373.14	1373.15	1373.13
After annealing [a]	1370.39	1370.49		1370.44

[a]Annealing treatment of BNPB-1100 was carried out at 1500 ^{o}C for 5h. Reproduced from Ref. 23, Chapter 2. Reproduced from Ref. 23, Chapter 2.

6.5 Chemical compositions of BNPB-900 and BNPB-1000 samples

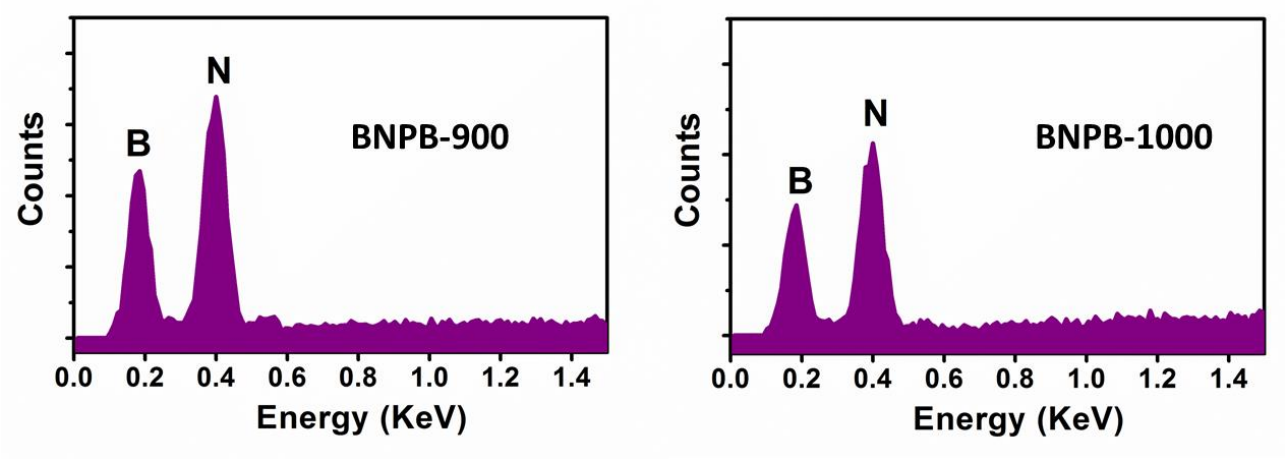

Figure 6.4 (a,b) EDX spectra of BNPB-900 and BNPB-1000 specimens. Reproduced from Ref. 23, Chapter 2.

6.6 Hydrogen uptake of the BNPBs prepared from 4B•M and B•M precursors

The H_2 uptake capacity of the BNPB derived from B•M shows very close values compared to BNPB-1100 prepared from 2B•M precursor. *E.g.*, both of them exhibit 2.3 wt % capacity at 1 MPa and 77 K. As we have confirmed that the B•M adduct shows a ~45 % weight loss at 200-300 ^{o}C caused by melamine sublimation, using the excess melamine can not further improve the H_2 storage performance of the products. On the other hand, using excess boric acid results in a lower H_2 capacity of the BNPB sample at the same testing conditions.

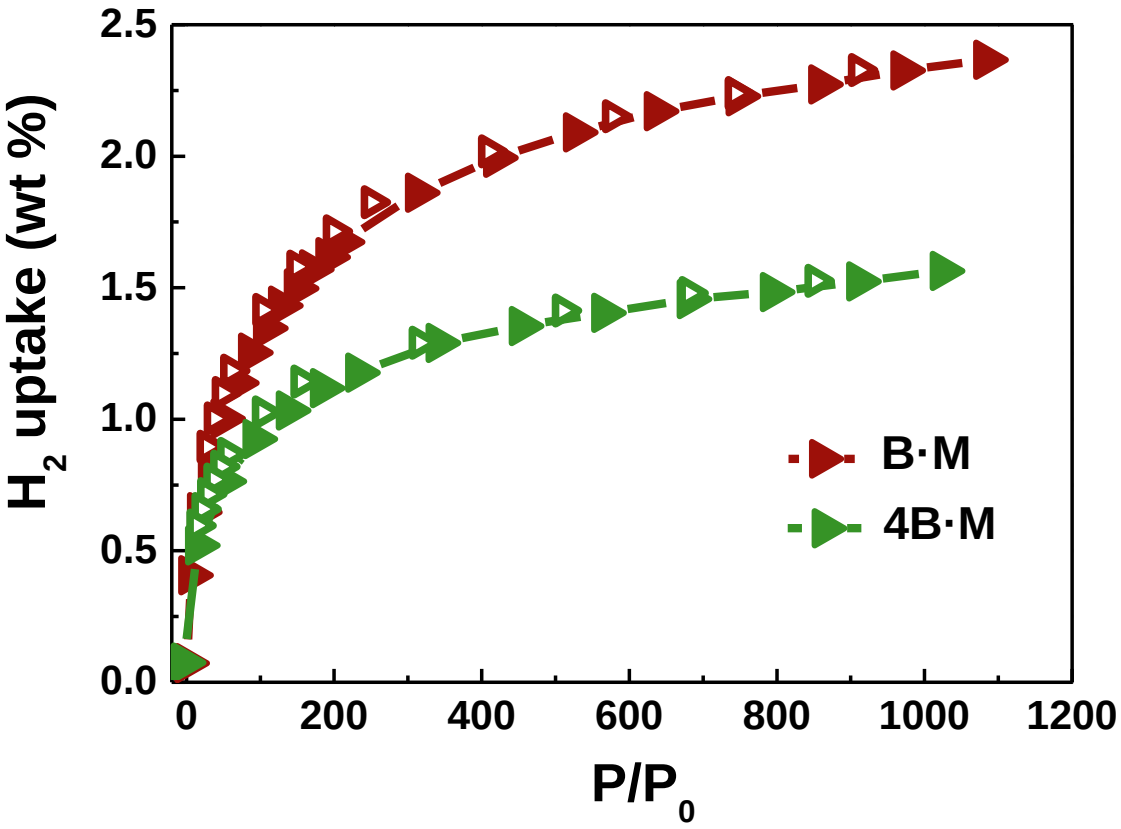

Figure 6.5 H_2 adsorption and desorption isotherms at 77 K of the BNPS samples obtained from 4B•M and B•M precursors at 1100 ^{o}C for 3 h.

6.7 XRD patterns of BNMS samples

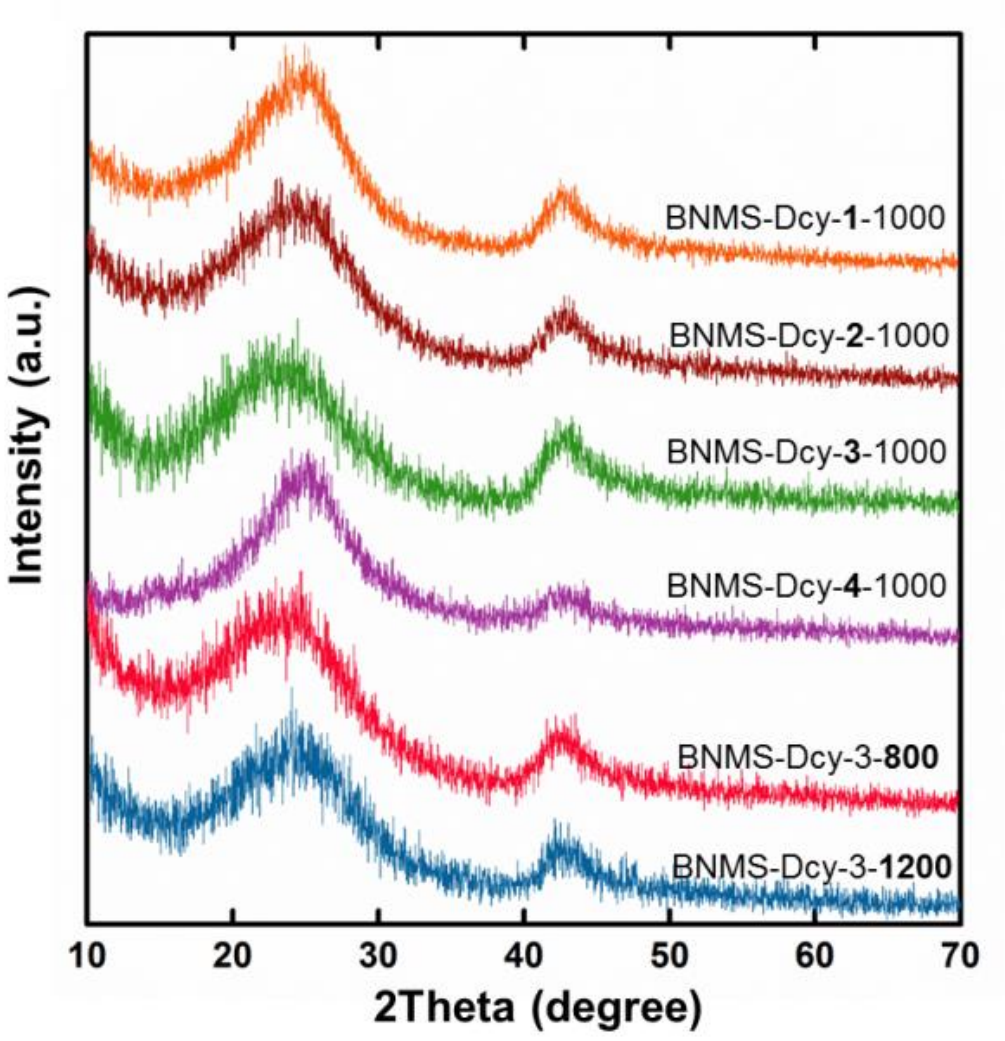

Figure 6.6 XRD patterns of BNMS samples. Reproduced from Ref. 21, Chapter 3.

6.8 Table 6.2. List of Raman E_{2g} shifts of BNMS samples studied

Samples	1	2	3	Average shifts (cm^{-1})	Standard deviation
BNMS-Dcy-1-1000	1373.20	1373.29	1373.42	1373.30	0.110604
BNMS-Dcy-2-1000	1374.01	1374.43	1373.75	1374.06	0.343123
BNMS-Dcy-3-1000	1374.83	1374.45	1374.95	1374.74	0.261024
BNMS-Dcy-4-1000	1373.61	1373.59	1373.25	1373.48	0.202320
BNMS-Dcy-3-800	1376.47	1376.39	1376.64	1376.50	0.127671
BNMS-Dcy-3-1200	1372.34	1372.31	1372.01	1372.22	0.182483

Reproduced from Ref. 21, Chapter 3.

6.9 FT-IR spectra of BCNO porous microbelt samples

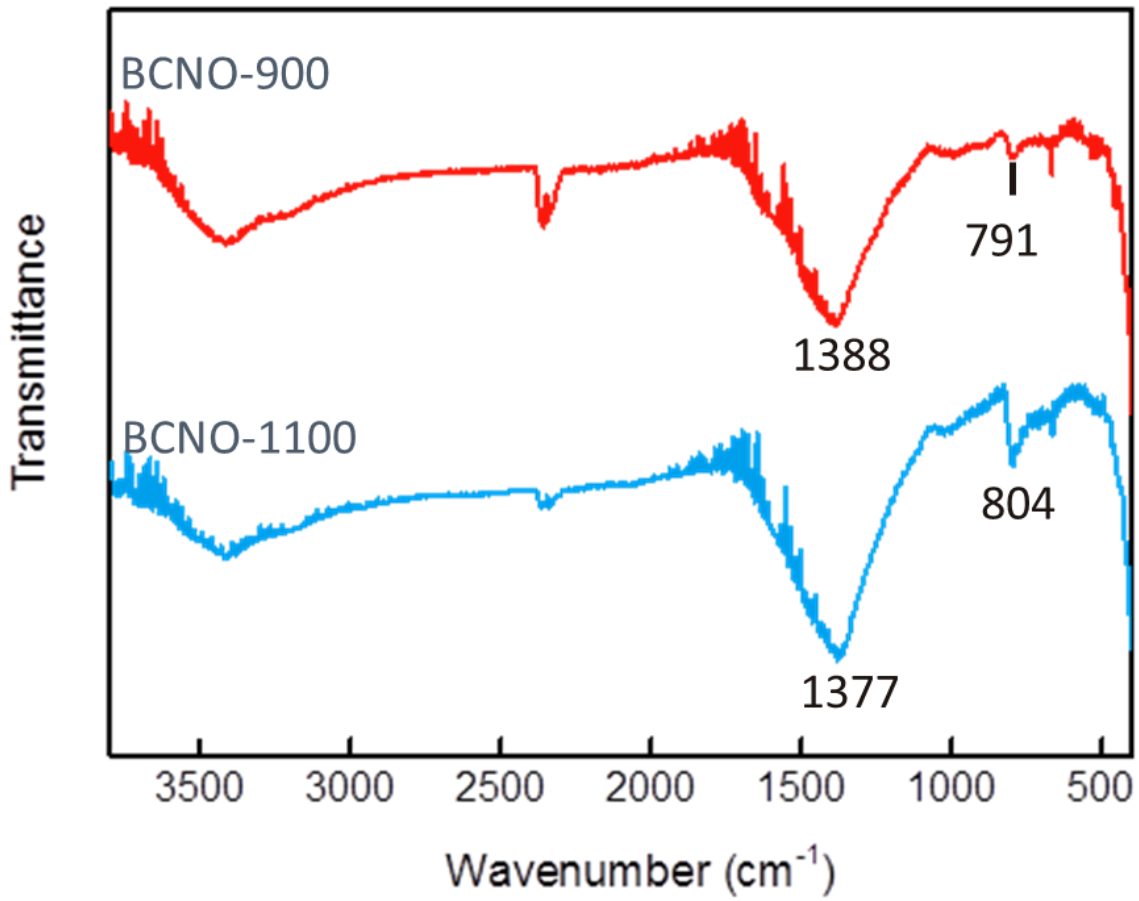

Figure 6.7 FT-IR spectra of BCNO-900 and BCNO-1300.

6.10 UV/Vis spectra of BCNO porous microbelt samples

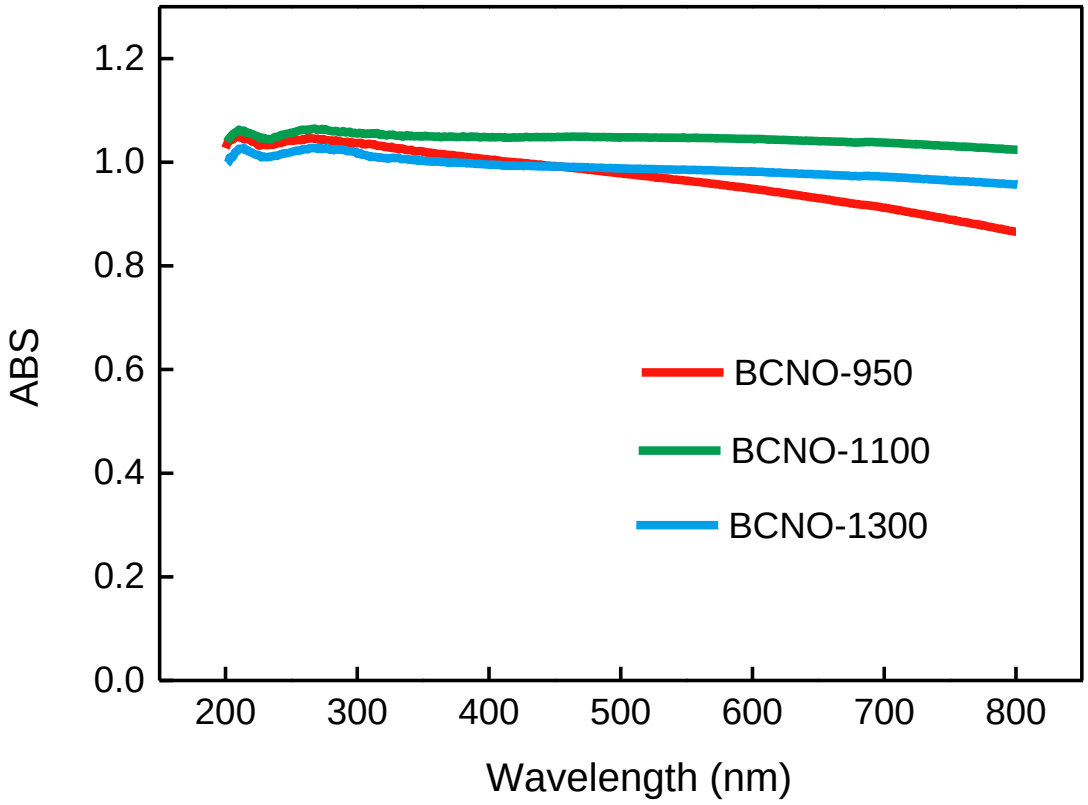

Figure 6.8 UV/Vis spectra of BCNO-900, BCNO-1100, and BCNO-1300.

List of Publications

From April 2012 to December 2014

Academic publications

1. **Weng, Q. H.**; Wang, X. B.; Zhi, C. Y.; Bando, Y.; Golberg. D. *Boron Nitride Porous Microbelts for Hydrogen Storage*. ***ACS Nano*** 2013, *7(2)*, 1558–1565.
2. **Weng, Q. H.**, Wang, X., Bando, Y., Golberg, D. *One-Step Template-Free Synthesis of Highly Porous Boron Nitride Microsponges for Hydrogen Storage*. ***Adv. Energy Mater.*** 2014, *4(7)*, 1301525.
3. **Weng, Q. H.**; Wang, X. B.; Wang, X.; Liu, D. Q.; Jiang, X. F.; Zhi, C. Y.; Bando, Y.; Golberg, D. *Preparation and Hydrogen Sorption Performances of BCNO Porous Microbelts with Ultra-Narrow and Tunable Pore Widths*. ***Chem. Asian J.*** 2013, *8(12)*, 2936–2939. (*Journal issue cover paper*)
4. **Weng, Q. H.**; Wang, B. J.; Wang, X. B.; Hanagata, N.; Li, X.; Liu, D. Q.; Wang, X.; Jiang, X. F., Zhi, C. Y., Bando, Y.; Golberg, D. *Highly Water-Soluble, Porous, and Biocompatible Boron Nitrides for Anticancer Drug Delivery*. ***ACS Nano***2014, *8(6)*, 6123–6130.
5. **Weng Q.H.**, Wang X., Wang X. B, Zhang C., Jiang X., Bando Y., Golberg D. *Supercapacitive energy storage performance of molybdenum disulfide nanosheets wrapped with micoporous carbons*. ***J. Mater. Chem. A***. (2014); doi 10.1039/C4TA06303A.
6. Wang, X.; **Weng, Q. H.**; Liu, X.; Wang, X. B.; Tang, D.; Tian, W.; Zhang, C.; Yi, W.; Liu, D.; Bando, Y.; Golberg, D. *Atomistic Origins of High Rate Capability and Capacity of N-Doped Graphene for Lithium Storage*. ***Nano Lett.*** 2014, *14(3)*, 1164–1171.
7. Liu, D.; Wang, X.; He, D.; Dao, T. D.; Nagao, T.; **Weng, Q. H.**; Tang, D.; Wang, X.; Tian, W.; Golberg, D.; Bando, Y. *Magnetically Assembled Ni@Ag Urchin-Like Ensembles with Ultra-Sharp Tips and Numerous Gaps for SERS Applications*. ***Small*** 2014, 10, 2564–2569.
8. Wang, X. B.; Zhang, Y.; Zhi, C. Y.; Wang, X.; Tang, D. M.; Xu, Y. B.; **Weng, Q. H.**; Jiang, X. F.; Mitome, M.; Golberg, D.; Bando, Y. *Three-Dimensional Strutted Graphene Grown by Substrate-Free Sugar Blowing for High-Power-Density Supercapacitors*. ***Nat. Commun.*** 2013, 4, 2905.
9. Wang, X. B.; Zhi, C.Y.; **Weng, Q. H.**; Bando, Y.; Golberg, D. *Boron Nitride Nanosheets: Novel Syntheses and Applications in Polymeric Composites*. ***J. Phys.: Conf. Ser.*** 2013, 471, 012003.
10. Wang, X. B.; Pakdel, A.; Zhang, J.; **Weng, Q. H.**; Zhai, T. Y.; Zhi, C.Y.; Golberg, D.; Bando, D. *Large-*

Surface-Area BN Nanosheets and Their Utilization in Polymeric Composites with Improved Thermal and Dielectric Properties. ***Nanoscale Res. Lett.*** 2012, *7*, 662.

Presentations

1. **Weng, Q. H.**; Wang, X. B.; Bando, Y.; Golberg, D. *Porous Boron Nitride Materials: Template-Free Fabrication and H_2 Adsorption Properties*, ***MANA International Symposium 2014***, Tsukuba, Japan, Mar, 5~7, 2014. (Poster)
2. **Weng, Q. H.**; Wang, X. B.; Wang, X.; Liu, D. Q.; Jiang, X. F.; Zhi, C. Y.; Bando, Y.; Golberg, D. *Hydrogen Sorption Performances of BCNO Porous Microbelts with Ultra-Narrow and Tunable Pore Width,* ***12th International Conference on Atomically Controlled Surfaces, Interfaces and Nanostructures in conjunction with 21st International Colloquium on Scanning Probe Microscopy***, Tsukuba, Japan, Nov, 4~8, 2013. (Oral)
3. **Weng, Q. H.**; Wang, X. B.; Bando, Y.; Golberg, D. *Facile Template-Free Preparation of Highly Porous Boron Nitrides for Hydrogen Storages*, ***2013 MRS Fall Meetings***, Boston, US, Dec, 1~6, 2013. (Poster)

Previous work (at Xiamen University)

1. **Weng, Q. H.**; He, Q.; Sun, D.; Huang, H. Y.; Xie, S. Y.; Lu, X.; Huang, R. B.; Zheng, L. S. *Separation and Characterization of $C_{70}(C_{14}H_{10})$ and $C_{70}(C_5H_6)$ from an Acetylene–Benzene–Oxygen Flame*. ***J. Phys. Chem. C*** 2011, *115(22)*, 11016–11022.
2. **Weng, Q. H.**; He, Q.; Liu, T.; Huang, H. Y.; Chen, J. H.; Gao, Z. Y.; Xie, S. Y.; Lu, X.; Huang, R. B.; Zheng, L. S. *Simple Combustion Production and Characterization of Octahydro[60]fullerene with a Non-IPR C60 Cage*. ***J. Am. Chem. Soc.*** 2010***,*** *132(43)*, 15093–15095.
3. **Weng, Q. H.**; Sun, D.; Lin, S. C.; Chen, J. H.; Xie, S. Y.; Huang, R. B.; Zheng, L. S. *patent CN101503188*, Mar, 2009.
4. Chen, J. H.; Gao, Z. Y.; **Weng, Q. H.**; Jiang, W. S.; He, Q.; Liang, H.; Deng, L. L.; Xie, S. L.; Huang, H. Y.; Lu, X.; Xie, S. Y.; Shi, K.; Huang, R. B.; Zheng, L. S. *Combustion Synthesis and Electrochemical Properties of the Small Hydrofullerene $C_{50}H_{10}$*. ***Chem. Eur. J.*** 2012, *18(11)*, 3408–3415.